

December 2014

# A Novel Transport Based Model for Wire Media and Its Application to Scattering Problems

Ebrahim Forati

*University of Wisconsin-Milwaukee*

Follow this and additional works at: <https://dc.uwm.edu/etd>



Part of the [Electromagnetics and Photonics Commons](#)

---

## Recommended Citation

Forati, Ebrahim, "A Novel Transport Based Model for Wire Media and Its Application to Scattering Problems" (2014). *Theses and Dissertations*. 458.

<https://dc.uwm.edu/etd/458>

This Dissertation is brought to you for free and open access by UWM Digital Commons. It has been accepted for inclusion in Theses and Dissertations by an authorized administrator of UWM Digital Commons. For more information, please contact [open-access@uwm.edu](mailto:open-access@uwm.edu).

A NOVEL TRANSPORT BASED MODEL FOR WIRE MEDIA  
AND ITS APPLICATION TO SCATTERING PROBLEMS

by

Ebrahim Forati

A Dissertation Submitted in  
Partial Fulfillment of the  
Requirements for the Degree of

DOCTOR OF PHILOSOPHY

in

ENGINEERING

at

The University of Wisconsin–Milwaukee

May 2014

## ABSTRACT

### A NOVEL TRANSPORT BASED MODEL FOR WIRE MEDIA AND ITS APPLICATION TO SCATTERING PROBLEMS

by

Ebrahim Forati

The University of Wisconsin–Milwaukee, 2014  
Under the Supervision of Professor George W. Hanson

Artificially engineered materials, known as metamaterials, have attracted the interest of researchers because of the potential for novel applications. Effective modeling of metamaterials is a crucial step for analyzing and synthesizing devices. In this thesis, we focus on wire medium (both isotropic and uniaxial) and validate a novel transport based model for them.

Scattering problems involving wire media are computationally intensive due to the spatially dispersive nature of homogenized wire media. However, it will be shown that using the new model to solve scattering problems can simplify the calculations a great deal. For scattering problems, an integro-differential equation based on a transport formulation is proposed instead of the convolution-form integral equation that directly comes from spatial dispersion. The integro-differential equation is much faster to solve than the convolution equation form, and its effectiveness is confirmed by solving several examples in one-, two-, and three-dimensions. Both the integro-differential equation formulation and the homogenized wire medium parameters are experimentally confirmed. To do so, several isotropic connected wire medium spheres have been fabricated using a rapid-prototyping machine, and their measured extinction cross sections are compared with simulation results. Wire parameters (period and diameter) are varied to the point where homogenization theory breaks down, which is observed in the measurements. The same process is done for three-dimensional cubical objects made of a uniaxial wire medium, and their

measured results are compared with the numerical results based on the new model. The new method is extremely fast compared to brute-force numerical methods such as FDTD, and provides more physical insight (within the limits of homogenization), including the idea of a Debye length for wire media. The limits of homogenization are examined by comparing homogenization results and measurement.

Then, a novel antenna structure is proposed utilizing an Epsilon Near Zero (ENZ) material and the total internal reflection principle. The epsilon near zero material of the antenna is realized by use of a wire medium which acts as an artificial plasma and exhibits ENZ condition at a frequency called the plasma frequency. This will lead us the question of whether or not the ENZ condition is realizable using spatially dispersive materials (e.g. wire medium). To answer this question, the momentum-dependent permittivity for a broad class of natural materials and wire-mesh metamaterials with spatial dispersion is determined in real-space, and a new characteristic length parameter is defined, in addition to the Debye length, which governs polarization screening. It is found that in the presence of spatial dispersion the electric displacement does not vanish at the plasma frequency, in general. However, conditions are investigated under which the permittivity can vanish or be strongly diminished, even in the presence of spatial dispersion, implementing an epsilon-near-zero material. The thesis will end with a chapter about homogenization of graphene. Although it does not completely follow the subject of the thesis, the last chapter shows another example of homogenization applications. In this last chapter, using periodicity and homogenization, a hyperlens is realized for surface plasmons on graphene. In general, such hyperlens cannot be realized without using periodic structures (metamaterials).



© Copyright by Ebrahim Forati, 2014  
All Rights Reserved

To my parents, for their endless love

# TABLE OF CONTENTS

<b>1</b>	<b>Introduction</b>	<b>1</b>
1.1	Background and motivation . . . . .	1
1.2	Thesis organization . . . . .	11
<b>2</b>	<b>The drift diffusion model and its applications in scattering problems [1]</b>	<b>14</b>
2.1	The direct integral equation method for scattering problems . . . . .	14
2.2	Integro-differential equation - the drift-diffusion approach . . . . .	19
<b>3</b>	<b>Examples of scattering problems using the DD approach [2; 3]</b>	<b>23</b>
3.1	One dimensional isotropic example . . . . .	24
3.2	Two dimensional isotropic example . . . . .	27
3.3	Three dimensional isotropic example . . . . .	30
3.3.1	Formulation . . . . .	30
3.3.2	Simulation and measurement results . . . . .	36
3.3.3	Effect of wire period: breakdown of homogenization . . . . .	40
3.3.4	Fabrication process . . . . .	43
3.4	Three dimensional anisotropic example . . . . .	43
3.5	Debye length and homogenization parameters . . . . .	50
3.6	Appendix: More details on the formulations in 3.3 . . . . .	55
<b>4</b>	<b>A novel antenna structure using epsilon near zero material and total internal reflection principle [4]</b>	<b>62</b>
4.1	Introduction . . . . .	62
4.2	The antenna geometry and results . . . . .	63
4.3	Summary . . . . .	67
<b>5</b>	<b>On the possibility of ENZ realization using spatially dispersive material [5]</b>	<b>69</b>
5.1	introduction . . . . .	69
5.2	Permittivity tensor and polarization vector in space domain . . . . .	73
5.2.1	Permittivity tensor . . . . .	73
5.2.2	Polarization as a function of the total field . . . . .	74
5.2.3	Polarization as a function of the scattered field . . . . .	75
5.2.4	Polarization as a function of the incident field . . . . .	76
5.3	Discussion of the results and the establishment of the ENZ condition . . .	78
<b>6</b>	<b>Homogenization example: hyperlensing by a graphene monolayer [6]</b>	<b>85</b>
6.1	introduction . . . . .	85
6.2	Theory and formulation . . . . .	87
6.3	Realization of the hyperlens . . . . .	89
6.4	Summary . . . . .	94
6.5	Appendix . . . . .	94

6.5.1	On the modeling of graphene layer by a thin dielectric . . . . .	94
6.5.2	Proof of (6.13) . . . . .	97
6.5.3	Proof of (6.2) . . . . .	98
6.5.4	Proof of (6.5) and (6.6) . . . . .	99
6.5.5	Idealized graphene nanoribbons with hard-boundaries . . . . .	101
6.5.6	Simulation setup for the hard- and the soft-boundary examples . .	102
6.5.7	The improvement of canalization by increasing the frequency . .	104
6.5.8	Modulated graphene conductivity using a rectangular ridged ground plane . . . . .	105
<b>7</b>	<b>Summary, future work and outlook</b>	<b>108</b>
	<b>Bibliography</b>	<b>111</b>

# LIST OF FIGURES

1.1	Spheroid geometry. . . . .	6
1.2	The difference between homogenization (left) and photonic (right) techniques. . . . .	8
1.3	Depiction of an isotropic connected wire medium having period $a$ and wire diameter $d$ . . . . .	9
1.4	Depiction of a uniaxial wire medium. . . . .	11
2.1	Volume equivalence principle for nonlocal materials. Left side: the original problem of a nonlocal medium having volume $\Omega$ immersed in a local background medium. Right: the equivalent problem of a homogeneous local medium having, within the volume $\Omega$ , nonzero polarization and conduction currents. . . . .	15
3.1	Wire medium slab with host relative permittivity of $\epsilon_r$ in air. . . . .	24
3.2	Real part of the charge distribution inside a nonlocal semiconductor slab for three different dopant densities using the drift diffusion formulation and the coupled transport-Poisson formulation [7]. . . . .	26
3.3	Wire medium slab infinite in the x and y directions. . . . .	27
3.4	Comparison of the transmission coefficient of a wire medium slab using the integro-differential drift diffusion method and the wave expansion method of [8]. . . . .	28
3.5	Internal field $E_y$ of a wire medium slab using the integro-differential drift diffusion method and the wave expansion method of [8]. . . . .	30
3.6	Internal field $E_z$ of a wire medium slab using the integro-differential drift diffusion method and the wave expansion method of [8]. . . . .	31
3.7	Wire medium spheres fabricated using a rapid prototyping machine. All spheres have 50 mm diameter except the far-right sphere, which has diameter 25 mm. . . . .	37
3.8	A close-up of the 50 mm and 25 mm wire medium spheres, both having period 4 mm. . . . .	37
3.9	A close-up of the D40a12d2 and D40a12d2C spheres. Both have the same diameter, period, and wire thickness, but the latter sphere (C) has wires crossing at the center, whereas the other sphere does not. . . . .	38
3.10	Measurement set-up. A: x-band horn antennas, B: strings for alignment, C: microwave absorbers, D: E8361A Network analyzer, E: height adjustment, F: WM sphere on a Styrofoam pedestal. . . . .	38
3.11	Normalized measured and theoretical extinction cross sections of the D50a4d1 wire medium sphere and of a plastic sphere. . . . .	39
3.12	Normalized measured and theoretical extinction cross sections of the D25a4d1 sphere. . . . .	41

3.13	Normalized measured and theoretical extinction cross sections of the D50a8d2, D50a12d2, and D50a12d2C spheres. Because of the large wire periods, homogenization theory becomes inapplicable in most of the measurement range. . . . .	42
3.14	Normalized measured extinction cross section of the D50a4d2, D50a8d2, D50a12d2, and D50a12d2C spheres showing the angle dependance for the spheres having larger periods. . . . .	43
3.15	Sphercal objects in the middle of the rapid prototyping process. . . . .	44
3.16	Sphercal objects after fabrication by rapid prototyping and before coating by paint. . . . .	45
3.17	The used silver paint and thinner for coating the objects. . . . .	46
3.18	A cubical object made of a uniaxial wire medium. . . . .	47
3.19	Measurement set-up. A: x-band horn antennas, B: microwave absorbers, C: height adjustment, D: E8361A Network analyzer, E: a fabricated 3 by 3 wire object on a Styrofoam pedestal. Wire diameter, period, and length are 2, 4, and 12 millimeters, respectively. . . . .	49
3.20	Normalized scattering cross section of a 3 by 3 wire cubical object with a 1 mm substrate. The incident electric field and wires are parallel. . . . .	49
3.21	Normalized scattering cross section of a 5 by 5 wire cubical object. . . . .	50
3.22	Normalized scattering cross section of cubical objects with different number of wires. Wires have $p = 4$ mm and $d = 1$ mm. . . . .	52
3.23	Normalized scattering cross section of 5 by 5 wire rectangular objects with $d = 1$ and $p = 4$ mm. For (a) wire length is well longer than the Debye length, whereas for (b) that is not the case, leading to a larger frequency shift between full wave and homogenized results. . . . .	53
3.24	Normalized scattering cross section of 5 by 5 wire rectangular objects with $d = 1$ and $b = 20$ mm. The breakdown of homogenization with increasing period is evident. . . . .	53
3.25	Normalized scattering cross section of 5 by 5 wire cubical objects with $p = 4$ mm. . . . .	54
4.1	TM wave incident on a (a) dielectric and ( b) PEC material at a $45^\circ$ angle. . . . .	64
4.2	Half of the proposed geometry. Full geometry will be obtained by adding a mirror image in the x-z plane. . . . .	65
4.3	Full wave simulated electric field distribution on the radiating edge. . . . .	65
4.4	Full wave simulated directivity and field distribution of the difference pattern. . . . .	66
4.5	Full wave simulated directivity and field distribution of the sum pattern. . . . .	66
4.6	The antenna geometry using uniaxial wire medium as its ENZ material. . . . .	67
4.7	The difference pattern (directivity) of the antenna with uniaxial wire medium. . . . .	67
4.8	The sum pattern (directivity) of the antenna with uniaxial wire medium. . . . .	68
5.1	Isotropic connected wire medium with wire period (a) and radius ( $r_w$ ). . . . .	70

5.2	Waveguide with a section of ENZ material: a. depicts an idealized ENZ material in the center region of the waveguide, otherwise filled with a simple constant-permittivity medium, and b. shows the section filled with an isotropic wire medium. c. TE <sub>20</sub> mode in the idealized ENZ, d. TE <sub>20</sub> mode in the actual wire medium, e. TM <sub>11</sub> mode in the idealized ENZ, and f. TM <sub>11</sub> mode in the actual wire medium. . . . .	82
5.3	Normalized screening length of the ICWM ( $L_\alpha/\lambda_0$ ) as a function of the wire period ( $a$ ) and radius ( $r_w$ ) at $\omega = 1.2\omega_p$ . . . . .	84
6.1	An infinite graphene layer in the $yz$ -plane. The conductivity of graphene is isotropic ( $\sigma_0$ ) everywhere except in the red region, where it is anisotropic ( $\bar{\sigma}$ ). The anisotropic region will be created by a suitable gate bias. . . . .	87
6.2	Triangular ridged ground plane for achieving conductivity modulation (leading to a soft-boundary profile). . . . .	90
6.3	The conductivity distributions resulting from the bias modulation scheme depicted in Fig. 6.2. Also shown is the idealized hard-boundary case discussed in the appendix. . . . .	91
6.4	The normalized $x$ -component of the electric field at the source (left) and image (right) planes of the modulated graphene surface. Source and image lines are at separated by $2\lambda_{\text{SPP}}$ (the region $-1 < x < 1$ is the dielectric slab model of graphene). . . . .	91
6.5	The normalized $x$ -components of the electric field at the source and image lines on the surface of the modulated graphene ( $x = 1$ nm). . . . .	92
6.6	Normalized $x$ -component of the electric field above the modulated graphene surface (left) and a homogenous graphene surface (right). . . . .	92
6.7	The effect of loss on the image canalization for hard- and soft-boundary bias modulations. . . . .	93
6.8	The error (6.14) as a function of the normalized dielectric thickness and conductivity of graphene. The graph is frequency independent. . . . .	97
6.9	An infinite graphene layer with isotropic periodic conductivity of $\sigma(z)$ . . . . .	100
6.10	The normalized $x$ -component of the electric field at the source (left) and image (right) planes of the hard-boundary example. Source and image lines are separated by $2\lambda_{\text{SPP}}$ (the region $-1 < x < 1$ is the dielectric slab model of graphene). . . . .	102
6.11	Normalized $x$ -component of the electric field above the graphene surface. . . . .	102
6.12	The normalized $x$ -components of the electric field at the source and image lines on the surface of the graphene (taken at the height $x = 1$ nm) for the hard-boundary example. . . . .	103
6.13	The dielectric model of the hard-boundary graphene strip example. . . . .	103
6.14	The dielectric model for the soft-boundary example - constant permittivities and smoothly-varying thickness model graphene's sinusoidal chemical potential. . . . .	104
6.15	The ratio $\text{Im}(\sigma)/\text{Re}(\sigma)$ as a function of chemical potential for three different frequencies. . . . .	105

6.16	The normalized $x$ -component of the electric field above the graphene surface ( $x = 2$ nm) for the peak value of $\text{Im}(\sigma)/\text{Re}(\sigma)$ at 10 THz (top-left), 20 THz (top-right), and 30 THz (bottom). . . . .	106
6.17	An alternative geometry with rectangular ridged ground plane to realize the soft-boundary example. . . . .	106
6.18	The conductivity distribution in the geometry of Fig. 6.17. . . . .	107



## LIST OF TABLES

5.1	Normalized characteristic screening and Debye length of some sample materials . . . . .	81
-----	---	----

# LIST OF SYMBOLS

$\epsilon_0$	vaccum permittivity
$\mu_0$	vaccum permeability
<b>J</b>	volume current density
<b>H</b>	magnetic field intensity
<b>E</b>	electric field intensity
<b>D</b>	electric flux density
<b>B</b>	magnetic flux density
$\rho^{free}$	volume free charge density
$\sigma$	conductivity
$c$	speed of light
ENZ	epsilon near zero
SPP	surface plasmon polariton
THz	terahertz

## ACKNOWLEDGEMENTS

I would like to thank my adviser, Professor George W. Hanson, both for advising me throughout this project and for the valuable life lessons he imparted with his attitude and knowledge. Without his guidance and persistent help this dissertation would not have been possible for me. I can truly claim the past three years as the most progressive years of my life so far.

Besides thanking my committee members for reviewing and improving this thesis, I would like to thank Professor Robert Wood for his lectures, which thoroughly engaged me in quantum mechanics, and for his inspirational teaching style as well. To Professor Arash Mafi, for involving me in his group's weekly seminars, and exposing me to the beautiful world of quantum optics, and for his generous advice and help whenever I requested. To Professor Tzu-Chu Lin, through whom I was exposed to mathematical concepts entirely new to me, such as functional analysis, and the delicacy involved in the solution of integral equations. I also would like to thank Professor Ramin Pashaie for his kind support during my first semester at UWM. I appreciate the experience of having worked in his lab, and his advice is still fresh in my mind.

In addition, thanks to my friends Vahid, Salman and Parisa, Afsaneh, and Emad for our strong friendship and the helpful discussions we had. I wish all of them a bright and progressive future. Finally, special thanks to Jennifer Ede, my girlfriend, for her support both emotionally and technically to improve the readability of these notes.

What you seek is seeking you.

*Rumi*

# Chapter 1

## Introduction

### 1.1 Background and motivation

One of the most important steps for solving most of physical problems (if not all) is to model the problem properly and efficiently. Having a model enables us to organize the problem, make connections between different parts of the problem and math, use other people's investigation results, etc. In fact, finding precise and efficient models was the aim of many researchers in the history of science. For example, in chemistry, great scientists like Rutherford, Thomson and Bohr presented the well known atomic models known by their names. Or, in electronics, a lot of effort have been done to model transistors and the hybrid model is an instance of them. Fortunately, in electromagnetics, Maxwell's equations along with a few other equations (usually three or four equations) form a self sufficient model for most of the problems (if not all). It is worth noting that these Maxwell's equations are obtained experimentally and are considered as laws: Faraday's law, Ampere's law, and Gauss's law (in electricity and magnetism) and, usually, law's are observed phenomena in nature and their exact reasons are not necessarily known to us. In fact, theorems and hypothesizes are proven starting from laws (which are accepted to be true usually without knowing their reasons). Other examples of laws are Coulomb's and gravity laws (although the gravity law was generalized, or somehow dissproved, by a general reativity paper of Einstein). Minkowski's form of Maxwell's equations are,

$$\nabla \cdot \mathbf{D} = \rho^{free} \quad (1.1)$$

$$\nabla \cdot \mathbf{B} = 0 \quad (1.2)$$

$$\nabla \times \mathbf{H} = \mathbf{J} + j\omega\mathbf{D} \quad (1.3)$$

$$\nabla \times \mathbf{E} = -j\omega\mathbf{B} \quad (1.4)$$

where  $\mathbf{E}$  and  $\mathbf{H}$  are electric and magnetic field intensities, and  $\mathbf{D}$  and  $\mathbf{B}$  are electric and magnetic displacement fields, respectively and  $\mathbf{J}$  is the volume current density. Among the above four equations, only two of them are linearly independent equations. Maxwell's equations, as mentioned before, need a few more equations to form a self sufficient model for electromagnetic analysis. Usually, two constitutive relations are given to relate  $\mathbf{E}$ ,  $\mathbf{H}$ ,  $\mathbf{D}$ , and  $\mathbf{B}$  inside a material. The simplest form of constitutive relations are for vacuum as

$$\mathbf{D} = \varepsilon_0\mathbf{E} \quad (1.5)$$

$$\mathbf{B} = \mu_0\mathbf{H} \quad (1.6)$$

where  $\varepsilon_0$  and  $\mu_0$  are physical constants called permittivity and permeability, respectively. The value of  $\mu_0$  is defined by the international standard organization as  $4\pi \times 10^{-7}$ . Then,  $\varepsilon_0$  is defined by the formula  $\varepsilon_0 = \frac{1}{\mu_0 c^2}$  where  $c$  is the speed of light in vacuum which is a fixed number in the international system of units (299,792,458). This number is also used in defining meter as the unit of length. Originally, permittivity was used to relate mechanical and electrical quantities as in Coulomb's law. The other two equations which are usually added to the above system is the continuity equation as

$$\nabla \cdot \mathbf{J} = -j\omega\rho \quad (1.7)$$

and Ohm's law as

$$\mathbf{J} = \sigma\mathbf{E} \quad (1.8)$$

where  $\rho$  is the volume charge density and  $\sigma$  is the conductivity. Ohm's law relies on the assumption that there is a linear relation between the electric field intensity and the current

density and its unit can be obtained from the resistance unit (which is defined by the international system of units as ohm). Materials which show this property (i.e. satisfy (1.8)) are known as ohmic materials. The most famous ohmic materials are metals like copper and silver and the most famous non ohmic materials are semiconductors like silicon and germanium. Equations (1.1)-(1.8) form a self sufficient set of equations as it has six unknown quantities and there are six independent equations. Unknown are  $\mathbf{E}$ ,  $\mathbf{H}$ ,  $\mathbf{D}$ ,  $\mathbf{B}$ ,  $\mathbf{J}$ , and  $\rho$ . The equations are two independent Maxwell's equations, two constitutive equations, continuity equation and Ohm's law. Among the above six equations, Maxwell's equation and the continuity equation are obtained from physical laws (note that the continuity equation is a form of conservation law) which are always true independent of the material. Then, the challenge in modeling an electromagnetic problem is to define (or to discover) three remaining material- or response-related equations. In the above example, the three remaining equations are provided by defining two constitutive relations and an Ohm's equation. However, the constitutive relations can become complicated depending on the material. As an example, for a class of materials called BiIsotropic (BI), the constitutive relations are

$$\mathbf{D} = \varepsilon_0 \varepsilon_r \mathbf{E} + \xi \mathbf{H} \quad (1.9)$$

$$\mathbf{B}_{av} = \zeta \mathbf{E} + \mu_0 \mu_r \mathbf{H} \quad (1.10)$$

where  $\xi$  and  $\zeta$  are constants. Some subclasses of biisotropic materials are chiral materials for which the constitutive relations are

$$\mathbf{D} = \varepsilon_0 \varepsilon_r \mathbf{E} + \frac{(\chi + j\kappa)}{c} \mathbf{H} \quad (1.11)$$

$$\mathbf{B} = \frac{(\chi - j\kappa)}{c} \mathbf{E} + \mu_0 \mu_r \mathbf{H}. \quad (1.12)$$

We have several special cases:

- General BI medium: non-reciprocal ( $\chi \neq 0$ ), chiral ( $\kappa \neq 0$ );

- Tellegen medium: non-reciprocal ( $\chi \neq 0$ ), non-chiral ( $\kappa = 0$ );
- Pasteur medium: reciprocal ( $\chi = 0$ ), chiral ( $\kappa \neq 0$ ).

In general, the constitutive relations can be even more complicated than the examples mentioned so far and they can include integro-differential terms. The parameters in the constitutive relations can be spatially and/or temporally dispersive, which means that they can be frequency and/or position dependent. They can also be direction dependent in which case the parameters are usually expressed as tensors.

The process of finding the constitutive relations is a separate and well developed subject of research which usually starts from the microscopic structure of the materials consisting of atoms and their electrons. The local quantities of the parameters of the electromagnetic model in the atomic scale are usually labeled as microscopic values and their spatial average over a big enough area are usually called the macroscopic values. It is much more convenient to ultimately eliminate the microscopic quantities from our analysis and work only with the macroscopic quantities which are measurable. This will lead to the defining of some parameters properly in a constitutional relation form for each material. This whole process is often called homogenization. After homogenization has been done and the constitutive relations are defined for a material, we will no longer deal with microscopic values. All we calculate as, say, electric field is a spatial average of the microscopic electric field inside the material which is what is useful for us. However, this process is useful only when the wavelength is much larger than the distances between atoms in the material.

The same argument is true when there is a mixture of different materials for which their dimensions are smaller than the wavelength. There are several theories by which the mixture can be modeled by a continuous homogenous material with a constitutive relation. For example, in the following we briefly review Maxwell-Garrett theory which homogenizes a mixture of particles with permittivity of  $\varepsilon_i$  in a host medium with permittivity of  $\varepsilon_h$ .



## Maxwell-Garnett theory review

Homogenized effective medium parameters are defined to simplify calculations involving a mixture of different materials. For low volume fractions of inclusions in a host medium all such mixing formulas are equivalent. Maxwell-Garnett (MG) theory expresses the effective permittivity of a composite medium in terms of the volume fraction of the inclusions. The effective relative permittivity of a composite medium consisting of randomly-oriented spheroidal inclusions having isotropic relative permittivity  $\varepsilon_p$  in a host medium having isotropic relative permittivity  $\varepsilon_h$  is [9]

$$\varepsilon_{eff} = \varepsilon_h \left( 1 + \frac{\frac{F_v}{3V\varepsilon_h\varepsilon_0} \sum_{j=a,b,c} \alpha_j}{1 - \frac{F_v}{3V\varepsilon_h\varepsilon_0} \sum_{j=a,b,c} N_j \alpha_j} \right) \quad (1.13)$$

where  $\varepsilon_0$  is the vacuum permittivity,  $\alpha_j$  is the polarizability ( $\text{Fm}^2$ ),  $N_j$  is the dimensionless depolarization factor, and  $F_v = \rho_0 V$  is the volume fraction of inclusions, where  $\rho_0$  is the density of inclusions ( $\text{m}^{-3}$ ),  $V = 4\pi abc/3$  is the inclusion volume,  $a = b$  are the semi minor (prolate) and semi major (oblate) axes, and  $c$  is the semi major (prolate) and semi minor (oblate) axis, as shown in Fig. 1.1. The polarizability and depolarization factors are given by

$$\alpha_j = V\varepsilon_h\varepsilon_0 \frac{\varepsilon_p - \varepsilon_h}{\varepsilon_h + N_j(\varepsilon_p - \varepsilon_h)}, \quad (1.14)$$

$$N_c = \frac{1 - e_p^2}{2e_p^3} \ln \left( \frac{1 + e_p}{1 - e_p} - 2e_p \right), \quad (1.15)$$

for a prolate spheroid ( $a = b < c$ ), and

$$N_c = \frac{1 + e_o^2}{e_o^3} (e_o - \tan^{-1}(e_o)) \quad (1.16)$$

for an oblate spheroid ( $a = b > c$ ), where  $e_p = \sqrt{1 - c^2/a^2}$ ,  $e_o = \sqrt{a^2/c^2 - 1}$ , and  $N_a = N_b = (1 - N_c)/2$ .

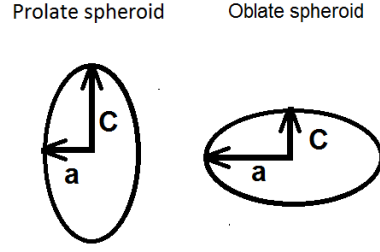


Figure 1.1: Spheroid geometry.

If we consider a vertical electric field, then in the extreme needle (prolate,  $N_c = N_{\parallel} = 0$ ,  $N_a = N_b = N_{\perp} = 1/2$ ) and disk (oblate,  $N_a = N_b = N_{\parallel} = 0$ ,  $N_c = N_{\perp} = 1$ ) limits the permittivity simplifies to

$$\varepsilon_{eff} = \varepsilon_h \left( 1 + \frac{\frac{F_v}{3V\varepsilon_h\varepsilon_0} (2\alpha_{\perp} + \alpha_{\parallel})}{1 - \frac{F_v}{3V\varepsilon_h\varepsilon_0} \alpha_{\perp}} \right), \quad (1.17)$$

where  $\alpha_{\perp}$  is the polarizability perpendicular to the long axis. Further, since  $\alpha_{\perp}$  is relatively small ( $\alpha_{\perp} \ll \alpha_{\parallel}$ ), the second term in the denominator can often be ignored and

$$\varepsilon_{eff} = \varepsilon_h + \frac{F_v \alpha_{\parallel}}{3V\varepsilon_0} = \varepsilon_h + \frac{\rho_0 \alpha_{\parallel}}{3\varepsilon_0}, \quad (1.18)$$

which is the usual Clausius-Mossotti dilute-limit form, where the factor of  $1/3$  is due to the equiprobability of particle orientations. For spherical particles  $\alpha_{\perp} = \alpha_{\parallel}$  and this factor is not present. Several comments on the validity of the Maxwell-Garnet effective permittivity are in order. First, we should consider low volume fractions, e.g.  $F_v = 10^{-6} - 10^{-3}$ , such that mutual interactions among inclusions are negligible, assuming stable colloids. In this range all effective medium formulations are equivalent, and the Maxwell-Garnet formulation is appropriate. Second, it should be noted the Maxwell-Garnet effective permittivity is independent of the actual size of the inclusions (for spheroids the dependence is on the axial ratio,  $c/a$ ), and, as such, is an unrestricted theory [10; 11] in the sense

that the resulting effective permittivity can be used in the same manner as any dielectric function. This is important since some of the homogenization theories are restricted in the sense that they are applicable for modeling the mixture only for specific calculations (e.g. only for reflection and transmission of wave calculations and not for wave absorption calculations). Extended effective medium formulations (typically formulated to account for higher multipole effects), which depend on the actual size of the inclusions, are restricted in their applicability, and generally cannot be used to compute absorption [10; 11]. Third, the Maxwell-Garrett permittivity assumes that the inclusions are stationary. Prolate spheroids can rotate in an applied electric field via their permanent and/or induced dipole moment [12], resulting in an anisotropic (and time-dependent) medium. At the end, it is worth noting that Maxwell-Garnett theory is derived from the well known Clausius-Masatti relation

$$\frac{\varepsilon - 1}{\varepsilon + 2} = \frac{4\pi}{3} \sum_j N_j \alpha_j \quad (1.19)$$

where  $\alpha_j$  is the polarizability of  $j$ 's particle and  $N_j$  is what called the depolarization factor and depends on the dimensions of the particle. In summary, by use of the Maxwell-Garnett homogenization for a nonmagnetic material, a constitutive relation will be obtained as

$$\mathbf{D} = \varepsilon_0 \varepsilon_{eff} \mathbf{E} \quad (1.20)$$

$$\mathbf{B} = \mu_0 \mathbf{H} \quad (1.21)$$

## Wire medium and its homogenized permittivity

The homogenization process which we reviewed (Maxwell-Garrett) was for a random positioned inclusions/atoms in a mixture. However, there are different homogenization processes which are developed specifically for periodic structures. These homogenization techniques were mainly developed to model materials with crystal structures. The general idea of these homogenization techniques is to use the Bloch theorem to decompose the

polarization response of the material into different Bloch waves. Then, in the limit that the wavelength is much larger than the lattice constant, the zeroth order Bloch wave is the dominant term and is used to obtain a constitutive relation as (1.20). If the wavelength is in the order of the lattice constant, a different approach will be used which is one of the subjects in photonics. This is depicted in Fig. 1.2.

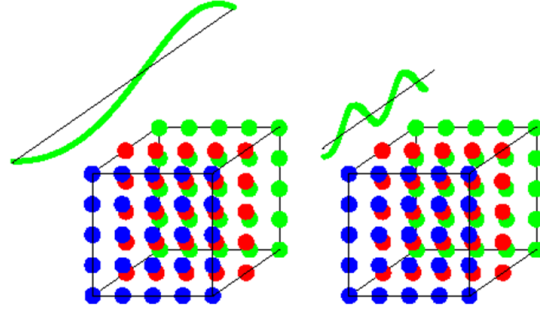


Figure 1.2: The difference between homogenization (left) and photonic (right) techniques.

The homogenization of a periodic structure was the main idea of artificially structured materials known as metamaterials (MTM). There are different definitions for the term metamaterial among which we chose the following two:

1- “Metamaterials are defined as macroscopic composites having a man-made, three dimensional, periodic cellular architecture designed to produce an optimized combination, not available in nature, of two or more responses to a specific excitation.” (by Rodger M. Walser)

2- “A metamaterial is an engineered composite that exhibits superior properties not observed in nature or in the constituent materials. The superior properties of a metamaterial are a result of their engineered constructs”. (DARPA’s US\$ 40 million metamaterials research program’s definition)

Both definitions share two conspicuous properties that MTMs should exhibit. First, the properties should be different than the constituent materials properties. Second, the properties should not be observed in nature.

The prefix “meta” comes from Greek and means “after” or “beyond”. There are

many different applications for these materials including super lensing and subwavelength imaging [13; 14; 15; 16; 17; 18], cloaking [19], shielding [20], and antenna applications [21; 22].

One of the most well-known metamaterials is the isotropic connected wire medium (ICWM) which is a square lattice of connected wires, as depicted in Fig. 1.3. ICWMs can act as an artificial plasma with negative permittivity and a relatively low (e.g., GHz) plasma frequency [8]. The basic concept of a wire medium as an artificial plasma has been known since the 1960s [23; 24]. However, recent studies have demonstrated interesting applications which were unknown before, as well as considerable complications arising from their spatially-dispersive nature [25; 26].

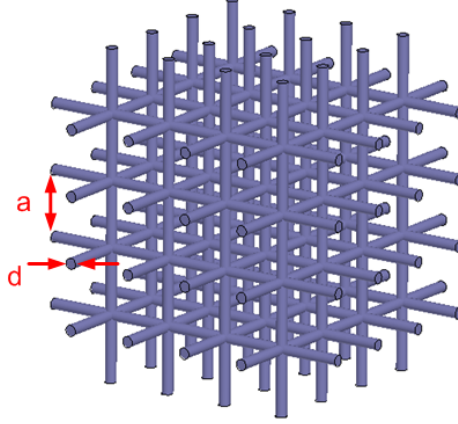


Figure 1.3: Depiction of an isotropic connected wire medium having period  $a$  and wire diameter  $d$ .

Consider an ICWM constructed from imperfectly-conducting wires characterized by  $\varepsilon_m = 1 - \omega_m^2 / (\omega(\omega - j\Gamma))$ , where  $\omega_m$  and  $\Gamma$  are the plasma frequency and damping frequency of the metal, respectively. When homogenization is appropriate (i.e., when the wire period is much smaller than wavelength [9]), both conduction and polarization effects can be contained in a single nonlocal relative permittivity [8],

$$\underline{\varepsilon}(\mathbf{q}, \omega) = \mathbf{1}\varepsilon_h - \kappa \left( \mathbf{1} - \frac{1}{q^2 + l_0 \left( \frac{\varepsilon_h k_p^2}{\varepsilon_m - \varepsilon_h} \frac{1}{f_v} - k_h^2 \right)} \mathbf{q}\mathbf{q} \right) \quad (1.22)$$

where

$$\kappa = \left( \frac{k_0^2}{k_p^2} - \frac{1}{\varepsilon_m - \varepsilon_h} \frac{1}{f_v} \right)^{-1}, \quad (1.23)$$

$f_v = \pi r^2/a^2$  is the volume fraction of the wires,  $r$  is the wire radius,  $a$  is the wire period,  $k_h = \omega\sqrt{\mu_0\varepsilon_0\varepsilon_h} = k_0\sqrt{\varepsilon_h}$  is the wavenumber in the dielectric supporting the wires,  $k_p = \omega_p/c$  is the plasma wavenumber given by  $(k_p a)^2 \cong 2\pi/\ln\left(\frac{a^2}{4r(a-r)}\right) \cong 2\pi/(\ln\left(\frac{a}{2\pi r}\right) + 0.5275)$ ; see [8],(11) for the exact expression, and  $l_0 = 3/(1 + 2k_p^2/\beta_1^2)$ , where

$$\frac{1}{\beta_1^2} = 2 \left( \frac{a}{2\pi} \right)^2 \sum_{n=1}^{\infty} \frac{[J_0\left(\frac{2\pi r}{a}n\right)]^2}{n^2}, \quad (1.24)$$

and where  $J_0$  is the zeroth-order Bessel function. As discussed in [8], this expression is very accurate below the effective plasma frequency, which, for  $\varepsilon_h \sim 1$  is

$$\frac{1}{\omega_{p,eff}^2} = \varepsilon_h \left( \frac{1}{\omega_m^2 f_v} + \frac{1}{k_p^2 c^2} \right). \quad (1.25)$$

If  $\varepsilon_h$  differs considerably from unity the effective transverse permittivity is not Drude-like and is given by a quadratic form obtained from setting the transverse permittivity to zero. The isotropic wire medium permittivity (1.22) reduces to the simpler form [27],

$$\underline{\varepsilon}(\mathbf{q}, \omega) = \mathbf{1}\varepsilon_h - \frac{k_p^2}{k_0^2} \left( \mathbf{1} - \frac{1}{q^2 - l_0 k_h^2} \mathbf{q}\mathbf{q} \right) \quad (1.26)$$

when  $|\varepsilon_m| \rightarrow \infty$ , i.e., as the wire conductivity becomes infinite.

A simpler form of wire medium is the uniaxial wire medium (UWM) as is shown in Fig. 1.4.

In [28], the homogenized nonlocal relative permittivity is obtained for a uniaxial wire medium with  $\varepsilon$ -negative rods as

$$\underline{\varepsilon}(\mathbf{q}) = \varepsilon_{xx} \hat{\mathbf{x}}\hat{\mathbf{x}} + \varepsilon_{xx} \hat{\mathbf{x}}\hat{\mathbf{x}} + \varepsilon_{xx}(\mathbf{q}) \hat{\mathbf{x}}\hat{\mathbf{x}}, \quad (1.27)$$

in which

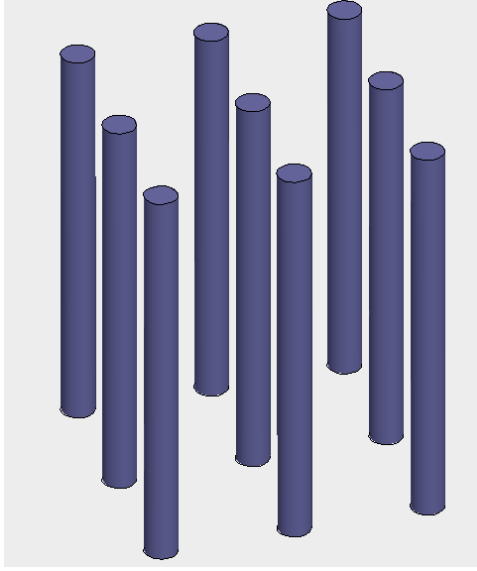


Figure 1.4: Depiction of a uniaxial wire medium.

$$\varepsilon_{xx} = \varepsilon_{yy} = 1 + \frac{2}{\frac{1}{f_V} \frac{(\varepsilon_m + \varepsilon_h)}{(\varepsilon_m - \varepsilon_h)} - 1}, \quad (1.28)$$

$$\varepsilon_{zz}(\mathbf{q}) = 1 + \frac{1}{\frac{1}{f_V} \frac{1}{(\varepsilon_m - \varepsilon_h)} - \frac{q^2 - q_z^2}{\beta_p^2}} \quad (1.29)$$

Note that in the above expressions permittivities are given in the spatial Fourier transform domain which is defined as

$$\mathcal{F}\{f(\mathbf{r})\} = F(\mathbf{q}) = \int f(\mathbf{r}) e^{-j\mathbf{q}\cdot\mathbf{r}} d^3\mathbf{r}, \quad (1.30)$$

$$f(\mathbf{r}) = \frac{1}{(2\pi)^3} \int F(\mathbf{q}) e^{j\mathbf{q}\cdot\mathbf{r}} d^3\mathbf{q}. \quad (1.31)$$

## 1.2 Thesis organization

This dissertation consists of seven chapters. Besides the introductory chapter which provided an overview of the electromagnetic model, homogenization in electromagnetics,

wire medium as an artificial plasma, and its homogenized permittivity (constitutive relation) there are six more chapters as follows.

In chapter two, the drift diffusion model will be introduced for spatially dispersive materials and specifically for wire medium. The equivalent (homogenized) parameters for the isotropic connected wire medium and uniaxial wire medium will also be given. Then, it will be shown how a scattering problem can be solved with much less computational effort using the drift diffusion model rather than the conventional model. To reveal this, the formulation for a scattering problem will be given using the conventional method (i.e. using the permittivity of (1.29)) and will be compared with the drift diffusion formulation for the same geometry. It will be seen that the conventional method leads to an integro-differential equation with six-fold integrals while the drift diffusion method will lead to an integro-differential equation with only three-fold integrals.

In chapter three, the drift diffusion model will be confirmed by measurement and the finite difference time domain (FDTD) numerical method. To do this, the drift diffusion model will be used to solve scattering problems involving 1-, 2-, and 3-D objects made of an isotropic connected wire medium. Numerical results obtained based on the drift diffusion method will be then compared with the measurement results and FDTD simulation results. Then, cubical objects made of uniaxial wire medium will be considered and their scattering cross sections will be calculated numerically based on the drift diffusion model and will be compared with measurement results and FDTD simulation results. In other words, both isotropic objects and anisotropic objects are studied to prove the drift diffusion model. Fabrication process for both isotropic and anisotropic objects will be discussed at the end of this chapter as well. After proving the drift diffusion model, the effect of the different parameters of the wire medium (wires thickness, period, and number in the object) on the accuracy of the homogenization method are studied. This is carried out by comparing the measurement results with the numerical results based on the drift diffusion method (which is obtained based on a homogenization technique).



In chapter four, an antenna is designed using the uniaxial wire medium as a material which exhibits permittivity of near zero at the operating frequency. This epsilon near zero condition has interesting applications which are mostly reported recently. In the beginning of chapter four, there will be an introduction to epsilon near zero materials and their applications. Besides using ENZ material, the proposed antenna benefits from the total internal reflection principle enabling it to create different radiation patterns. Especially, two of the radiation patterns called sum and difference patterns are very useful for radar applications. The antenna is fabricated and its measured radiation pattern is compared with the simulation results.

In chapter five, conditions will be studied under which the epsilon near zero is possible for spatially dispersive materials. It will be shown in this chapter that the permittivity of zero is not possible for a general excitation. Under some specific excitations the ENZ can be exactly achieved. For a general excitation, ENZ cannot be realized using the wire medium. This argument will be explained in detail in chapter five.

Chapter six can be considered as a separate metamaterial example which does not relate to wire medium. This chapter is included to emphasize the beauty of applications of periodic structures and metamaterials. A hyperlens is designed in this chapter using graphene monolayer with a periodic conductivity. The hyperlens, designed for surface plasmons, transfers perfect images overcoming the diffraction limit. In the end, chapter seven summarizes the thesis conclusions in a few pages.

## Chapter 2

### The drift diffusion model and its applications in scattering problems [1]

Before describing the transport-based integro-differential equation (drift diffusion model), in a section we describe what might be called the direct integral equation method for non-local materials, where we use the term “direct” since it results from the basic definition of nonlocal response.

#### 2.1 The direct integral equation method for scattering problems

We use the volume equivalence principle to replace a nonlocal medium (characterized by  $\sigma(\mathbf{r} - \mathbf{r}')$  and/or relative permittivity  $\epsilon(\mathbf{r} - \mathbf{r}')$  and having domain  $\Omega$ ) embedded in an infinite local medium characterized by  $\epsilon_1, \sigma_1$  with a homogeneous space characterized by  $\epsilon_1, \sigma_1$  but having equivalent volume conduction ( $\mathbf{J}_c$ ) and polarization ( $\mathbf{J}_p$ ) currents in the domain  $\Omega$ , as shown in Fig. 2.1. Note that although the volume equivalence principle is usually applied to local and linear materials, it is easy to show that it applies to very general nonlocal and even nonlinear materials [29]. Although we use the material parameters for a translationally invariant medium, the additional boundary condition described below rigorously accounts for the material boundary [30].

For example, assume the case of a material having a nonlocal conduction and polarization response,  $\mathbf{J}_c(\mathbf{q}) = (\sigma(\mathbf{q}) - \sigma_1) \mathbf{E}(\mathbf{q})$  and  $\mathbf{J}_p(\mathbf{q}) = j\omega\epsilon_0 (\epsilon(\mathbf{q}) - \epsilon_1) \mathbf{E}(\mathbf{q})$ , where we assume the spatial transform pair  $\mathbf{r} \leftrightarrow \mathbf{q}$ . The corresponding space-domain relations are

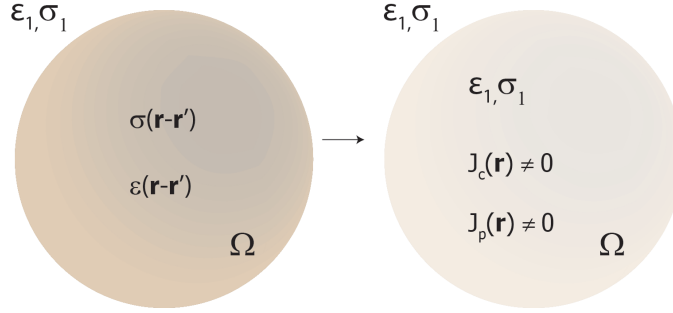


Figure 2.1: Volume equivalence principle for nonlocal materials. Left side: the original problem of a nonlocal medium having volume  $\Omega$  immersed in a local background medium. Right: the equivalent problem of a homogeneous local medium having, within the volume  $\Omega$ , nonzero polarization and conduction currents.

$$\mathbf{J}_c(\mathbf{r}) = \int (\sigma(\mathbf{r} - \mathbf{r}') - \sigma_1 \delta(\mathbf{r} - \mathbf{r}')) \mathbf{E}(\mathbf{r}') d\Omega', \quad (2.1)$$

$$\mathbf{J}_p(\mathbf{r}) = j\omega\epsilon_0 \int (\epsilon(\mathbf{r} - \mathbf{r}') - \epsilon_1 \delta(\mathbf{r} - \mathbf{r}')) \mathbf{E}(\mathbf{r}') d\Omega', \quad (2.2)$$

where (2.1) is a generalized ohm's law for the effective conduction response and (2.2) gives a similar relationship for the effective polarization response. The relationship between current and field is given in terms of a three-fold integral,

$$\mathbf{E}(\mathbf{r}) = -j\omega\mu \int \underline{\mathbf{G}}_{ee}(\mathbf{r}, \mathbf{r}') \cdot \mathbf{J}(\mathbf{r}') d\Omega', \quad (2.3)$$

where  $\underline{\mathbf{G}}_{ee}$  is the dyadic Green's function as

$$\underline{\mathbf{G}}_{ee}(\mathbf{r}, \mathbf{r}') = \left\{ \left( 3\hat{\mathbf{R}}\hat{\mathbf{R}} - \underline{\mathbf{I}} \right) \left( \frac{1}{k^2 R^2} - \frac{1}{jkR} \right) - \left( \hat{\mathbf{R}}\hat{\mathbf{R}} - \underline{\mathbf{I}} \right) \right\} \frac{e^{-jkR}}{4\pi R} - \underline{\mathbf{L}} \frac{\delta(\mathbf{r} - \mathbf{r}')}{k^2} \quad (2.4)$$

where  $\mathbf{R} = \mathbf{r} - \mathbf{r}'$ . In the volume integral in (2.3), if we find the principal value of the integral by excluding a disc with thickness  $2\delta$  around point  $\mathbf{r}$  inside the sphere of radius  $a_{\text{sphere}}$ , the integrals become  $\left( \int_0^{r-\delta} + \int_{r+\delta}^{a_{\text{sphere}}} \right) \int_0^\pi \int_0^{2\pi} \dots d\varphi d\theta dr$ , and the depolarizing dyadic will be [31]  $\underline{\mathbf{L}} = \hat{\mathbf{r}}\hat{\mathbf{r}}$ .

Then, the convolution-type integral equations to be solved are

$$\mathbf{J}_c(\mathbf{r}) = \int (\sigma(\mathbf{r} - \mathbf{r}') - \sigma_1 \delta(\mathbf{r} - \mathbf{r}')) \quad (2.5)$$

$$\times \left[ \left( -j\omega\mu \int \underline{\mathbf{G}}_{ee}(\mathbf{r}', \mathbf{r}'') \cdot \mathbf{J}_{eq}(\mathbf{r}'') d\Omega'' \right) + \mathbf{E}^i(\mathbf{r}') \right] d\Omega'$$

and

$$\mathbf{J}_p(\mathbf{r}) = j\omega\epsilon_0 \int (\epsilon(\mathbf{r} - \mathbf{r}') - \epsilon_1 \delta(\mathbf{r} - \mathbf{r}')) \quad (2.6)$$

$$\times \left[ \left( -j\omega\mu \int \underline{\mathbf{G}}_{ee}(\mathbf{r}', \mathbf{r}'') \cdot \mathbf{J}_{eq}(\mathbf{r}'') d\Omega'' \right) + \mathbf{E}^i(\mathbf{r}') \right] d\Omega'$$

for all  $\mathbf{r} \in \Omega$ , where  $\mathbf{J}_{eq} = \mathbf{J}_c + \mathbf{J}_p$ .

Equations (2.5) and (2.6) are what we term the direct convolution form integral equations, since they arise directly from the convolution forms (2.1)-(2.2). These involve computationally intensive six fold integrals. Furthermore, determining the space-domain material parameters  $\sigma(\mathbf{r})$  and  $\epsilon(\mathbf{r})$  from the momentum representations  $\sigma(\mathbf{q})$  and  $\epsilon(\mathbf{q})$  represents another three-fold integration unless the inversion to the space domain can be performed analytically. In the absence of that ability, the IEs involve nine-fold integrals, which may be impossible to compute from a practical standpoint.

It is worth noting that in the much simpler local isotropic case we have  $\mathbf{J}_c(\mathbf{r}) = (\sigma - \sigma_1) \mathbf{E}(\mathbf{r})$  and  $\mathbf{J}_p(\mathbf{r}) = j\omega\epsilon_0 (\epsilon - \epsilon_1) \mathbf{E}(\mathbf{r})$ , such that

$$\frac{\mathbf{J}_c(\mathbf{r})}{\sigma - \sigma_1} = -j\omega\mu \int \underline{\mathbf{G}}_{ee}(\mathbf{r}, \mathbf{r}') \cdot \mathbf{J}_{eq}(\mathbf{r}') d\Omega' + \mathbf{E}^i(\mathbf{r}) \quad (2.7)$$

and

$$\frac{\mathbf{J}_p(\mathbf{r})}{j\omega\epsilon_0(\epsilon - \epsilon_1)} = -j\omega\mu \int \underline{\mathbf{G}}_{ee}(\mathbf{r}, \mathbf{r}') \cdot \mathbf{J}_{eq}(\mathbf{r}') d\Omega' + \mathbf{E}^i(\mathbf{r}) \quad (2.8)$$

for all  $\mathbf{r} \in \Omega$ . These can simply be added together to form a single, three-fold IE,

$$\frac{\mathbf{J}_{eq}(\mathbf{r})}{\sigma_c} = -j\omega\mu \int \underline{\mathbf{G}}_{ee}(\mathbf{r}, \mathbf{r}') \cdot \mathbf{J}_{eq}(\mathbf{r}') d\Omega' + \mathbf{E}^i(\mathbf{r}), \quad (2.9)$$

where  $\sigma_c = (\sigma - \sigma_1) + j\omega\epsilon_0(\epsilon - \epsilon_1)$  is the combined composite complex conductivity that describes all conduction and polarization effects. Perhaps more often, (2.9) is expressed in terms of a combined effective relative permittivity  $\epsilon_c = \epsilon - \epsilon_1 + (\sigma - \sigma_1)/j\omega\epsilon_0$  as

$$\mathbf{E}(\mathbf{r}) = \left( \omega^2\mu\epsilon_0\epsilon_c \int \underline{\mathbf{G}}_{ee}(\mathbf{r}, \mathbf{r}') \cdot \mathbf{E}(\mathbf{r}') d\Omega' + \mathbf{E}^i(\mathbf{r}) \right), \quad (2.10)$$

for all  $\mathbf{r} \in \Omega$ , which is the usual volume integral equation for local penetrable scatterers [32].

Returning to the nonlocal case, we consider an ICWM constructed from imperfectly-conducting wires characterized by  $\epsilon_m = 1 - \omega_m^2/(\omega(\omega - j\Gamma))$ , where  $\omega_m$  and  $\Gamma$  are the plasma frequency and damping frequency of the metal, respectively. When homogenization is appropriate (i.e., when the wire period is much smaller than wavelength [9]), both conduction and polarization effects can be contained in a single nonlocal relative permittivity [8],

$$\underline{\epsilon}(\mathbf{q}, \omega) = \mathbf{1}\epsilon_h - \kappa \left( \mathbf{1} - \frac{1}{q^2 + l_0 \left( \frac{\epsilon_h k_p^2}{\epsilon_m - \epsilon_h} \frac{1}{f_v} - k_h^2 \right)} \mathbf{q}\mathbf{q} \right) \quad (2.11)$$

where

$$\kappa = \left( \frac{k_0^2}{k_p^2} - \frac{1}{\epsilon_m - \epsilon_h} \frac{1}{f_v} \right)^{-1}, \quad (2.12)$$

$f_v = \pi r^2/a^2$  is the volume fraction of the wires,  $r$  is the wire radius,  $a$  is the wire period,  $k_h = \omega\sqrt{\mu_0\epsilon_0\epsilon_h} = k_0\sqrt{\epsilon_h}$  is the wavenumber in the dielectric supporting the wires,  $k_p = \omega_p/c$  is the plasma wavenumber given by  $(k_p a)^2 \cong 2\pi/\ln\left(\frac{a^2}{4r(a-r)}\right) \cong$

$2\pi / (\ln(\frac{a}{2\pi r}) + 0.5275)$ ; see [8]-(11) for the exact expression, and  $l_0 = 3 / (1 + 2k_p^2/\beta_1^2)$ , where

$$\frac{1}{\beta_1^2} = 2 \left( \frac{a}{2\pi} \right)^2 \sum_{n=1}^{\infty} \frac{[J_0(\frac{2\pi r}{a}n)]^2}{n^2}, \quad (2.13)$$

and where  $J_0$  is the zeroth-order Bessel function. As discussed in [8], this expression is very accurate below the effective plasma frequency, which, for  $\varepsilon_h \sim 1$  is

$$\frac{1}{\omega_{p,eff}^2} = \varepsilon_h \left( \frac{1}{\omega_m^2 f_v} + \frac{1}{k_p^2 c^2} \right). \quad (2.14)$$

If  $\varepsilon_h$  differs considerably from unity the effective transverse permittivity is not Drude-like and is given by a quadratic form obtained from setting the transverse permittivity to zero. The isotropic wire medium permittivity (2.11) reduces to the simpler form [27]

$$\underline{\varepsilon}(\mathbf{q}, \omega) = \mathbf{1}\varepsilon_h - \frac{k_p^2}{k_0^2} \left( \mathbf{1} - \frac{1}{q^2 - l_0 k_h^2} \mathbf{q}\mathbf{q} \right) \quad (2.15)$$

when  $|\varepsilon_m| \rightarrow \infty$ , i.e., as the wire conductivity becomes infinite. The direct (conventional) method would consist of determining  $\underline{\varepsilon}(\mathbf{r})$  and using that in the six-fold IE (2.6); it appears that scattering from three-dimensional wire media has not been considered, likely because of this complication.

Note that the permittivity of (2.11) is given in the Fourier transform domain and taking its inverse Fourier transform will lead to

$$\frac{\underline{\varepsilon}(\mathbf{r})}{\varepsilon_0} = (\varepsilon_h - \kappa) \delta(\mathbf{r}) \mathbf{I} - \kappa \left\{ (3\hat{\mathbf{r}}\hat{\mathbf{r}} - \mathbf{I}) \left( \frac{1}{r^2} - \frac{\alpha}{ir} \right) - \alpha^2 \hat{\mathbf{r}}\hat{\mathbf{r}} \right\} \frac{e^{-j\alpha r}}{4\pi r}. \quad (2.16)$$

where  $\delta(\mathbf{r})$  is the Dirac delta function.

## 2.2 Integro-differential equation - the drift-diffusion approach

In [1] a transport treatment of a nonlocal wire medium was developed, leading to a drift diffusion equation that relates conduction current, electric field, and charge density as

$$\mathbf{J}_c(\mathbf{r}) = \sigma \mathbf{E}(\mathbf{r}) - D \nabla \rho_c(\mathbf{r}), \quad (2.17)$$

in which  $\sigma$  is the conductivity and  $D$  is the diffusion parameter. Although the material parameters  $\sigma$  and  $D$  are wavevector-independent, (2.17) is a nonlocal expression since the gradient samples the spatial region near the point  $\mathbf{r}$  [33].

The drift-diffusion equation originates from the Boltzmann's equation which is the model that governs the evolution of perfect gases in kinetic theory,

$$\frac{\partial f_e}{\partial t} + V_e \cdot \nabla_r f_e - \frac{e}{\hbar} (\mathbf{E}(\mathbf{r}, t) + V_e \times \mathbf{B}(\mathbf{r}, t)) \cdot \nabla_k f_e = \frac{f_e - f_{e,0}}{\tau_e} \quad (2.18)$$

where  $f_e = f_e(\mathbf{r}, \mathbf{k}, t)$  is the probability of finding an electron at position  $\mathbf{r}(t)$  at time  $t$  and having the momentum  $\mathbf{k}(t)$ .

The method to derive macroscopic (configuration space) variables from the microscopic (6-dimensional phase space) distribution function is to take velocity moments. The continuity equation comes from the zeroth moment of Boltzmann's equation,

$$\frac{\partial \rho(\mathbf{r}, t)}{\partial t} + \nabla_r \cdot \mathbf{J}^{\text{cond}}(\mathbf{r}, t) = 0 \quad (2.19)$$

which is an example of a conservation law

$$\frac{\partial \mathbf{F}}{\partial t} + \nabla_r \cdot \mathbf{G} = 0 \quad (2.20)$$

where  $\mathbf{F}$  is the density of a physical quantity and  $\mathbf{G}$  is its flux.

Transport equation comes from the first moment of Boltzmann's equation

$$n_\alpha m_\alpha \frac{\partial \mathbf{V}_\alpha}{\partial t} + \nabla \cdot \mathbf{P}_\alpha(\mathbf{r}, t) + n_\alpha m_\alpha \mathbf{V}_\alpha \cdot \nabla \mathbf{V}_\alpha - q_\alpha n_\alpha \langle \mathbf{E} + \mathbf{V}_\alpha \times \mathbf{B} \rangle = \quad (2.21)$$

$$m_\alpha \int \mathbf{v} \left( \frac{\partial f_\alpha}{\partial t} \right) d^3v$$

The second-order contributions  $\nabla \cdot \mathbf{P}_\alpha(\mathbf{r}, t)$ ,  $\mathbf{V}_\alpha \cdot \nabla \mathbf{V}_\alpha$  arise from terms containing the product  $\mathbf{V}\mathbf{V}$  or  $\mathbf{V} \cdot \mathbf{V}$ . The divergence  $\mathbf{P}$  contains information of inhomogeneity and viscosity of the plasma. Boltzmann's equation is semiclassical and its quantum parts come from momentum ( $\hbar k$ ) and Fermi-Dirac distribution

$$\mathbf{J} = q_e \sum \int V(\mathbf{k}) f(E(\mathbf{k})) \frac{d^3k}{4\pi^3}. \quad (2.22)$$

Linearization of transport equation yields to

$$\left( \frac{\partial}{\partial t} + \frac{1}{\tau} \right) \mathbf{J}^{cond}(\mathbf{r}, t) + \frac{k_B T}{m} \nabla \rho(\mathbf{r}, t) - \frac{q^2}{m} N \mathbf{E}(\mathbf{r}, t) = 0 \quad (2.23)$$

where

$$\mathbf{J}^{cond}(\mathbf{r}, t) = qNV(\mathbf{r}, t), \quad (2.24)$$

$$\rho = qn(\mathbf{r}, t). \quad (2.25)$$

Therefore, the drift diffusion equation will be obtained as

$$\mathbf{J}(\mathbf{r}, \omega) = \sigma(\omega) \mathbf{E}(\mathbf{r}, \omega) - D(\omega) \nabla \rho_c(\mathbf{r}, \omega), \quad (2.26)$$



$$D(\omega) = \frac{k_B T}{m(j\omega + \gamma)}, \quad (2.27)$$

$$\sigma(\omega) = \frac{ne^2}{m(j\omega + \gamma)}. \quad (2.28)$$

For the ICWM, the equivalent conductivity and diffusion parameters are [1]

$$\sigma = \sigma^{\text{ICWM}} = j\omega\epsilon_0 \left( \frac{1}{(\epsilon_m - \epsilon_h) f_V} - \frac{\omega^2}{\beta_p^2 c^2} \right)^{-1}, \quad (2.29)$$

$$D = D^{\text{ICWM}} = j\omega \left[ l_0 \left( \frac{\epsilon_h \beta_p^2}{(\epsilon_m - \epsilon_h) f_V} - \frac{\epsilon_h \omega^2}{c^2} \right) \right]^{-1}. \quad (2.30)$$

In this formulation, the response of the wire medium is the conduction plus polarization response, and if the wires are in the same material as the background environment ( $\epsilon_h = \epsilon_1$ ) there is no polarization response, in which case, using (2.17), Maxwell's equations, and continuity equation, we obtain

$$\mathbf{J}_c(\mathbf{r}, \omega) = \sigma \left[ -j\omega\mu \int \underline{\mathbf{G}}_{ee}(\mathbf{r}, \mathbf{r}') \cdot \mathbf{J}_c(\mathbf{r}') d\Omega' \right. \quad (2.31)$$

$$\left. + \mathbf{E}^i(\mathbf{r}) \right] + \frac{D}{j\omega} \nabla \nabla \cdot \mathbf{J}_c(\mathbf{r})$$

for all  $\mathbf{r} \in \Omega$ . We refer to this as the drift-diffusion (DD) result. This integro-differential formulation involves only three-fold integrals, and differentiation. For solutions involving the expansion of the conduction current in a set of basis functions, taking the derivative of the basis functions is very easy to implement; obviously, the chosen basis function should be twice-differentiable.

If the wires are supported by a material having permittivity different than the background permittivity, then we need to solve the coupled DD system [1]

$$\mathbf{J}_c(\mathbf{r}) = \sigma [\mathbf{E}^{sca}(\mathbf{r}) + \mathbf{E}^i(\mathbf{r})] + \frac{D}{j\omega} \nabla \nabla \cdot \mathbf{J}_c(\mathbf{r}), \quad (2.32)$$

$$\mathbf{J}_p(\mathbf{r}) = j\omega\varepsilon_0 (\varepsilon(\mathbf{r}) - 1) [\mathbf{E}^{sca}(\mathbf{r}) + \mathbf{E}^i(\mathbf{r})], \quad (2.33)$$

for all  $\mathbf{r} \in \Omega$ , where

$$\mathbf{E}^{sca}(\mathbf{r}) = -j\omega\mu \int \underline{\mathbf{G}}_{ee}(\mathbf{r}, \mathbf{r}') \cdot (\mathbf{J}_c(\mathbf{r}') + \mathbf{J}_p(\mathbf{r}')) d\Omega'. \quad (2.34)$$

In terms of complexity, these are three-fold equations, although they are coupled as also occurs for the local case of both permittivity and permeability contrast [34]. Note that these equations reduce to the usual local integral equations when  $D = 0$ .

In solving both the convolution-form IEs (2.5)-(2.6) and the transport-based DD form (2.31) or (2.32)-(2.33) the additional boundary condition that needs to be enforced is (see, e.g., [8; 1; 28])

$$\mathbf{J}_c \cdot \hat{\mathbf{n}} = 0, \quad (2.35)$$

where  $\hat{\mathbf{n}}$  is the unit vector normal to the surface of the region  $\Omega$ .

## Chapter 3

### Examples of scattering problems using the DD approach

[2; 3]

In the following, first we solve one-dimensional and two-dimensional isotropic examples involving both polarization and conduction current. Then, in the three-dimensional sphere examples we assume ( $\epsilon_h = \epsilon_1$ ) and therefore we only need to consider the conduction current, to avoid unnecessary complications and concentrate on the validation of the method. For the one-dimensional example, the new approach leads to a closed form analytical solution even though there are coupled polarization and conduction currents. In the two dimensional example, we show that for a two-dimensional wire medium slab the new approach gives the same results as the analytical solution in [8]. In the isotropic three dimensional example, we apply the formulation to the three-dimensional problem of a sphere of wire medium with different size and wire parameters, and we compare the result with a nonlocal Mie theory and measurement. The strong advantage of this new formulation is that for geometries other than spheres the integro-differential formulation yields a tractable method only involving three-fold integrals (of course, nonlocal Mie theory can only be used to validate the sphere geometry). In the anisotropic three dimensional example, we consider different cubical object with air as their host medium (therefore, only the conduction current is involved).

In the one- and two-dimensional examples, we have used the following identities which are obtained from the Leibniz rule

$$\frac{\partial^2}{\partial z^2} \int_0^L \frac{e^{-jk_z|z-z'|}}{2jk_z} J(z') dz' = (-k_z^2) \int_0^L \frac{e^{-jk_z|z-z'|}}{2jk_z} J(z') dz' - J(z), \quad (3.1)$$

$$\frac{\partial}{\partial z} \int_0^L \frac{e^{-jk_z|z-z'|}}{2jk_z} J(z') dz' = -\frac{1}{2} \left[ \int_0^z e^{-jk_z|z-z'|} J(z') dz' - \int_z^L e^{-jk_z|z-z'|} J(z') dz' \right]. \quad (3.2)$$

### 3.1 One dimensional isotropic example

A one-dimensional example based on the new transport formulation was considered in [1], and here we briefly summarize the result, as well as compare with a different method of solution. Consider a slab of ICWM extending to infinity in the x- and y-directions, and extending from  $-L$  to  $L$  in the z direction, as shown in Fig. 3.1.

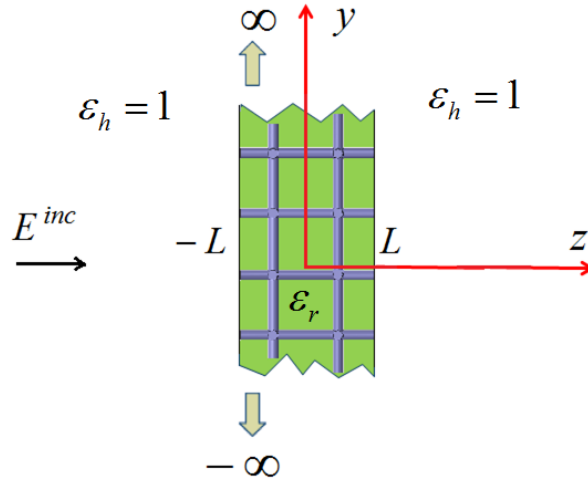


Figure 3.1: Wire medium slab with host relative permittivity of  $\epsilon_r$  in air.

We assume a quasi-static incident field  $E^{\text{inc}}$  which is constant and z-directed; this can be considered to be the field between capacitor plates far-removed from the slab. The wires are immersed in a dielectric host medium having relative permittivity  $\epsilon_r$ .

Reducing (2.32)-(2.34) to one dimension,

$$J_c(z) = \sigma [E^{\text{sca}}(z) + E^i(z)] + \frac{D}{j\omega} \frac{d^2}{dz^2} J_c(z), \quad (3.3)$$

$$J_p(z) = j\omega\varepsilon_0(\varepsilon_r - 1) [E^{sca}(z) + E^i(z)]. \quad (3.4)$$

Using (70) and (71) of [1], (2.34) simplifies to

$$E^{sca}(z) = -\frac{J_c(z) + J_p(z)}{j\omega\varepsilon_0} \quad (3.5)$$

and, upon substituting (3.5) into (2.32) and (2.33) and simplifying,

$$\frac{d^2}{dz^2} J_c - \frac{\sigma + j\omega\varepsilon_0\varepsilon_r}{\varepsilon_0\varepsilon_r D} J_c + \frac{j\omega\sigma}{\varepsilon_r D} E^{inc} = 0. \quad (3.6)$$

The solution of (3.6) subject to the boundary condition  $J_c(-L) = J_c(L) = 0$  is (3.7), from which (3.8) is found by use of the continuity equation.

$$J_c(z) = \frac{j\omega\sigma\varepsilon_0}{\sigma + j\omega\varepsilon_0\varepsilon_r} \left[ 1 - \frac{\cosh\left(\sqrt{\frac{\sigma + j\omega\varepsilon_0\varepsilon_r}{\varepsilon_0\varepsilon_r D}} z\right)}{\cosh\left(\sqrt{\frac{\sigma + j\omega\varepsilon_0\varepsilon_r}{\varepsilon_0\varepsilon_r D}} L\right)} \right] E^{inc}, \quad (3.7)$$

$$\rho(z) = \frac{\sigma\varepsilon_0}{\sigma + j\omega\varepsilon} \sqrt{\frac{\sigma + j\omega\varepsilon}{D\varepsilon}} \frac{\sinh\left(\sqrt{\frac{\sigma + j\omega\varepsilon}{D\varepsilon}} z\right)}{\cosh\left(\sqrt{\frac{\sigma + j\omega\varepsilon}{D\varepsilon}} L\right)} E^{inc}, \quad (3.8)$$

in which  $\sigma$  and  $D$  are given by (2.29) and (2.30), respectively. For perfect electrical conductor (PEC) wires, (3.7) and (3.8) simplify to

$$J_c(z) = \frac{j\omega\varepsilon_0\beta_p^2}{\beta_p^2 - \varepsilon_r\beta_0^2} \left[ 1 - \frac{\cosh\left(\sqrt{(\beta_p^2 - \beta_0^2\varepsilon_r)} l_0 z\right)}{\cosh\left(\sqrt{(\beta_p^2 - \beta_0^2\varepsilon_r)} l_0 L\right)} \right] E^{inc}, \quad (3.9)$$

$$\rho(z) = \beta_p^2\varepsilon_0 \sqrt{\frac{l_0}{\beta_p^2 - \beta_0^2\varepsilon_r}} \frac{\sinh\left(\sqrt{(\beta_p^2 - \beta_0^2\varepsilon_r)} l_0 z\right)}{\cosh\left(\sqrt{(\beta_p^2 - \beta_0^2\varepsilon_r)} l_0 L\right)} E^{inc}. \quad (3.10)$$

There does not seem to be a previous one-dimensional wire medium case with which to compare this solution. However, to demonstrate the applicability of this method we can consider a different diffusive (i.e., spatially-dispersive) material, an n-type semiconductor.

This has been considered in [7] under the same excitation as in Fig. 3.1. There, the solution was obtained by numerically solving coupled transport-Poisson (TP) equations. Here we consider the same material except using the proposed drift-diffusion model. For a semiconducting slab, (3.7) and (3.8) are valid using [33]

$$D = \frac{k_B T}{m_e (j\omega + \gamma)} \left[ \frac{\text{Am}^2}{C} \right], \quad (3.11)$$

$$\sigma = \frac{Ne^2}{m_e (j\omega + \gamma)} \left[ \frac{\text{S}}{m} \right], \quad (3.12)$$

where  $m_e$  is the effective electron mass,  $N$  is the donor doping density,  $T$  is temperature in Kelvin,  $k_B$  is Boltzmann's constant, and  $\gamma$  is the damping frequency. We consider a slab having thickness  $L = 100$  nm and  $f = 1$  THz, with  $\varepsilon_r = 11.9$ ,  $\gamma = 4.6$  THz,  $m_e = 0.26m_{e0}$  ( $m_{e0}$  is the free-space electron mass),  $T = 300$  K, and  $E^{\text{inc}} = 100$  V/m, which corresponds to the example in [7].

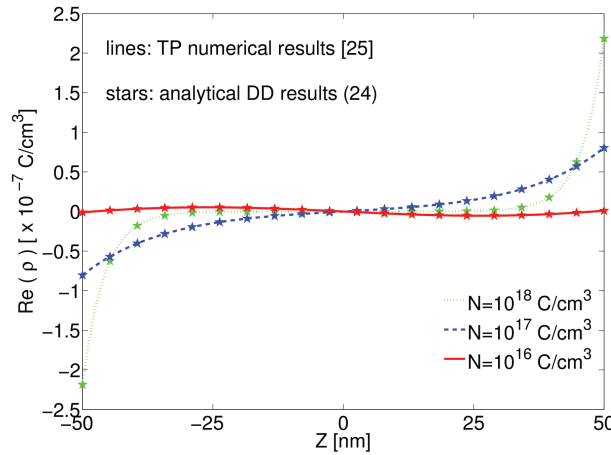


Figure 3.2: Real part of the charge distribution inside a nonlocal semiconductor slab for three different dopant densities using the drift diffusion formulation and the coupled transport-Poisson formulation [7].

Fig. 3.2 shows the real part of the charge distribution for three different dopant concentrations using (3.8) and its comparison with the results reported in [7] using a numerical solution of the coupled transport-Poisson equations. It is evident that the two methods

are in complete agreement.

## 3.2 Two dimensional isotropic example

As a two dimensional example, consider the geometry depicted in Fig. 3.3, where a TM-polarized wave is obliquely incident with angle of  $\theta_i$  on a slab of wire medium with equivalent parameters  $D$  and  $\sigma$ .

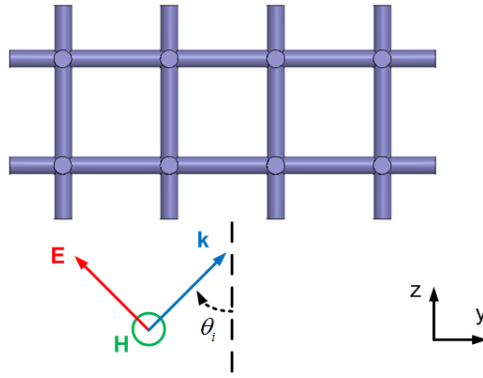


Figure 3.3: Wire medium slab infinite in the x and y directions.

After reducing (2.31) to two dimensions and using the collocation method we can find the induced current inside the slab and thus the scattered (reflected and transmitted) field. The reduced 2D equations are

$$\begin{aligned} \sigma E_y^i(z) = & \left\{ 1 + \frac{Dk_y^2}{j\omega} \right\} J_y(z) - \frac{\sigma k_y}{\omega \varepsilon_0} \frac{\partial}{\partial z} \int_0^L g(z, z') J_z(z') dz' \\ & + \frac{j\sigma k_z^2}{\omega \varepsilon_0} \int_0^L g(z, z') J_y(z') dz' - \frac{Dk_y}{\omega} \frac{\partial}{\partial z} J_z(z) \end{aligned} \quad (3.13)$$

$$\sigma E_z^i(z) = -\frac{Dk_y}{\omega} \frac{\partial}{\partial z} J_y(z) - \frac{\sigma k_y}{\omega \varepsilon_0} \frac{\partial}{\partial z} \int_0^L g(z, z') J_y(z') dz' +$$

$$\frac{j\sigma}{\omega\epsilon_0} \left( k^2 + \frac{\partial^2}{\partial z^2} \right) \int_0^L g(z, z') J_z(z') dz' + \left\{ 1 - \frac{D}{j\omega} \frac{\partial^2}{\partial z^2} \right\} J_z(z) \quad (3.14)$$

where

$$g(z, z') = g(z - z') = \frac{e^{-jk_z|z-z'|}}{2jk_z}, \quad (3.15)$$

$$k_y = k_0 \sin(\theta_i), \quad k_z = k_0 \cos(\theta_i) = \sqrt{k_1^2 - k_y^2}. \quad (3.16)$$

These were solved using the basis functions

$$J_y(z) = \sum_{n=1}^N a_n \sin\left(n \frac{\pi}{L} z\right) + \sum_{n=0}^N b_n \cos\left(n \frac{\pi}{L} z\right), \quad (3.17)$$

$$J_z(z) = \sum_{n=1}^N c_n \sin\left(n \frac{\pi}{L} z\right). \quad (3.18)$$

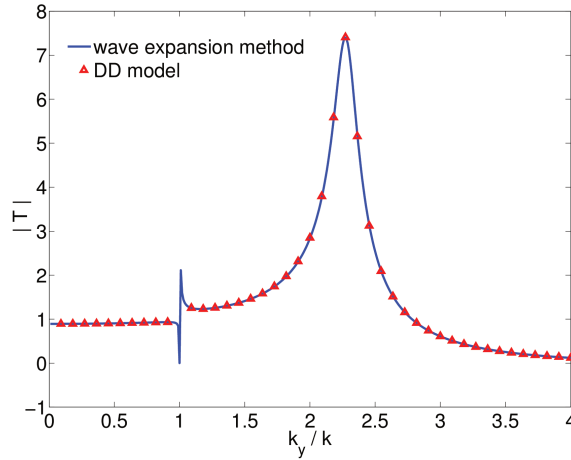


Figure 3.4: Comparison of the transmission coefficient of a wire medium slab using the integro-differential drift diffusion method and the wave expansion method of [8].

Fig. 3.4 shows the transmission coefficient as a function of  $k_y/k_0$  for a slab thickness of 276 nm,  $f = 76.1$  THz,  $\epsilon_h = 1$ , wire period  $a = 276$  nm,  $r = 8.25$  nm, and wire permittivity  $\epsilon_m = -810 - j50$  using the drift diffusion formulation and the wave expansion



method detailed in [8]; that approach [8] was to use (1.22) for permittivity and to define induced and scattered fields inside and outside of the slab with unknown coefficients, and match the boundary conditions. Note that the wave expansion method is only useful for regions having simple boundaries.

As a more general example, let us assume that the host dielectric of the wire medium has permittivity  $\varepsilon_r = 11.9$ . In this case we need to solve the coupled system of equations (2.32)-(2.34).

For the case of a conduction and polarization response, the reduction of (2.32)-(2.34) to two-dimensions is

$$\begin{aligned} \frac{J_y^{eq}(z) - J_y^c(z)}{j\omega\epsilon_0(\varepsilon - \varepsilon_1)} &= E_y^i(z) + \frac{(k_1^2 - k_y^2)}{j\omega\epsilon_0\varepsilon_1} \int_0^L g(z, z') J_y^{eq}(z') dz' \\ &+ \frac{q_y}{\omega\epsilon_0\varepsilon_1} \frac{\partial}{\partial z} \int_0^L g(z, z') J_z^{eq}(z') dz' \end{aligned} \quad (3.19)$$

$$\begin{aligned} \frac{J_z^{eq}(z) - J_z^c(z)}{j\omega\epsilon_0(\varepsilon - \varepsilon_1)} &= E_z^i(z) + \frac{k_y}{\omega\epsilon_0\varepsilon_1} \frac{\partial}{\partial z} \int_0^L g(z, z') J_y^{eq}(z') dz' \\ &+ \frac{1}{j\omega\epsilon_0\varepsilon_1} \left( k_1^2 + \frac{\partial^2}{\partial z^2} \right) \int_0^L g(z, z') J_z^{eq}(z') dz' \end{aligned} \quad (3.20)$$

where  $\mathbf{J}^{eq} = \mathbf{J}^c + \mathbf{J}^p$ . The basis functions used are

$$J_y^c = \sum_{n=-N}^N a_y e^{jn\frac{\pi}{L}(z-\frac{L}{2})}, \quad (3.21)$$

$$J_z^{con} = \sum_{n=-N}^N a_z e^{jn\frac{\pi}{L}(z-\frac{L}{2})}. \quad (3.22)$$

The internal electric fields of this slab are shown in Figs. 3.5 and 3.6, which demonstrate that the presented method is in complete agreement with the method of [8].

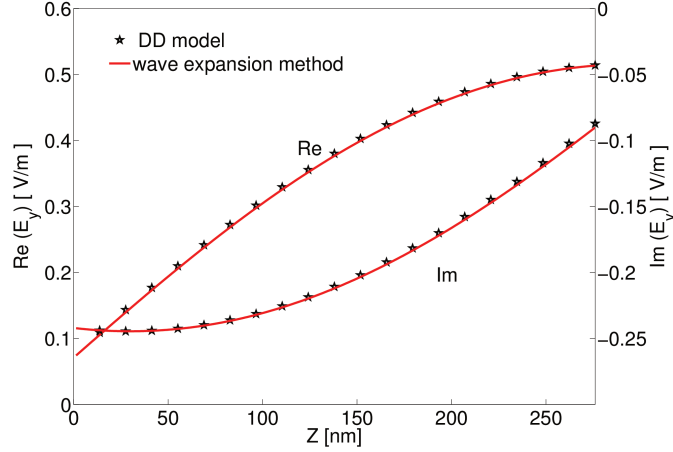


Figure 3.5: Internal field  $E_y$  of a wire medium slab using the integro-differential drift diffusion method and the wave expansion method of [8].

### 3.3 Three dimensional isotropic example

The two-dimensional example has been solved in the past using other methods. The most significant aspect of the presented formulation is the ability to solve three-dimensional wire-medium problems, which have not been previously treated. Towards this end, we consider spherical geometries since they are perhaps the simplest three-dimensional case, and they also admit a non-local Mie solution [35] which can be used for comparison. Of course, the presented integro-differential formulation is applicable to three-dimensional objects having arbitrary geometries, whereas the nonlocal Mie solution we use for comparison is only applicable to spheres.

#### 3.3.1 Formulation

Any realizable electromagnetic vector quantity inside a nonlocal material can be expanded in terms of

$$\mathbf{M}(\mathbf{r}, m, n) = \nabla \times \hat{\mathbf{r}} \psi_{\text{H}}(\mathbf{r}, m, n), \quad (3.23)$$

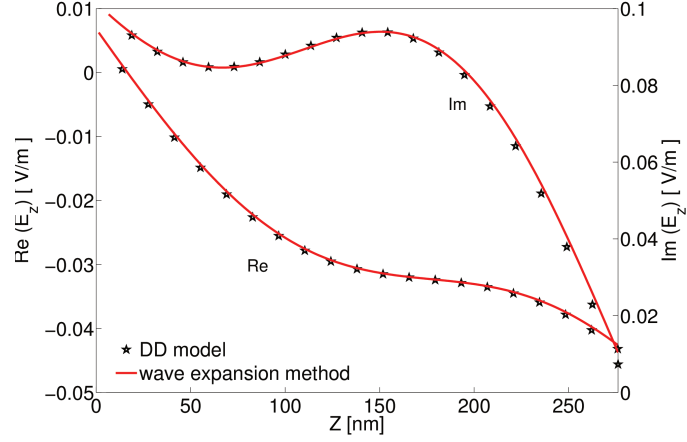


Figure 3.6: Internal field  $E_z$  of a wire medium slab using the integro-differential drift diffusion method and the wave expansion method of [8].

$$\mathbf{N}(\mathbf{r}, m, n) = \frac{1}{k_{\text{tr}}} \nabla \times \nabla \times \hat{\mathbf{r}} \psi_E(\mathbf{r}, m, n), \quad (3.24)$$

$$\mathbf{L}(\mathbf{r}, m, n) = \nabla \psi_\rho(\mathbf{r}, m, n), \quad (3.25)$$

in which

$$\psi_{H,E}(\mathbf{r}, m, n) = j_n(k_{\text{tr}} r) \begin{cases} \cos(m\varphi) \\ \sin(m\varphi) \end{cases} P_n^m(\cos(\theta)) \quad (3.26)$$

$$\psi_\rho(\mathbf{r}, m, n) = j_n(\alpha r) \begin{cases} \cos(m\varphi) \\ \sin(m\varphi) \end{cases} P_n^m(\cos(\theta)) \quad (3.27)$$

$$k_{\text{tr}} = \omega \sqrt{\mu \epsilon_0 \left( \epsilon - j \frac{\sigma}{\omega \epsilon_0} \right)}, \quad (3.28)$$

$$\alpha = j \sqrt{\frac{\sigma + j \omega \epsilon_0 \epsilon}{\epsilon_0 \epsilon D}}, \quad (3.29)$$

where  $P_n^m(x)$  is the associated Legendre polynomial and  $\mathbf{r}$  is the radial vector in spherical

coordinates;  $r = |\mathbf{r}|$ .

These set of functions form a complete set in  $L^2(\Omega)$  space where  $\Omega = [0, L]^3 \subset \mathbb{R}^3$ . The  $\mathbf{L}$  functions can be set to zero for expansions of magnetic fields, but are necessary for electric fields and conduction current expansions for  $\mathbf{r} \in \Omega$ . Here we include a brief discussion on the validity of the above expansion.

In [32] it is shown that if  $\psi_\rho$ ,  $\psi_{E,H}$  are eigenvectors of the scalar Helmholtz equation with eigenvalues of  $\alpha$  and  $k_{tr}$ , respectively, the  $\mathbf{M}$ ,  $\mathbf{N}$ , and  $\mathbf{L}$  functions as in (3.23)-(3.25) will form a complete set of functions in their respective space of functions satisfying the same boundary conditions (note that the pilot vector is set to be  $\hat{\mathbf{r}}$ ). Also, [32]

$$\nabla \times \nabla \times \mathbf{F} - k_{tr}^2 \mathbf{F} = 0; \quad \mathbf{F} = \mathbf{M}, \mathbf{N} \quad (3.30)$$

$$\mathbf{L} = \nabla \psi_\rho; \quad \nabla^2 \psi_\rho - \alpha^2 \psi_\rho = 0. \quad (3.31)$$

Therefore, we need to show

$$\alpha = -\frac{\sigma + j\omega\epsilon_0\epsilon}{\epsilon_0\epsilon D} \quad (3.32)$$

$$k_{tr}^2 = \omega^2 \mu \epsilon_0 \left( \epsilon - j \frac{\sigma}{\omega \epsilon_0} \right). \quad (3.33)$$

Starting from the drift diffusion equation (2.30) and using Maxwell's equations, it is straightforward to show

$$\nabla^2 \rho + \frac{\sigma + j\omega\epsilon_0\epsilon}{\epsilon_0\epsilon D} \rho = 0, \quad (3.34)$$

$$\nabla \times \nabla \times \mathbf{H} - \omega^2 \mu \epsilon_0 \left( \epsilon - j \frac{\sigma}{\omega \epsilon_0} \right) \mathbf{H} = 0, \quad (3.35)$$

$$\nabla \times \nabla \times \mathbf{E} - \omega^2 \mu \epsilon_0 \left( \epsilon - j \frac{\sigma}{\omega \epsilon_0} \right) \mathbf{E} = j \omega \mu D \nabla \rho. \quad (3.36)$$

By comparing (3.35) with (3.30), it is evident that  $k_{tr}$  is (3.33) since  $\mathbf{H}$  can be expanded in terms of  $\mathbf{M}$  and  $\mathbf{N}$  functions.

If we substitute  $\mathbf{L}$  for  $\mathbf{E}$  in (3.36) (we can do this since the  $\mathbf{M}$  and  $\mathbf{N}$  functions in the  $\mathbf{E}$  expansion make the left hand side of (3.36) zero),

$$\mathbf{L} = \frac{D}{\sigma + j \epsilon \omega} \nabla \rho, \quad (3.37)$$

and using (3.31),

$$\nabla \psi_\rho = \frac{D}{\sigma + j \epsilon \omega} \nabla \rho \quad (3.38)$$

so that

$$\psi_\rho \propto \rho. \quad (3.39)$$

Comparing (3.39), (3.34), and (3.31) results in (3.32).

Now, we consider an isotropic wire medium with an air host, and solve (2.31).

Assuming that the incident field is y-directed and is propagating in the z direction, we may simplify (3.26) and (3.27) as [29]

$$\psi_{H,E}(\mathbf{r}, n) = j_n(k_{tr}r) \sin(\varphi) P_n^1(\cos(\theta)), \quad (3.40)$$

$$\psi_\rho(\mathbf{r}, n) = j_n(\alpha r) \cos(\varphi) P_n^1(\cos(\theta)). \quad (3.41)$$

Therefore, a complete expansion for the conduction current is

$$\mathbf{J}_c(\mathbf{r}) = \sum_n (c_{1n} \mathbf{M}(\mathbf{r}, n) + c_{2n} \mathbf{N}(\mathbf{r}, n) + c_{3n} \mathbf{L}(\mathbf{r}, n)). \quad (3.42)$$

After inserting (3.42) into (2.31) and using the point matching technique, the unknown

expansion coefficients  $c_{in}$ ,  $i = 1, 2, 3$ , can be found.

Since the basis functions in (3.42) are obtained so that they satisfy the wave equation for nonlocal materials, we can solve (2.31) for one component (for example, the  $\theta$  or  $\varphi$  component) to obtain the unknown coefficients in (3.42). Here we pick the  $\theta$  directed component for two reasons:

- 1- none of the terms in (2.31) will be set to zero, and
- 2- the depolarizing dyadic contribution vanishes (as shown below), simplifying the calculation.

The dyadic Green's function is

$$\underline{\mathbf{G}}_{ee}(\mathbf{r}, \mathbf{r}') = \left\{ \left( 3\hat{\mathbf{R}}\hat{\mathbf{R}} - \underline{\mathbf{I}} \right) \left( \frac{1}{k^2 R^2} - \frac{1}{jkR} \right) - \left( \hat{\mathbf{R}}\hat{\mathbf{R}} - \underline{\mathbf{I}} \right) \right\} \frac{e^{-jkR}}{4\pi R} - \underline{\mathbf{L}} \frac{\delta(\mathbf{r} - \mathbf{r}')}{k^2} \quad (3.43)$$

where  $\mathbf{R} = \mathbf{r} - \mathbf{r}'$ . In the volume integral in (2.31), if we find the principal value of the integral by excluding a disc with thickness  $2\delta$  around point the  $\mathbf{r}$  inside the sphere of radius  $a_{\text{sphere}}$ , the integrals become  $\left( \int_0^{r-\delta} + \int_{r+\delta}^{a_{\text{sphere}}} \right) \int_0^\pi \int_0^{2\pi} \dots d\varphi d\theta dr$ , and the depolarizing dyadic will be [31]  $\underline{\mathbf{L}} = \hat{\mathbf{r}}\hat{\mathbf{r}}$ , and therefore  $\underline{\mathbf{L}} \cdot \mathbf{J}_c^\theta(\mathbf{r}) = 0$ .

Plugging (3.42) into (2.31) and simplifying, we have

$$\mathbf{J}_c(\mathbf{r}) \cdot \hat{\boldsymbol{\theta}} + \sum_n \left( c_{3n} \frac{D\alpha^2}{j\omega} \mathbf{L}(\mathbf{r}, n) \cdot \hat{\boldsymbol{\theta}} \right) + j\omega\mu\sigma \left( \int \hat{\boldsymbol{\theta}} \cdot \underline{\mathbf{G}}_{ee}(\mathbf{r}, \mathbf{r}') \cdot \mathbf{J}_c(\mathbf{r}') dV' \right) = \sigma E_i^\theta(r, \theta) \quad (3.44)$$

in which

$$\mathbf{M}(\mathbf{r}, n) = \frac{\cos(\varphi)}{\sin(\theta)} P_n^1(\cos(\theta)) j_n(\rho) \hat{\boldsymbol{\theta}} - \sin(\varphi) \frac{dP_n^1(\cos(\theta))}{d\theta} j_n(\rho) \hat{\boldsymbol{\varphi}}, \quad (3.45)$$

$$\mathbf{N}(\mathbf{r}, n) = \frac{j_n(\rho)}{\rho} \cos(\varphi) n(n+1) P_n(\cos(\theta)) \hat{\mathbf{r}} + \quad (3.46)$$

$$\frac{\cos(\varphi) dP_n^1(\cos(\theta))}{\rho d\theta} \frac{d}{d\rho} [\rho j_n(\rho)] \hat{\theta} - \frac{\sin(\varphi) P_n^1(\cos(\theta))}{\rho \sin(\theta)} \frac{d}{d\rho} [\rho j_n(\rho)] \hat{\varphi},$$

$$\mathbf{L}(\mathbf{r}, n) = \frac{d}{d\rho_t} [j_n(\rho_t)] \cos(\varphi) P_n^1(\cos(\theta)) \hat{r} - \quad (3.47)$$

$$\frac{j_n(\rho_t) \sin(\varphi)}{\rho_t \sin(\theta)} P_n^1(\cos(\theta)) \hat{\varphi} + \frac{1}{\rho_t} j_n(\rho_t) \cos(\varphi) \frac{dP_n^1(\cos(\theta))}{d\theta} \hat{\theta},$$

$$\rho = k_{tr} r, \quad \rho_t = \alpha r. \quad (3.48)$$

The obtained current is then used to calculate the scattered field using (2.34). The extinction cross section  $\sigma^{\text{ext}}$  of the object can be found using the optical theorem [36], which expresses the extinction cross section of an arbitrarily shaped object in terms of the forward scattered electric field,

$$\sigma^{\text{ext}} = \frac{4\pi}{k^2} \text{Im} \left( \frac{kr}{E_0 e^{jkr}} \mathbf{E}_s^{\parallel} \right), \quad (3.49)$$

where  $\mathbf{E}_s^{\parallel}$  is the far scattered field in the forward direction co-polarized with the incident field, and  $k$  is the wavenumber in the host medium external to the scatterer. The optical theorem is usually proved for objects consisting of local materials, but it is simple to repeat the same derivation for nonlocal materials.

Since we are going to compare results with Mie theory results too, the obtained the nonlocal Mie coefficients based on our parameters. The nonlocal Mie coefficients from [35] are

$$a_n = \frac{-j_n(\theta_h) \theta_{tr} j_n'(\theta_{tr}) + j_n(\theta_{tr}) \theta_h j_n'(\theta_h)}{h_n^{(+)}(\theta_h) \theta_{tr} j_n'(\theta_{tr}) - j_n(\theta_{tr}) \theta_h \left[ h_n^{(+)}(\theta_h) \right]'} \quad (3.50)$$

$$b_n = \frac{-\varepsilon_h j_n(\theta_h) ([\theta_{tr} j_n(\theta_{tr})]' + g_n) + \varepsilon_{tr} j_n(\theta_{tr}) [\theta_h j_n(\theta_h)]'}{h_n^{(+)}(\theta_h) \varepsilon_h ([\theta_{tr} j_n(\theta_{tr})]' + g_n) - j_n(\theta_{tr}) \varepsilon_{tr} [\theta_h h_n^{(+)}(\theta_h)]'}$$

in which

$$g_n = \frac{n(n+1) j_n(\theta_{tr}) j_n(q_0 a_{\text{sphere}})}{q_0 a_{\text{sphere}} j_n'(q_0 a_{\text{sphere}})} \left( \frac{\varepsilon_{tr}}{\varepsilon_b} - 1 \right), \quad (3.51)$$

$$q_0 = \sqrt{\frac{\sigma + j\omega\epsilon_0\varepsilon_b}{-D\epsilon_0\varepsilon_b}}; \quad \varepsilon_{tr} = \varepsilon_b - j\frac{\sigma}{\omega\epsilon_0} \quad (3.52)$$

where  $\theta_{tr} = k_0 A \sqrt{\varepsilon_{tr}}$ ,  $\theta_h = k_0 A \sqrt{\varepsilon_h}$ , and  $a_{\text{sphere}}$  is the radius of the sphere,  $\varepsilon_b$  is the relative permittivity of the dielectric host environment of the wires,  $\varepsilon_h$  is the relative permittivity of the medium surrounding the sphere,  $j_n$  is the spherical Bessel function, and  $h_n^{(+)}$  is the spherical Hankel function of the second kind. The usual local Mie theory is obtained by setting  $g_n = 0$ .

### 3.3.2 Simulation and measurement results

Six different wire medium spheres are examined in this section, as shown in Figs. 3.7-3.9. For convenience, we designate each sphere with a three part label  $D(\#1)a(\#2)d(\#3)$  in which #1 is the sphere diameter, #2 is the wire period, and #3 is the wire diameter, all in millimeters. For example, D50a4d1 indicates a sphere with diameter 50 mm, wire period 4 mm, and wire diameter 1 mm.

Note for purposes to be discussed later we fabricated two different D50a12d2 spheres as shown in Fig. 3.9. To distinguish between these we labeled one of them with an extra “C” at its end (i.e., D50a12d2C), which indicates that it has wires crossing at the center. Fig. 3.9 clarifies the difference between D50a12d2 and D50a12d2C.

The experimental configuration is shown in Fig. 3.10, consisting primarily of an



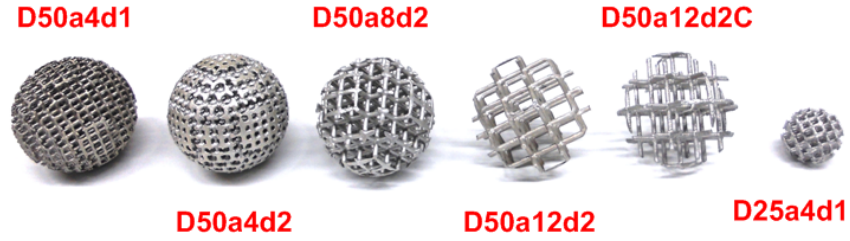


Figure 3.7: Wire medium spheres fabricated using a rapid prototyping machine. All spheres have 50 mm diameter except the far-right sphere, which has diameter 25 mm.

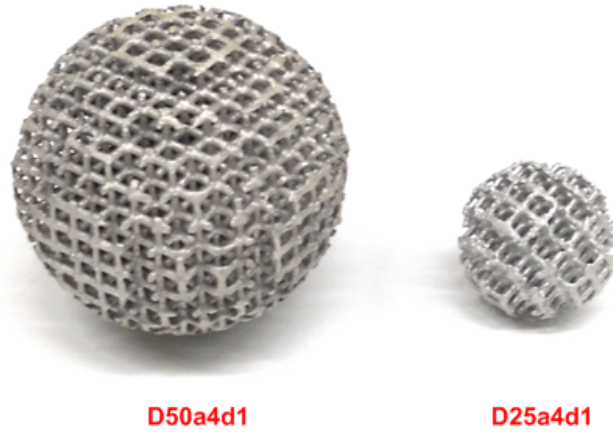


Figure 3.8: A close-up of the 50 mm and 25 mm wire medium spheres, both having period 4 mm.

anechoic box (C), two x-band horns (A), and an E8361A Agilent network analyzer (D). A Styrofoam pedestal (F) is used to support the sphere, and strings (B) are used to align the object between the horns. After measuring the forward scattered field using a 25 mm diameter brass sphere for calibration, the optical theorem (3.49) is used to find the extinction cross section, which is the same as the scattering cross section in our case since the spheres are considered lossless. In order to validate the measurement set-up, we considered a variety of metal and plastic spheres of different sizes. In all cases very good agreement with the known extinction cross section was found (one such validation is shown in Fig. 3.11).

Figure 3.11 shows the result of the measurement for the D50a4d1 sphere, and its comparison with the integro-differential DD method (2.31) using eight expansion terms,

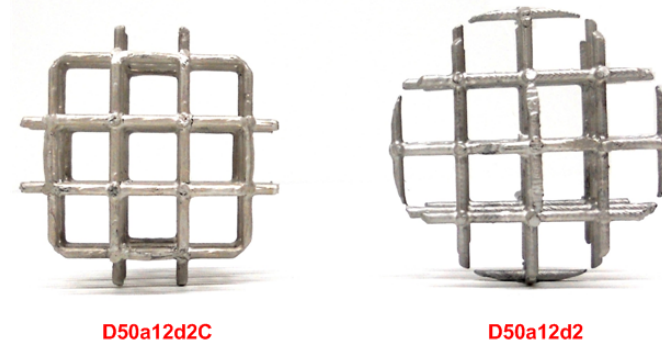


Figure 3.9: A close-up of the D40a12d2 and D40a12d2C spheres. Both have the same diameter, period, and wire thickness, but the latter sphere (C) has wires crossing at the center, whereas the other sphere does not.

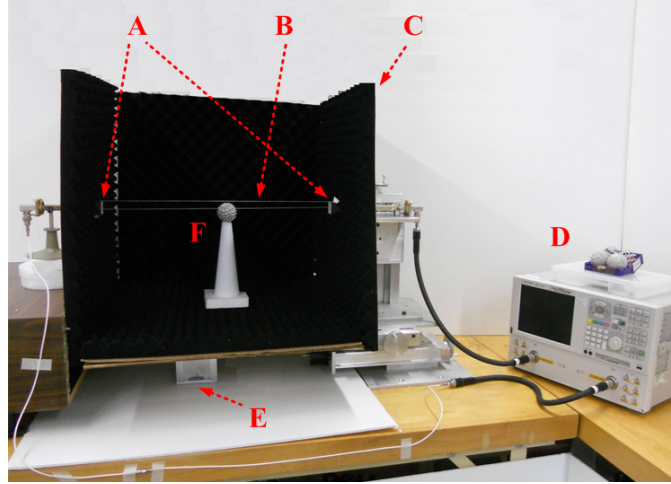


Figure 3.10: Measurement set-up. A: x-band horn antennas, B: strings for alignment, C: microwave absorbers, D: E8361A Network analyzer, E: height adjustment, F: WM sphere on a Styrofoam pedestal.

a nonlocal Mie theory solution [35] (some simple algebra allows us to express the parameters in [35] in terms of the diffusion constant and conductivity used here. For convenience, the final expressions for the nonlocal Mie coefficients are given in Appendix E), and a finite-difference time domain commercial code (Lumerical, [37]). We also show the result from a local Mie theory (setting  $D = 0$ ), which is not expected to be accurate but which we include just to show the influence of spatial dispersion. In Fig. 3.11 we also include, as validation of the measurement procedure, a comparison between measurement and Mie theory [29] for an ABSplus solid plastic sphere (which is a local material), also fabricated by the rapid prototyping machine. Measurements are only shown for 7 – 14

GHz, which is the approximate range of the horn antennas. Results are normalized by twice the geometric cross-sectional area of the spheres ( $a_{\text{sphere}}$  is the radius of the sphere), which is the high-frequency asymptotic value for PEC spheres [29].

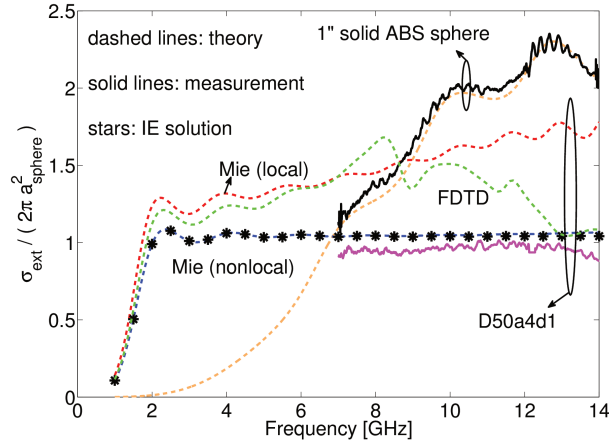


Figure 3.11: Normalized measured and theoretical extinction cross sections of the D50a4d1 wire medium sphere and of a plastic sphere.

From Fig. 3.11 it can be seen that the integro-differential DD formulation is in excellent agreement with the nonlocal Mie result (which can be considered to be an exact analytical solution for the homogenized problem), and these are in good agreement with the measurement. The local treatment of the wire medium (e.g., ignoring the wavevector dependence of the permittivity, or, equivalently, setting the diffusion parameter  $D = 0$ ) is seen to be in poor agreement with the nonlocal theory and measurement, highlighting the importance of spatial dispersion for this problem.

The FDTD commercial package was run on a 142 node computer cluster for the actual wire mesh sphere. However, it did not generate very accurate results, although great effort was made to obtain a convergent solution. Extensive numerical tests of spheres at various frequencies and for different wire periods showed that in some cases the FDTD solution more closely resembled the local solution, and in other cases it more closely resembled the nonlocal solution. The FDTD solution was often between the local and nonlocal results. We are not sure why the FDTD solution was inaccurate, although it can be noted that the geometry is relatively complex. Lumerical technical support indicated that our FDTD

model was correct, and should produce accurate results. Grid spacing was 0.1mm, which is  $0.0046\lambda$  at 14 GHz. We attempted to use other commercial codes for comparison as well, but these were not installed on the cluster and we did not have enough memory to run the simulations.

As a rough estimate of computation times, the Mie solution can be considered as essentially instantaneous, the integro-differential equation solution requires a few minutes for calculation, and the FDTD method typically takes 6-8 hours on the 142 node computer cluster.

Figure 3.12 shows similar results for the D25a4d1 sphere; note that in this case the normalized cross-section approaches its asymptotic value at approximately 5 GHz, as compared to 2 GHz for the larger sphere. Also, since this sphere is smaller, we only need four terms in (3.42) to solve the integro-differential DD equation. For this smaller sphere the agreement between nonlocal theory and measurement is still fairly good, but is somewhat poorer than for the larger 50 mm sphere. We attribute this to the fact that the larger sphere forms a relatively smoother spherical surface compared to the 25 mm sphere, in the sense that the ratio of wire period to cross-section circumference  $a/2\pi a_{\text{sphere}}$  is larger for the smaller sphere. As a result, the small sphere has a relatively rougher surface than the larger sphere, resulting in something of a “stair casing” effect.

### 3.3.3 Effect of wire period: breakdown of homogenization

The derivation of the equivalent diffusion parameter and conductivity of the ICWM in [1] is based on the ICWM permittivity [8]. This is derived assuming that  $ka \ll \pi$  where  $a$  is the wire lattice period and  $k$  is the wavenumber. The Bragg condition  $ka \ll \pi$  leads to  $a \ll c/2f$ , which leads to the Bragg frequency  $f_B = c/2a$ . We expect the homogenized model to break down as the wire period increases enough to violate this Bragg condition. Furthermore, it is discussed in [1] that (1.22) loses accuracy above the effective plasma frequency (1.25) (although a more complicated nonlocal permittivity can be used instead

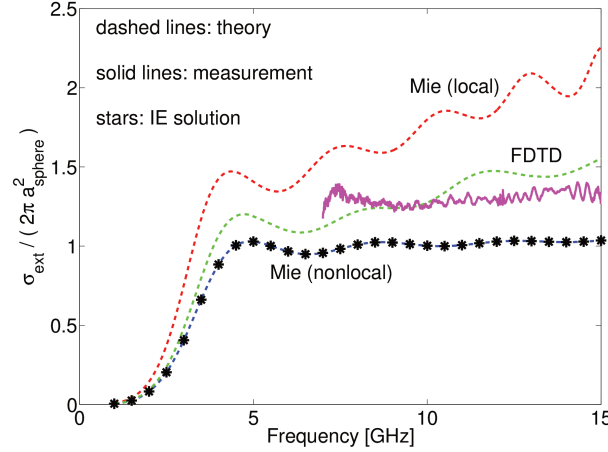


Figure 3.12: Normalized measured and theoretical extinction cross sections of the D25a4d1 sphere.

of (1.22), restoring accuracy above the plasma frequency [8], here we simply use (1.22)). In the following, different wire periods are considered and measurement results demonstrate that the homogenization approximation indeed starts to breakdown with increasing period, as expected.

To consider the breakdown of the homogenized isotropic permittivity, Fig. 3.13 shows measurement results for the D50a8d2, D50a12d2, and D50a12d2C spheres for the incident wave angle  $\theta = \varphi = 45^\circ$  (wires are parallel to x, y, and z axes). Although not previously discussed, for the smaller period ( $a = 4$  mm) spheres considered above the angle of the incident wave with respect to the wire orientation did not affect the measurement results, verifying that the material acts like an isotropic wire medium as expected (this is discussed in further detail below). However, for larger periods this is not the case, and so here we specify the orientation angle with respect to the wire axes. Comparing with Fig. 3.11, it is evident from Fig. 3.13 that for larger wire periods the agreement between theory and measurement becomes poorer at a much lower frequency than for the  $a = 4$  mm wire sphere, due to the lower plasma and Bragg frequencies. For  $a = 8$  mm and  $d = 2$  mm these are  $f_p = 16.56$  GHz and  $f_B = 18.75$  GHz, and for  $a = 12$  mm and  $d = 2$  mm,  $f_p = 9.13$  GHz and  $f_B = 12.5$  GHz. For comparison, in Fig. 3.11 where the

homogenization model is valid parameters are  $a = 4$  mm,  $d = 1$  mm,  $f_p = 33.12$  GHz, and  $f_B = 37.5$  GHz. Similarly, in Fig. 3.12,  $a = 4$  mm,  $d = 1$  mm,  $f_p = 57.45$  GHz, and  $f_B = 37.5$ .

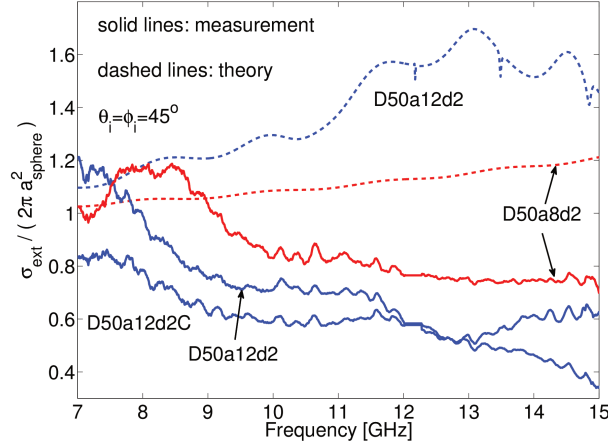


Figure 3.13: Normalized measured and theoretical extinction cross sections of the D50a8d2, D50a12d2, and D50a12d2C spheres. Because of the large wire periods, homogenization theory becomes inapplicable in most of the measurement range.

Finally, we consider the angle dependence of the wire medium spheres. Fig. 3.14 shows the measured extinction cross section for the D50a8d2, D50a12d2, and D50a12d2C spheres for different angles of the incident field with respect to the wire orientation. Two wire orientations are considered,  $\theta = 0^\circ$  and  $\theta = \varphi = 45^\circ$  (wires are aligned along the x, y, and z axes). Clearly, for the larger period spheres there is considerable angle dependence, whereas for the  $a = 4$  mm period sphere there is no angle dependence except at the highest measurement frequencies. Furthermore the D50a12d2, and D50a12d2C spheres, which have the same wire period and diameter but differ in their wire placement, show different responses. Again, this is indicative of a breakdown of homogenization theory when frequencies approach the plasma and Bragg frequencies.

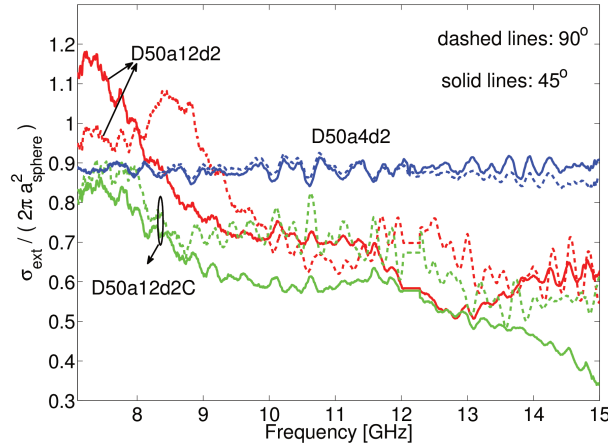


Figure 3.14: Normalized measured extinction cross section of the D50a4d2, D50a8d2, D50a12d2, and D50a12d2C spheres showing the angle dependance for the spheres having larger periods.

### 3.3.4 Fabrication process

The wire medium spheres were fabricated using a rapid prototyping machine (dimension Elite 3D Printer). The resulting “wires” are P430 ABSplus, which is a plastic material with  $\epsilon_r = 2.53$  (measured in our lab at 2.7 GHz using a split post dielectric resonator (SPDR) [38]). The resulting wire mesh is self-supporting, and is coated with silver paint [39] to form conducting wires. This process results in a several micron thick conductive layer on the insulating “wire” support, so we can consider the resulting wires as PEC at microwave frequencies. In Figs. 3.15, 3.16, and 3.17, some pictures of the fabrication process are shown for clarification.

## 3.4 Three dimensional anisotropic example

In this section we consider rectangular objects made of uniaxial wire media as shown in Fig. 3.18. Similar to the isotropic example, we use the transport model introduced in [1]-[2]. Based on this model, for a wire medium we can form a drift-diffusion equation that relates conduction current, electric field, and conduction charge density as

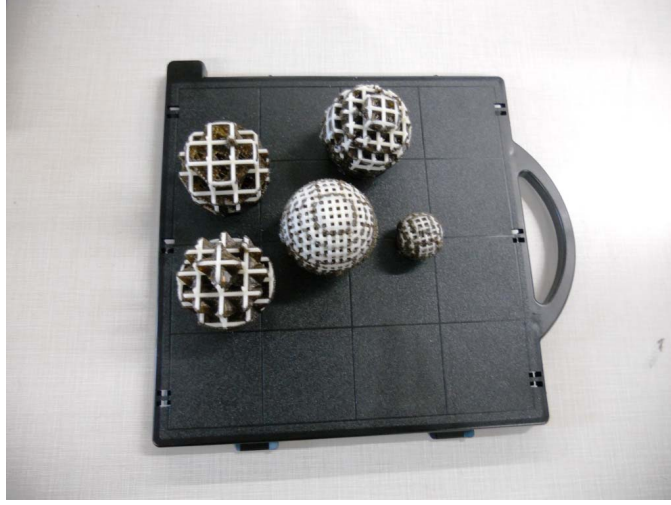


Figure 3.15: Spherical objects in the middle of the rapid prototyping process.

$$\mathbf{J}_c(\mathbf{r}) = \underline{\sigma} \cdot \mathbf{E}(\mathbf{r}) - \underline{\mathbf{D}} \cdot \nabla \rho_c(\mathbf{r}) \quad (3.53)$$

in which  $\sigma$  is the (local) conductivity and  $\mathbf{D}$  is the diffusion constant.

In [28], the homogenized nonlocal relative permittivity is obtained for a uniaxial wire medium with  $\varepsilon$ -negative rods as

$$\underline{\varepsilon}(\mathbf{q}) = \varepsilon_{xx} \hat{\mathbf{x}}\hat{\mathbf{x}} + \varepsilon_{xx} \hat{\mathbf{x}}\hat{\mathbf{x}} + \varepsilon_{xx}(\mathbf{q}) \hat{\mathbf{x}}\hat{\mathbf{x}}, \quad (3.54)$$

in which

$$\varepsilon_{xx} = \varepsilon_{xx} = 1 + \frac{2}{\frac{1}{f_V} \frac{(\varepsilon_m + \varepsilon_h)}{(\varepsilon_m - \varepsilon_h)} - 1}, \quad (3.55)$$

$$\varepsilon_{zz}(\mathbf{q}) = 1 + \frac{1}{\frac{1}{f_V} \frac{1}{(\varepsilon_m - \varepsilon_h)} - \frac{q^2 - q_z^2}{\beta_p^2}} \quad (3.56)$$

where  $\mathbf{q}$  is the wave vector in the spatial transform domain, wires are  $z$  directed,  $\varepsilon_m$  is the permittivity of wires,  $c$  is the speed of light,  $\varepsilon_h$  is the permittivity of the host medium,  $f_V$  is the volume fraction of wires ( $f_V = \frac{\pi d^2}{4p^2}$ ), and  $\beta_p$  is the plasma wavenumber as [28]



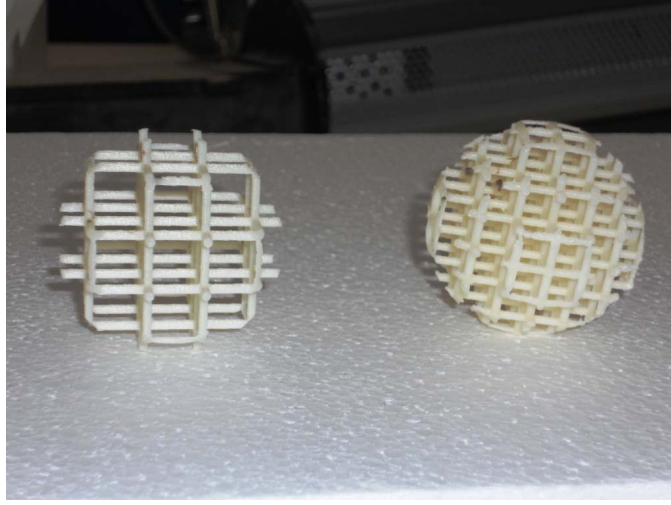


Figure 3.16: Spherical objects after fabrication by rapid prototyping and before coating by paint.

$$\beta_p = \omega_p \sqrt{\mu_0 \varepsilon_0 \varepsilon_h} \simeq \frac{1}{p} \sqrt{\frac{2\pi}{\ln\left(\frac{p}{\pi d}\right) + 0.5275}}. \quad (3.57)$$

As shown in [1], for the drift-diffusion model the equivalent conductivity and diffusion parameters are

$$\sigma_{zz} = j\omega\varepsilon_0 \left( \frac{1}{(\varepsilon_m - \varepsilon_h) f_V} - \frac{\omega^2}{\beta_p^2 c^2} \right)^{-1}, \quad (3.58)$$

$$D_{zz} = j\omega \left[ \left( \frac{\varepsilon_h \beta_p^2}{(\varepsilon_m - \varepsilon_h) f_V} - \frac{\varepsilon_h \omega^2}{c^2} \right) \right]^{-1}. \quad (3.59)$$

For a uniaxial wire medium, conduction current can flow only in the direction parallel to the wires. Therefore,  $\sigma$  and  $D$  are as (3.58) and (3.59) in the direction parallel to the wires and they are zero in the transverse direction with respect to wires. Turning the diffusion off by setting  $D = 0$ , (3.53) leads to the local Ohm's law. In the following we use  $d$  and  $p$  to denote wire thickness and period, respectively.

Assuming that the host medium of the wires is the same as the background, there is no polarization response, in which case using (3.53), Maxwell's equations, and the continuity equation, and noting that conduction current can only flow only parallel to wires (taken



Figure 3.17: The used silver paint and thinner for coating the objects.

parallel to the  $z$  axis in Cartesian coordinates), we obtain integral equation (IE)

$$J_z(\mathbf{r}) - \frac{D}{j\omega} \frac{d^2}{dz^2} J_z(\mathbf{r}) = \sigma E_z^{\text{inc}}(\mathbf{r}) - \sigma j\omega\mu \int G_{ee}^{zz}(\mathbf{r}, \mathbf{r}') J_z(\mathbf{r}') d\Omega'. \quad (3.60)$$

where

$$G_{ee}^{zz}(\mathbf{r}, \mathbf{r}') = -\hat{\mathbf{z}} \cdot \underline{\mathbf{L}} \cdot \hat{\mathbf{z}} \frac{\delta(\mathbf{r} - \mathbf{r}')}{k^2} + \frac{e^{-jkR}}{4\pi R} \times \left\{ \left( 3 \frac{(z - z')^2}{R^2} - 1 \right) \left( \frac{1 + jkR}{k^2 R^2} \right) - \left( \frac{(z - z')^2}{R^2} - 1 \right) \right\} \quad (3.61)$$

where  $\mathbf{R} = \mathbf{r} - \mathbf{r}'$  and  $\underline{\mathbf{L}}$  is the dyadic depolarization factor [31]. This integro-differential equation can be solved numerically by expanding  $J_z$  in terms of a set of complete basis functions for the given geometry. Since we are not allowing any surface charge build up on the surface of the object (due to diffusion), we need to enforce the following additional boundary condition [28],

$$\mathbf{J}_c \cdot \hat{\mathbf{n}} = 0 \quad (3.62)$$



Figure 3.18: A cubical object made of a uniaxial wire medium.

where  $\hat{n}$  is the outward unit vector normal to the surface of the object.

In the following we assume rectangular objects with the dimensions of  $a$ ,  $a$ , and  $b$  in  $x$ ,  $y$ , and  $z$ , respectively, and the incident wave is assumed to propagate in the  $y$  direction with its electric field component either parallel or perpendicular to the wires.

In order to solve (3.53) using the collocation method, we expand  $J_z(x, y, z)$  as

$$J_z(x, y, z) = \sum_{m=1}^M \sum_{n=1}^N \sum_{k=1}^K C_{mnk} P_{mn}(x, y) \sin\left(k \frac{\pi}{b} z\right) \quad (3.63)$$

in which

$$P_{mn}(x, y) = \begin{cases} 1 & \frac{(m-1)a}{M} \leq x < \frac{ma}{M}, \frac{(n-1)a}{N} \leq y < \frac{na}{N} \\ 0 & \text{otherwise} \end{cases} \quad (3.64)$$

are pulse functions,  $M$ ,  $N$ , and  $K$  are the number of expansion functions in the  $x$ ,  $y$ , and  $z$  directions respectively, and  $C_{mnk}$  are unknown coefficients of the expansion.

This current expansion is chosen so that the boundary condition (3.62) is satisfied. However, this expansion is complete only when a  $z$ -directed electric field is traveling in

the  $y$  or  $x$  direction and therefore there is a symmetry in the geometry with respect to the  $z = b/2$  plane. Otherwise, we need to consider both the sine and cosine functions in the expansion as

$$J_z(x, y, z) = \sum_{m=1}^M \sum_{n=1}^N \sum_{k=1}^K P_{mn}(x, y) \times \left[ C_{mnk} \sin\left(k \frac{\pi}{b} z\right) + D_{mnk} \cos\left(k \frac{\pi}{b} z\right) \right] \quad (3.65)$$

and enforce (3.62) at the  $z = 0$  and  $z = b$  planes.

After finding the equivalent currents for the object, we can use the optical theorem to calculate the extinction cross section using (3.49). The extinction cross section is obviously equal to the scattering cross section in our examples since objects are considered lossless. For a comparison we use a commercial simulation package which is based on the FDTD method [37]. The mesh size for all of the simulations is 0.1 mm, which is  $0.0046\lambda$  at 14 GHz.

Fabrication process for the objects is the same as in section 3.3.4. In Fig. 3.19, a sample of the fabricated wire medium objects is magnified. At the frequencies considered the object in Fig. 3.19 forms a cube of homogenized wire medium consisting of a 3-wire by 3-wire array with wire diameter  $d = 2$  mm, wire period  $p = 4$  mm, and wire length 12 mm. In order to make the wires self supporting, they are connected together at one end by a 1 mm thick plastic substrate (its scattered cross section is small compared to that of the wires).

The set up for the measurements is the same as the isotropic example (Fig. 3.19).

Figure 3.20 shows the normalized scattering cross section of the 3 by 3 wire object with substrate, for electric field polarization parallel to the wires. The good agreement between the full wave (CST) and measured results show the validity of the full wave simulation, which will be used for comparison with the drift-diffusion results. Figure 3.21 shows the normalized cross section of a 5 by 5 wire cubical object without the substrate. For the drift-diffusion IE, (3.60) and (3.65) are used with  $M = 3$ ,  $N = 4$ ,  $K = 3$ . The

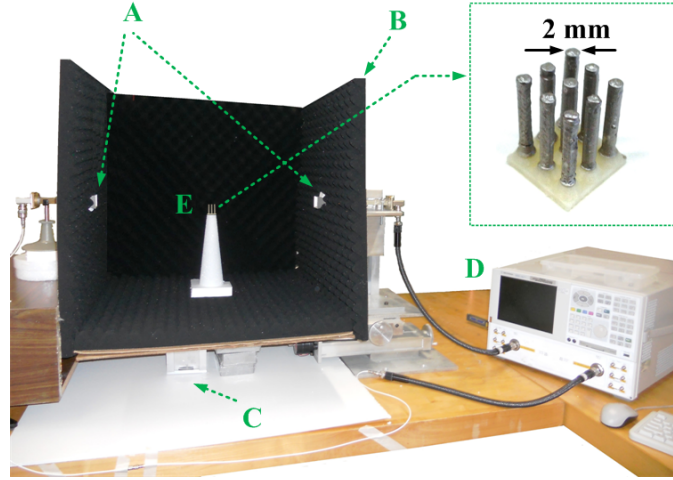


Figure 3.19: Measurement set-up. A: x-band horn antennas, B: microwave absorbers, C: height adjustment, D: E8361A Network analyzer, E: a fabricated 3 by 3 wire object on a Styrofoam pedestal. Wire diameter, period, and length are 2, 4, and 12 millimeters, respectively.

wire period, diameter and length are 4, 1, 20 millimeters, respectively. These parameters are chosen so that the homogenization approximations leading to the transport model are valid in the chosen frequency interval. It is evident from Fig. 3.21 that the drift-diffusion method is in good agreement with the full wave results. By comparing the full wave results in Fig. 3.20 and Fig. 3.21, a frequency shift of more than 1 GHz caused by the substrate is evident.

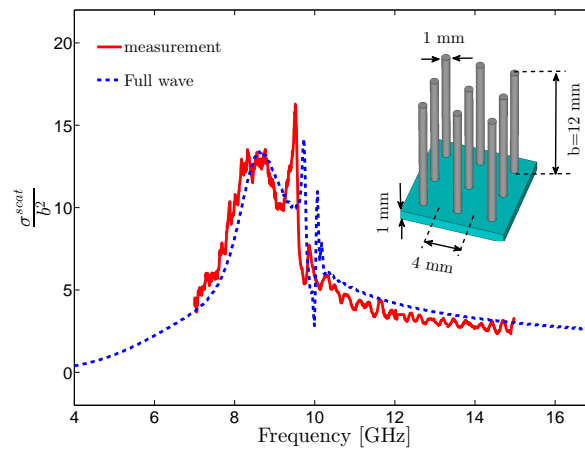


Figure 3.20: Normalized scattering cross section of a 3 by 3 wire cubical object with a 1 mm substrate. The incident electric field and wires are parallel.

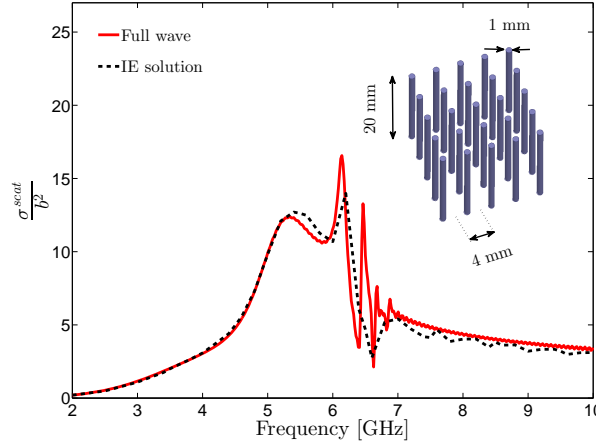


Figure 3.21: Normalized scattering cross section of a 5 by 5 wire cubical object.

### 3.5 Debye length and homogenization parameters

Having established the transport model, we can take the opportunity afforded by having a three-dimensional simulation to access how the wire parameters affect the validity of the homogenization. In deriving the homogenized results in Ref. [28], which lead to (3.58) and (3.59) without further approximation, the following assumptions were made: 1) the wire diameter is much smaller than the period,  $d \ll p$ , 2)  $|\mathbf{q}|p \ll 2\pi$ , where  $\mathbf{q}$  is the electromagnetic wavevector such that  $p \ll \lambda$  in the medium, 3) the wires are infinitely long, and 4) the medium is periodic. In this section we consider these aspects. Using the transport model, in Ref. [1] the Debye length of an artificial plasma formed by a wire medium is shown to be

$$\begin{aligned} \lambda_D &= 2\pi \left( \frac{\sigma + j\omega\varepsilon}{D\varepsilon} \right)^{-\frac{1}{2}} \simeq \frac{2\pi}{\beta_p} \sqrt{\frac{\varepsilon_r}{\varepsilon_h}} = \lambda_p \sqrt{\frac{\varepsilon_r}{\varepsilon_h}} \\ &= p \sqrt{2\pi \left( \ln \left( \frac{p}{\pi d} \right) + 0.5275 \right)} \sqrt{\frac{\varepsilon_r}{\varepsilon_h}} \end{aligned} \quad (3.66)$$

where in this case the Debye length is defined along the wires. The Debye length is weakly frequency dependent well below the plasma frequency, and is primarily dependent on the wire parameters; it is strongly dependent on period and weakly-dependent on wire

diameter, as shown in (3.66). Assuming  $\varepsilon_r \simeq \varepsilon_h$ , then if  $p \geq \pi d$  (which should be the case per the assumption above),  $\lambda_D \geq p$ .

The Debye length can be used to find the minimum size of a wire medium object that can be modeled using homogenization. The criteria that the Debye length be small compared to the physical size of the plasma (quasineutrality condition) is often taken as a basic condition for a system to behave as a plasma. For a wire medium we have a similar situation - if wire length  $b$  is less than the Debye length then the current induced on the wire will differ considerably from the case of a longer wire. This will lead to a per-unit-length polarizability that, for  $b < \lambda_D$ , differs from the infinite-wire case, violating a basic assumption of the homogenization. Accordingly, in order that a wire medium can be considered to be an artificial plasma, wires should be longer than the Debye length, which is, itself, typically larger than the wire period (and becomes increasingly larger than the period as period increases). For example,  $d = 1$  mm and  $p = 4$  mm, the Debye length is approximately 9 mm in the 1-15 GHz frequency interval. Therefore, in this case the object should be larger than 9 mm to have a meaningful artificial plasma. Moreover, the object should accommodate enough wires within itself so that the fundamental Floquet mode suffices for the homogenization. As an illustration of these two requirements, assumptions 3 and 4, cubical objects with sizes of 4, 8, 12, and 20 mm (which accommodate 1, 2, 3, and 5 wires respectively) are considered in Fig. 3.22 for  $p = 4$  mm, and  $d = 1$  mm. As wires are added the wire length was increased so that the objects remained cubical, hence the resonances shift to lower frequencies. As expected, for a single wire the homogenized model is not a good approximation since the object size is smaller than the Debye length and also the object is not periodic. However, even for a 2 by 2 wire array, having size  $8 \times 8 \times 8$  mm, the object is larger than the Debye length and the homogenized model applies to a fairly good approximation, still there is a large frequency shift between the results. Obviously, as the number of wires in the object increases, the homogenized model becomes more accurate. Further, measurements confirm that for a 5 by 5 wire object with

period 4 mm, homogenization becomes increasingly inaccurate as wire length is reduced below the Debye length as shown in Fig. 3.23. For  $b \simeq \lambda_D$ , the frequency shift (of the peak in the curves) is about 1 GHz. For  $b \simeq 1.5\lambda_D$  and  $b \simeq 2\lambda_D$ , the shift is 300 MHz, and less than 100 MHz, respectively.

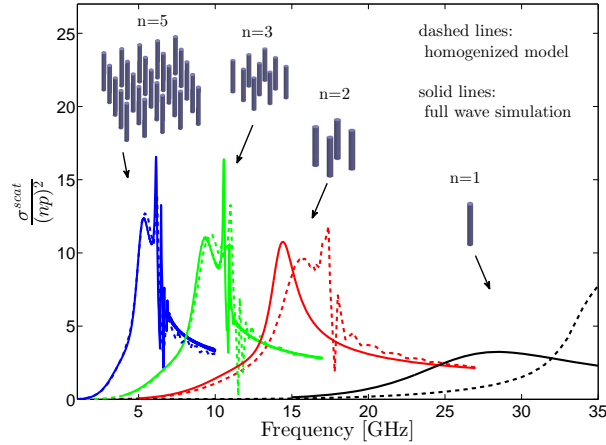


Figure 3.22: Normalized scattering cross section of cubical objects with different number of wires. Wires have  $p = 4$  mm and  $d = 1$  mm.

The homogenization used to derive (3.59) and (3.58) is based upon the assumption that only the fundamental Floquet mode is important and other modes are negligible. That is, the field variation over a period should be small, or  $p \ll \lambda$  (assumption 2). This condition will be automatically satisfied if the frequency of operation is well below the plasma frequency (as discussed in Ref. [28]). To illustrate this, rectangular 5 by 5 wire objects are considered with wire diameters of  $d = 1$  mm and periods of  $p = 4, 8$  and  $12$ , corresponding to plasma frequencies 33.1, 12.3, and 7.3 GHz, respectively. The length of all the wires are chosen to be 20 mm. Figure 3.24 shows the normalized scattering cross section, comparing full wave and homogenization theory (the  $p = 4$  mm results were shown in Fig. 3.21 and are not repeated here).

The results in Fig. 3.21 and Fig. 3.24 show that as  $p$  increases, the homogenization becomes less accurate. For  $p = 8$  mm the homogenization preserves the shape of the curve but shifts the frequency of the scattering. However, for  $p = 12$  mm, homogeniza-



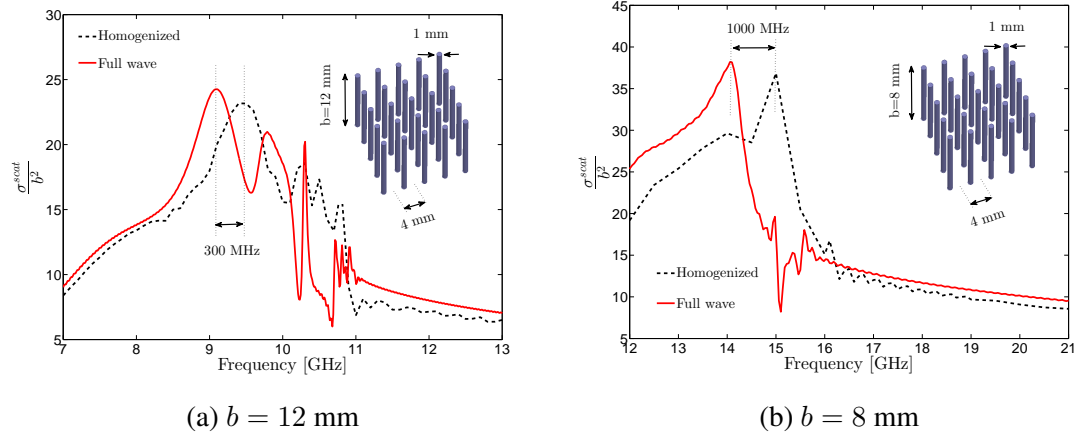


Figure 3.23: Normalized scattering cross section of 5 by 5 wire rectangular objects with  $d = 1$  and  $p = 4$  mm. For (a) wire length is well longer than the Debye length, whereas for (b) that is not the case, leading to a larger frequency shift between full wave and homogenized results.

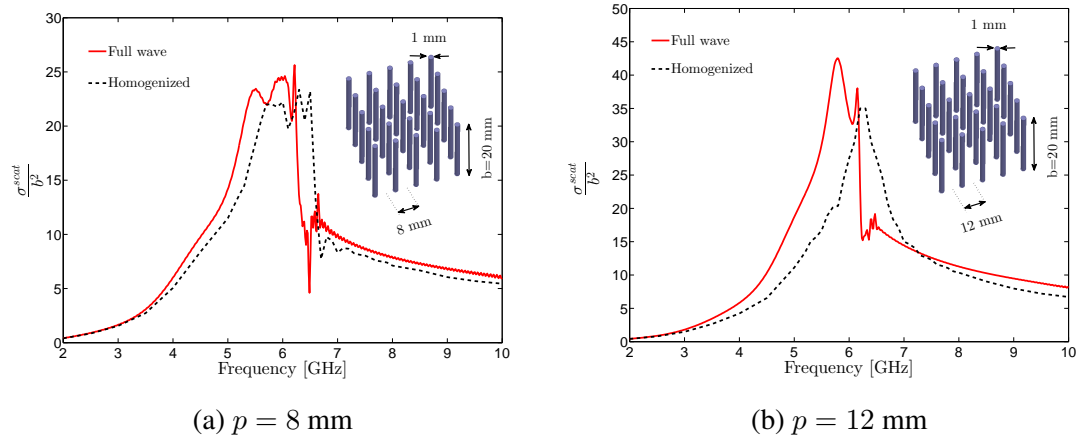


Figure 3.24: Normalized scattering cross section of 5 by 5 wire rectangular objects with  $d = 1$  and  $b = 20$  mm. The breakdown of homogenization with increasing period is evident.

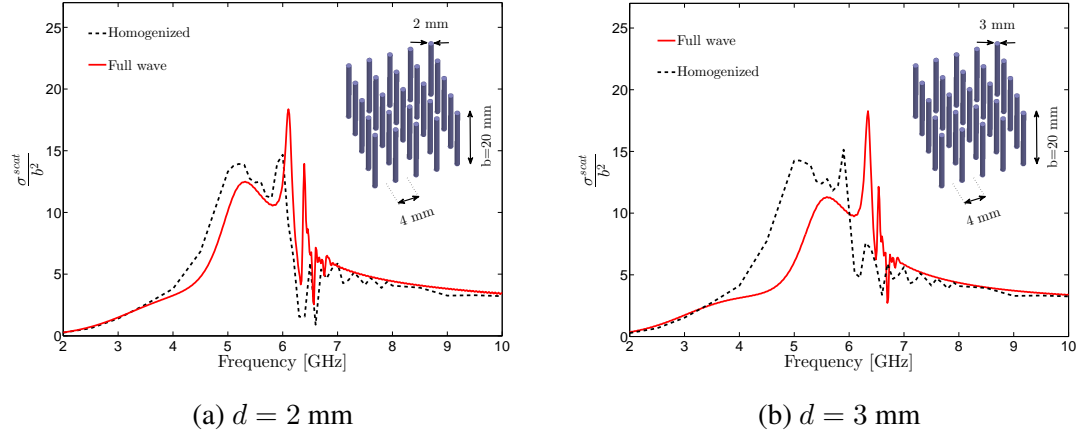


Figure 3.25: Normalized scattering cross section of 5 by 5 wire cubical objects with  $p = 4$  mm.

tion is no longer a reasonable approximation since the plasma frequency is lower than the operating frequency. This suggests that when the period is such that the plasma frequency is higher than the frequency of interest, the homogenized model can be used as a reasonable approximation.

Finally, to consider the effect of wire diameters, assumption 1, cubical 5 by 5 wire objects with  $p = 4$  mm and  $d = 1, 2$ , and 3 millimeters are investigated. Figure 3.25 shows the normalized scattering cross section for the  $d = 2$  and 3 mm cases (the results for  $d = 1$  mm were shown in Fig. 3.21). From Fig. 3.21 and Fig. 3.25 we conclude that by increasing  $d$ , homogenization will have a larger frequency shift in the scattering response from the actual results. However, it still keeps the shape of the curve. This suggests us that the homogenization is more sensitive to the period of wires than their thickness. This makes sense because increasing  $d$  will increase the plasma frequency (if the period is fixed) and will improve the homogenization approximation. However, the condition  $d/p \ll 1$  will be violated and the homogenization becomes worse. Because of these two phenomena acting in apposite directions we can expect that homogenization is less sensitive to wire thickness than to their period.

### 3.6 Appendix: More details on the formulations in 3.3

We can expand every vector function in the spherical coordinate (which correlates to an electromagnetic quantity) in term of the following complete set of basis functions:

$$\mathbf{M}(r, \theta, \varphi) = \nabla \times \mathbf{r}\psi(r, \theta, \varphi) \quad (3.67)$$

$$\mathbf{N}(r, \theta, \varphi) = \frac{1}{k} \nabla \times \nabla \times \mathbf{r}\psi(r, \theta, \varphi) \quad (3.68)$$

$$\mathbf{L}(r, \theta, \varphi) = \nabla \psi(r, \theta, \varphi) \quad (3.69)$$

where

$$\psi(r, \theta, \varphi) = j_n(\rho) \begin{cases} \cos(m\varphi) & P_n^m(\cos(\theta)) \\ \sin(m\varphi) & P_n^m(\cos(\theta)) \end{cases} \quad (3.70)$$

is the solution of homogeneous scalar Helmholtz equation in spherical coordinate,  $j_n(x)$  is spherical Bessel function and  $P_n^m(x)$  is associated Legendre polynomial

Explicit expressions for  $\mathbf{M}$ ,  $\mathbf{N}$ , and  $\mathbf{L}$  functions will be given later.

Using the expansion for conduction and total current (which is the sum of conduction and polarization currents), we have

$$\mathbf{J}_c = \sum_{m,n} \sum_{i=1}^6 (a_{imn}^c \mathbf{B}_{imn}) \quad (3.71)$$

$$\mathbf{J}_{eq} = \sum_{m,n} \sum_{i=1}^6 (a_{imn}^{eq} \mathbf{B}_{imn}) \quad (3.72)$$

where

$$\mathbf{B}_{1mn} = \mathbf{M}_{emn} \quad \mathbf{B}_{2mn} = \mathbf{M}_{omn} \quad \mathbf{B}_{3mn} = \mathbf{N}_{emn} \quad (3.73)$$

$$\mathbf{B}_{4mn} = \mathbf{N}_{omn} \quad \mathbf{B}_{5mn} = \mathbf{L}_{emn} \quad \mathbf{B}_{6mn} = \mathbf{L}_{omn}.$$

In the expansion, we use  $\rho = k_{tr}r$  for  $\mathbf{M}$  and  $\mathbf{N}$  functions and  $\rho = \alpha r$  for  $\mathbf{L}$  function. (This comes from Helmholtz equations that field and charge satisfy, details are at the end of this subsection) where,

$$\alpha = j\sqrt{\frac{\sigma + j\omega\varepsilon}{\varepsilon D}}, \quad (3.74)$$

$$k_{tr} = \omega\sqrt{\mu\left(\varepsilon - \frac{i\sigma}{\omega}\right)}, \quad (3.75)$$

and  $k$  is wavenumber in the scatterer.

Then, we find unknowns  $a_{imn}$  by solving the following set of equations simultaneously.

$$\begin{aligned} &\left(\mathbf{J}_c(r, \theta) - \frac{D}{j\omega} \nabla \nabla \cdot \mathbf{J}_c(r, \theta)\right) = \\ &-j\omega\mu\sigma \left(\int \underline{\mathbf{G}}_{ee}(\mathbf{r}, \mathbf{r}') \cdot \mathbf{J}_{eq}(\mathbf{r}') dV' - \frac{\underline{\mathbf{L}} \cdot \mathbf{J}_{eq}(\mathbf{r})}{k^2}\right) + \sigma \mathbf{E}^i(r, \theta), \end{aligned} \quad (3.76)$$

$$\begin{aligned} &\mathbf{J}_{eq}(\mathbf{r}) - \mathbf{J}_c(\mathbf{r}) = \\ &j\omega(\varepsilon - \varepsilon_0) \left[-j\omega\mu \left(\int \underline{\mathbf{G}}_{ee}(\mathbf{r}, \mathbf{r}') \cdot \mathbf{J}_{eq}(\mathbf{r}') dV' - \frac{\underline{\mathbf{L}} \cdot \mathbf{J}_{eq}(\mathbf{r})}{k^2}\right) + \mathbf{E}^i(r, \theta)\right]. \end{aligned} \quad (3.77)$$

Which leads to

$$\left(\mathbf{J}_c(r, \theta) - \frac{D}{j\omega} \nabla \nabla \cdot \mathbf{J}_c(r, \theta)\right) = \sigma \frac{\mathbf{J}_{eq}(\mathbf{r}) - \mathbf{J}_c(\mathbf{r})}{j\omega(\varepsilon - \varepsilon_0)}, \quad (3.78)$$

$$\begin{aligned} &\mathbf{J}_{eq}(\mathbf{r}) - \mathbf{J}_c(\mathbf{r}) = \\ &j\omega(\varepsilon - \varepsilon_0) \left[-j\omega\mu \left(\int \underline{\mathbf{G}}_{ee}(\mathbf{r}, \mathbf{r}') \cdot \mathbf{J}_{eq}(\mathbf{r}') dV' - \frac{\underline{\mathbf{L}} \cdot \mathbf{J}_{eq}(\mathbf{r})}{k^2}\right) + \mathbf{E}^i(r, \theta)\right]. \end{aligned} \quad (3.79)$$

Now, the first equation gives us:

$$\left( \sum_{m,n} \sum_{i=1}^6 (a_{imn}^c \mathbf{B}_{imn}) - \frac{D}{j\omega} \nabla \nabla \cdot \sum_{m,n} \sum_{i=1}^6 (a_{imn}^c \mathbf{B}_{imn}) \right) = \sigma \frac{\mathbf{J}_{eq}(r, \theta) - \sum_{m,n} \sum_{i=1}^6 (a_{imn}^c \mathbf{B}_{imn})}{j\omega (\varepsilon - \varepsilon_0)}, \quad (3.80)$$

or

$$\begin{aligned} \frac{j\omega (\varepsilon - \varepsilon_0) + \sigma}{\sigma} \sum_{m,n} \sum_{i=1}^6 (a_{imn}^c \mathbf{B}_{imn}) = \\ \frac{(\varepsilon - \varepsilon_0) D}{\sigma} \nabla \nabla \cdot \sum_{m,n} \sum_{i=1}^6 (a_{imn}^c \mathbf{B}_{imn}) + \mathbf{J}_{eq}(r, \theta). \end{aligned} \quad (3.81)$$

whihc simplifies to

$$\begin{aligned} \frac{j\omega (\varepsilon - \varepsilon_0) + \sigma}{\sigma} \sum_{m,n} \sum_{i=1}^6 (a_{imn}^c \mathbf{B}_{imn}) = \\ - \frac{(\varepsilon - \varepsilon_0) D \alpha_n^2}{\sigma} \sum_{m,n} \sum_{i=5}^6 (a_{imn}^c \mathbf{B}_{imn}) + \mathbf{J}_{eq}(r, \theta). \end{aligned} \quad (3.82)$$

For  $1 \leq i \leq 4$

$$a_{imn}^{eq} = \frac{j\omega (\varepsilon - \varepsilon_0) + \sigma}{\sigma} (a_{imn}^c), \quad (3.83)$$

and for  $5 \leq i \leq 6$

$$\left( \frac{j\omega (\varepsilon - \varepsilon_0) + \sigma}{\sigma} + \frac{(\varepsilon - \varepsilon_0) D \alpha_n^2}{\sigma} \right) a_{imn}^c = a_{imn}^{eq}. \quad (3.84)$$

In Summary,

$$a_{imn}^c = \frac{\sigma}{j\omega (\varepsilon - \varepsilon_0) + \sigma + (\varepsilon - \varepsilon_0) D \alpha_n^2} a_{imn}^{eq} \quad (3.85)$$

$$D_i = \begin{cases} D & 5 \leq i \leq 6 \\ 0 & 1 \leq i \leq 4 \end{cases} \quad (3.86)$$

Therefore, we have the following integral equation,

$$\mathbf{J}_{eq}(\mathbf{r}) - \mathbf{J}_c(\mathbf{r}) = j\omega(\varepsilon - \varepsilon_0) \left[ -j\omega\mu \left( \int \underline{\mathbf{G}}_{ee}(\mathbf{r}, \mathbf{r}') \cdot \mathbf{J}_{eq}(\mathbf{r}') dV' - \frac{\underline{\mathbf{L}} \cdot \mathbf{J}_{eq}(\mathbf{r})}{k^2} \right) + \mathbf{E}^i(r, \theta) \right], \quad (3.87)$$

leading to

$$\sum_{m,n} \sum_{i=1}^6 \left( a_{imn}^{eq} \left( \frac{j\omega(\varepsilon - \varepsilon_0) + (\varepsilon - \varepsilon_0) D_i \alpha_{in}^2}{j\omega(\varepsilon - \varepsilon_0) + \sigma + (\varepsilon - \varepsilon_0) D_i \alpha_{in}^2} \right) \mathbf{B}_{imn} \right) = \omega^2 \mu (\varepsilon - \varepsilon_0) \sum_{m,n} \sum_{i=1}^6 a_{imn}^{eq} \left[ \left( \int \underline{\mathbf{G}}_{ee}(\mathbf{r}, \mathbf{r}') \cdot \mathbf{B}_{imn} dV' - \frac{\underline{\mathbf{L}} \cdot \mathbf{B}_{imn}}{k^2} \right) \right] + j\omega(\varepsilon - \varepsilon_0) \mathbf{E}^i(r, \theta). \quad (3.88)$$

We only need to solve this equation for one of the components ( $r$ ,  $\theta$ , or  $\varphi$ ) and find  $a_{imn}^{eq}$ , then we have the solution for all of the components.

Keeping only the theta component,

$$\sum_{m,n} \sum_{i=1}^6 \left( a_{imn}^{eq} \left( \frac{j\omega(\varepsilon - \varepsilon_0) + (\varepsilon - \varepsilon_0) D_i \alpha_{in}^2}{j\omega(\varepsilon - \varepsilon_0) + \sigma + (\varepsilon - \varepsilon_0) D_i \alpha_{in}^2} \right) \mathbf{B}_{imn}^\theta \right) = \omega^2 \mu (\varepsilon - \varepsilon_0) \sum_{m,n} \sum_{i=1}^6 a_{imn}^{eq} \left[ \left( \int \hat{\theta} \cdot \underline{\mathbf{G}}_{ee}(\mathbf{r}, \mathbf{r}') \cdot \mathbf{B}_{imn} dV' \right) \right] + j\omega(\varepsilon - \varepsilon_0) \mathbf{E}_i^\theta(r, \theta). \quad (3.89)$$

We can solve the above equation using collocation method.

Then, if we are looking for the charge density,

$$\rho = -\frac{1}{j\omega} \nabla \cdot \mathbf{J}_c = -\frac{1}{j\omega} \nabla \cdot \left( \sum_{m,n} \sum_{i=1}^6 (a_{imn}^c \mathbf{B}_{imn}) \right) = \frac{1}{j\omega} \left( \sum_{m,n} \sum_{i=5}^6 \frac{\sigma - j\omega(\varepsilon - \varepsilon_0)}{(\varepsilon - \varepsilon_0) \alpha_n^2 D_i + \sigma} a_{imn}^e \alpha_n^2 (j_n(\rho_t) \cos(m\varphi) P_n^m(\cos(\theta))) \right), \quad (3.90)$$

and if we are looking for the scattered field,

$$\mathbf{E}^{\text{sca}} = -j\omega\mu \sum_{m,n} \sum_{i=1}^6 a_{imn}^c \left( \int \mathbf{G}_{ee}(\mathbf{r}, \mathbf{r}') \cdot \mathbf{B}_{imn}(\mathbf{r}') dV' \right). \quad (3.91)$$

### Detailed bases functions

$$M_{emn} = \frac{-m}{\sin(\theta)} \sin(m\varphi) P_n^m(\cos(\theta)) j_n(\rho) \hat{\theta} - \cos(m\varphi) \frac{dP_n^m(\cos(\theta))}{d\theta} j_n(\rho) \hat{\varphi} \quad (3.92)$$

$$M_{omn} = \frac{m}{\sin(\theta)} \cos(m\varphi) P_n^m(\cos(\theta)) j_n(\rho) \hat{\theta} - \sin(m\varphi) \frac{dP_n^m(\cos(\theta))}{d\theta} j_n(\rho) \hat{\varphi} \quad (3.93)$$

$$N_{emn} = \frac{j_n(\rho)}{\rho} \cos(m\varphi) n(n+1) P_n^m(\cos(\theta)) \hat{r} + \cos(m\varphi) \frac{dP_n^m(\cos(\theta))}{d\theta} \frac{1}{\rho} \frac{d}{d\rho} [\rho j_n(\rho)] \hat{\theta} \\ - m \sin(m\varphi) \frac{P_n^m(\cos(\theta))}{\sin(\theta)} \frac{1}{\rho} \frac{d}{d\rho} [\rho j_n(\rho)] \hat{\varphi} \quad (3.94)$$

$$N_{omn} = \frac{j_n(\rho)}{\rho} \sin(m\varphi) n(n+1) P_n^m(\cos(\theta)) \hat{r} + \sin(m\varphi) \frac{dP_n^m(\cos(\theta))}{d\theta} \frac{1}{\rho} \frac{d}{d\rho} [\rho j_n(\rho)] \hat{\theta} \\ + m \cos(m\varphi) \frac{P_n^m(\cos(\theta))}{\sin(\theta)} \frac{1}{\rho} \frac{d}{d\rho} [\rho j_n(\rho)] \hat{\varphi} \quad (3.95)$$

$$L_{emn} = \frac{d}{d\rho_t} [j_n(\rho_t)] \cos(m\varphi) P_n^m(\cos(\theta)) \hat{r} - \frac{m}{\rho_t \sin(\theta)} j_n(\rho_t) \sin(m\varphi) P_n^m(\cos(\theta)) \hat{\varphi} \\ + \frac{1}{\rho_t} j_n(\rho_t) \cos(m\varphi) \frac{dP_n^m(\cos(\theta))}{d\theta} \hat{\theta} \quad (3.96)$$

$$\begin{aligned}
L_{omn} = & \frac{d}{d\rho_t} [j_n(\rho_t)] \sin(m\varphi) P_n^m(\cos(\theta)) \hat{r} + \frac{m}{\rho_t \sin(\theta)} j_n(\rho_t) \cos(m\varphi) P_n^m(\cos(\theta)) \hat{\varphi} \\
& + \frac{1}{\rho_t} j_n(\rho_t) \sin(m\varphi) \frac{dP_n^m(\cos(\theta))}{d\theta} \hat{\theta}
\end{aligned} \tag{3.97}$$

Where, where  $\rho = kr$  and  $\rho_t = \alpha r$ .

### Detailed Green's function components

$$\underline{\mathbf{L}} = \hat{\mathbf{r}}\hat{\mathbf{r}} \tag{3.98}$$

$$\underline{\mathbf{G}}_{ee}(\mathbf{r}, \mathbf{r}') = g(\mathbf{r}, \mathbf{r}') \left\{ \left( 3\hat{\mathbf{R}}\hat{\mathbf{R}} - \underline{\mathbf{I}} \right) \left( \frac{1}{k^2 R^2} - \frac{1}{jkR} \right) - \left( \hat{\mathbf{R}}\hat{\mathbf{R}} - \underline{\mathbf{I}} \right) \right\} \tag{3.99}$$

$$R = \sqrt{r^2 + r'^2 - 2rr'(\cos(\theta)\cos(\theta') + \sin(\theta)\sin(\theta')\cos(\varphi - \varphi'))} \tag{3.100}$$

$$\hat{\varphi}' \cdot \hat{\mathbf{r}} = \sin(\theta) \sin(\varphi - \varphi') \tag{3.101}$$

$$\hat{\varphi} \cdot \hat{\mathbf{r}}' = \sin(\theta') \sin(\varphi' - \varphi) \tag{3.102}$$

$$\hat{\theta} \cdot \hat{\varphi}' = \cos(\theta) \sin(\varphi - \varphi') \tag{3.103}$$

$$\hat{\theta}' \cdot \hat{\varphi} = \cos(\theta') \sin(\varphi' - \varphi) \tag{3.104}$$

$$\hat{\varphi} \cdot \hat{\varphi}' = \cos(\varphi' - \varphi) \tag{3.105}$$

$$\hat{\theta}' \cdot \hat{\mathbf{r}} = \sin(\theta) \cos(\theta') \cos(\varphi - \varphi') - \cos(\theta) \sin(\theta') \tag{3.106}$$

$$\hat{\theta} \cdot \hat{\mathbf{r}}' = \cos(\theta) \sin(\theta') \cos(\varphi - \varphi') - \sin(\theta) \cos(\theta') \tag{3.107}$$

$$\hat{\theta} \cdot \hat{\theta}' = \cos(\theta) \cos(\theta') \cos(\varphi - \varphi') + \sin(\theta) \sin(\theta') \tag{3.108}$$

$$\hat{\mathbf{r}} \cdot \hat{\mathbf{r}}' = \sin(\theta) \sin(\theta') \cos(\varphi - \varphi') + \cos(\theta) \cos(\theta') \tag{3.109}$$

$$\hat{\mathbf{R}} \cdot \hat{\varphi}' = \frac{\mathbf{r} - \mathbf{r}'}{R} \cdot \hat{\varphi}' = \frac{r [\sin(\theta) \sin(\varphi - \varphi')]}{R} \tag{3.110}$$



$$\hat{\mathbf{R}}.\hat{\varphi} = \frac{\mathbf{r} - \mathbf{r}'}{R}.\hat{\varphi} = \frac{r' [\sin(\theta') \sin(\varphi - \varphi')]}{R} \quad (3.111)$$

$$\hat{\mathbf{R}}.\hat{\theta} = \frac{\mathbf{r} - \mathbf{r}'}{R}.\hat{\theta} = \frac{-r' [\cos(\theta) \sin(\theta') \cos(\varphi - \varphi') - \sin(\theta) \cos(\theta')]}{R} \quad (3.112)$$

$$\hat{\mathbf{R}}.\hat{\mathbf{r}}' = \frac{\mathbf{r} - \mathbf{r}'}{R}.\hat{\mathbf{r}}' = \frac{r [\sin(\theta) \sin(\theta') \cos(\varphi - \varphi') + \cos(\theta) \cos(\theta')] - r'}{R} \quad (3.113)$$

$$\hat{\mathbf{R}}.\hat{\mathbf{r}} = \frac{\mathbf{r} - \mathbf{r}'}{R}.\hat{\mathbf{r}} = \frac{r - r' [\sin(\theta) \sin(\theta') \cos(\varphi - \varphi') + \cos(\theta) \cos(\theta')]}{R} \quad (3.114)$$

$$\hat{\mathbf{R}}.\hat{\theta}' = \frac{\mathbf{r} - \mathbf{r}'}{R}.\hat{\theta}' = \frac{r [\sin(\theta) \cos(\theta') \cos(\varphi - \varphi') - \cos(\theta) \sin(\theta')]}{R} \quad (3.115)$$

$$\hat{\theta}.\underline{\mathbf{G}}_{ee}(\mathbf{r}, \mathbf{r}') . \hat{\mathbf{r}}' = \quad (3.116)$$

$$g(\mathbf{r}, \mathbf{r}') \left\{ \left( 3 \left( \hat{\mathbf{R}}.\hat{\theta} \right) \left( \hat{\mathbf{R}}.\hat{\mathbf{r}}' \right) - \hat{\theta}.\hat{\mathbf{r}}' \right) \left( \frac{1}{k^2 R^2} - \frac{1}{jkR} \right) - \left( 3 \left( \hat{\mathbf{R}}.\hat{\theta} \right) \left( \hat{\mathbf{R}}.\hat{\mathbf{r}}' \right) - \hat{\theta}.\hat{\mathbf{r}}' \right) \right\} \\ \hat{\theta}.\underline{\mathbf{G}}_{ee}(\mathbf{r}, \mathbf{r}') . \hat{\theta}' = \quad (3.117)$$

$$g(\mathbf{r}, \mathbf{r}') \left\{ \left( 3 \left( \hat{\mathbf{R}}.\hat{\theta} \right) \left( \hat{\mathbf{R}}.\hat{\theta}' \right) - \hat{\theta}.\hat{\theta}' \right) \left( \frac{1}{k^2 R^2} - \frac{1}{jkR} \right) - \left( \left( \hat{\mathbf{R}}.\hat{\theta} \right) \left( \hat{\mathbf{R}}.\hat{\theta}' \right) - \hat{\theta}.\hat{\theta}' \right) \right\} \\ \hat{\theta}.\underline{\mathbf{G}}_{ee}(\mathbf{r}, \mathbf{r}') . \hat{\varphi}' = \quad (3.118)$$

$$g(\mathbf{r}, \mathbf{r}') \left\{ \left( 3 \left( \hat{\mathbf{R}}.\hat{\theta} \right) \left( \hat{\mathbf{R}}.\hat{\varphi}' \right) - \hat{\theta}.\hat{\varphi}' \right) \left( \frac{1}{k^2 R^2} - \frac{1}{jkR} \right) - \left( \left( \hat{\mathbf{R}}.\hat{\theta} \right) \left( \hat{\mathbf{R}}.\hat{\varphi}' \right) - \hat{\theta}.\hat{\varphi}' \right) \right\}$$

### Scattered field

$$\mathbf{E} = -j\omega\mu \left( \int \underline{\mathbf{G}}_{ee}(\mathbf{r}, \mathbf{r}') . \mathbf{J}_{eq}(\mathbf{r}') dV' - \frac{\underline{\mathbf{L}}.\mathbf{J}_{eq}(\mathbf{r})}{k^2} \right) = \quad (3.119)$$

$$-j\omega\mu \left( \int g(\mathbf{r}, \mathbf{r}') \left\{ \left( 3\hat{\mathbf{R}}\hat{\mathbf{R}} - \underline{\mathbf{I}} \right) \left( \frac{1}{k^2 R^2} - \frac{1}{jkR} \right) - \left( \hat{\mathbf{R}}\hat{\mathbf{R}} - \underline{\mathbf{I}} \right) \right\} . \mathbf{J}_{eq}(\mathbf{r}') dV' - \frac{\underline{\mathbf{L}}.\mathbf{J}_{eq}(\mathbf{r})}{k^2} \right)$$

$$E_{\theta}^{sca} = -j\omega\mu \int \{ M\mathbf{J}_{eq}^r(\mathbf{r}') + N\mathbf{J}_{eq}^{\theta}(\mathbf{r}') + P\mathbf{J}_{eq}^{\varphi}(\mathbf{r}') \} dV' \quad (3.120)$$

$$E_r^{sca} = -j\omega\mu \int \{ Q\mathbf{J}_{eq}^r(\mathbf{r}') + R\mathbf{J}_{eq}^{\theta}(\mathbf{r}') + S\mathbf{J}_{eq}^{\varphi}(\mathbf{r}') \} dV' \quad (3.121)$$

## Chapter 4

### **A novel antenna structure using epsilon near zero material and total internal reflection principle [4]**

In this chapter, a novel geometry is proposed to achieve sum and difference patterns using a monopole antenna as the feed. This geometry consists of a dielectric flare with an embedded uniaxial wire medium acting as an epsilon near zero (ENZ) material. Beams are formed via total internal reflection, but by placing two metallic plates on two side walls of the flare, sum and difference patterns can be interchanged. Physics of the structure are discussed and its radiation pattern, gain and input impedance are calculated by full wave simulation. The antenna is chosen to operate at x band and can be easily fabricated.

#### **4.1 Introduction**

One of the important applications of metamaterials is beam forming using epsilon-near-zero (ENZ) materials. In such materials the phase velocity of the wave tends to infinity. As a result, if a radiator is placed inside an ENZ material, the waves emerging from different points of the ENZ boundary are in phase. That is, the radiation from a source inside an ENZ object conforms in a simple way to the shape of the exterior of the ENZ object. Also, considering Snells law, the critical angle for total internal reflection from an ENZ surface is zero, indicating that a wave can only transmit through an ENZ surface normally. This fact is used in [40] to shape the patterns of an antenna inside an ENZ material. As a more similar structure to our work, in [41] the pattern of a monopole antenna is shaped by immersing it into a uniaxial wire medium acting as an artificial plasma. The plasma frequency of the wire medium is adjusted to be at the operating frequency of the antenna,

hence providing zero permittivity around it. In our geometry, we also use a monopole as the radiating antenna and a uniaxial wire medium as the ENZ material because of its simple fabrication.

The final generated pattern which is achieved by our geometry is either a difference or a sum pattern as are used in monopulse radar systems. In a tracking system the difference pattern of a movable antenna is used to lock the target in the null of the pattern while in a surveillance system the location of a target is extracted from the amplitude or phase of two overlapping patterns [42]. In other words, in a tracking system the antenna positioner is moved until the signal in this difference channel reaches a minimum, causing the sum channel to point accurately at the radar target. There are different well known patterns for sum and difference patterns such as Taylor distributions and Bayliss distributions which use phased arrays with usually complex feed networks. In this work, we do not achieve patterns as good as aforementioned patterns. However, we are not using any feed network and the antenna has a single input. This makes the antenna suitable for tracking systems but unsuitable for monopulse radar systems in which the access to the two beams are required separately.

## 4.2 The antenna geometry and results

Total internal reflection occurs when a wave is obliquely-incident on a dielectric interface with an angle greater than the critical angle. From electromagnetic boundary conditions, it is evident that for the case of a TM incident wave (as shown in Fig. 4.1), under conditions of total internal reflection the polarity of the reflected field is as shown in Fig. 4.1(a) (the PEC case is shown in Fig. 4.1(b)).

Figure 4.2 shows half of the proposed structure. It consists of a rectangular ENZ volume with its upper and lower faces covered by PEC. A monopole antenna is placed in the middle of the lower GND plane so that it can be easily fed by a coaxial cable. A dielectric flare shaped material with a  $45^\circ$  angle surrounds the structure. To generate a

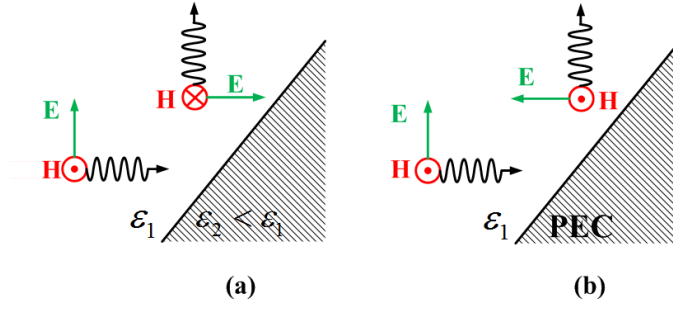


Figure 4.1: TM wave incident on a (a) dielectric and (b) PEC material at a  $45^\circ$  angle.

difference pattern, all of the side edges of the flare are left open; to generate a sum pattern two adjacent side edges are covered by PEC sheets. We labeled these side edges as #1 and #2 in Fig. 4.2. Since the monopole is in the  $z$  direction, from the fact that epsilon is almost zero, Ampere's law simplifies to

$$\nabla \times \mathbf{H} = \mathbf{J} \quad (4.1)$$

which implies that  $H_z = 0$  everywhere inside the ENZ region assuming a sufficiently long wire. Knowing this and the fact that a wave can only radiate normally from the ENZ boundary, one can conclude that the electric field is in the  $z$  direction. Therefore, the rectangular ENZ region shapes the wavefront as four plane waves traveling in the  $\pm x$  and  $\pm y$  directions which are incident on the flare boundary as a TM wave with  $45^\circ$  incidence angle (as in Fig. 4.1). If the permittivity of the dielectric flare is greater than two, the critical angle of the flare boundary is less than  $45^\circ$ . As a result, total internal reflection occurs for the four plane waves incident on the flare boundary and they all reflect in the  $z$  direction.

Depending on whether edges #1 and #2 are covered with PEC or not, the electric field distribution on the radiating edge is as Fig. 4.3(a) or 4.3(b). Therefore, there are four radiating spots on the radiating edge (top surface) as shown in Fig. 4.3. The electric field direction and the distance between these spots specifies the radiation properties of the antenna. The field distribution of Fig. 4.3(a) produces a four lobe pattern with a

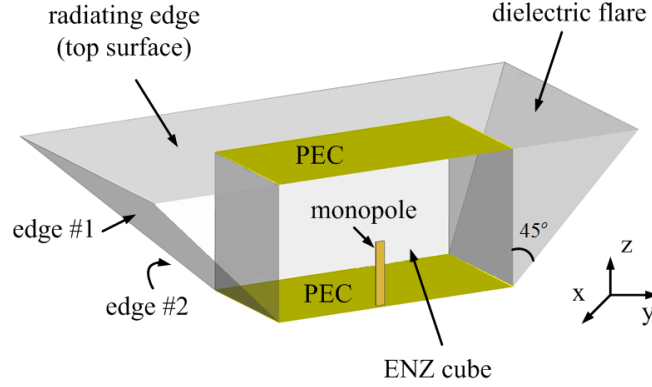


Figure 4.2: Half of the proposed geometry. Full geometry will be obtained by adding a mirror image in the x-z plane.

null at  $\theta = 0$  as shown in Fig. 4.4. As we increase the size of the ENZ material, the distance between radiating apertures increases and therefore the null becomes sharper. Equivalently, gain increases and the four lobes become closer to each other. The field distribution of Fig. 4.3(b) produces a pencil beam at an angle very close to  $\theta = 0$  as shown in Fig. 4.5 which can be considered as a sum pattern. The more we increase the aperture distances, the more the beam angle becomes closer to  $\theta = 0$ .

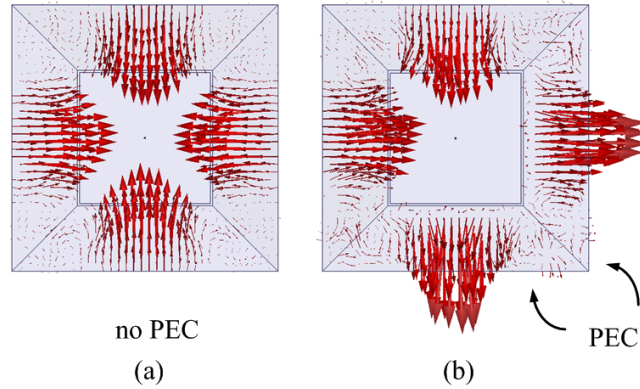


Figure 4.3: Full wave simulated electric field distribution on the radiating edge.

Figures 4.3, 4.4 and 4.5 are obtained using full wave simulation [43] for a structure with the following flare size: the bottom rectangle is 8 by 8 cm, the upper rectangle is 16 by 16 cm and the angle is 45 degrees. Plaster is used as the dielectric material of the flare around the ENZ material with permittivity of 3.84. The monopole antenna length

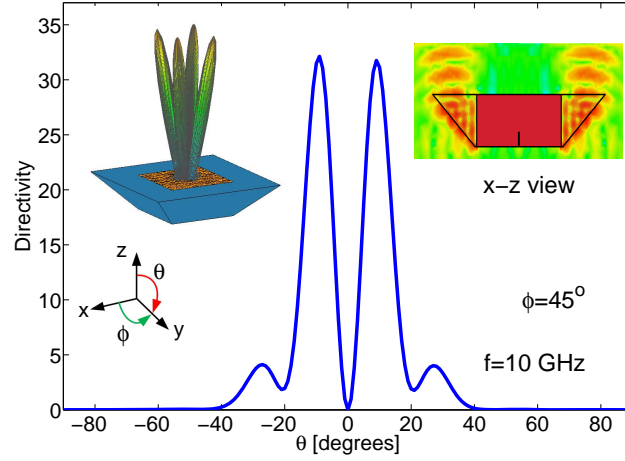


Figure 4.4: Full wave simulated directivity and field distribution of the difference pattern.

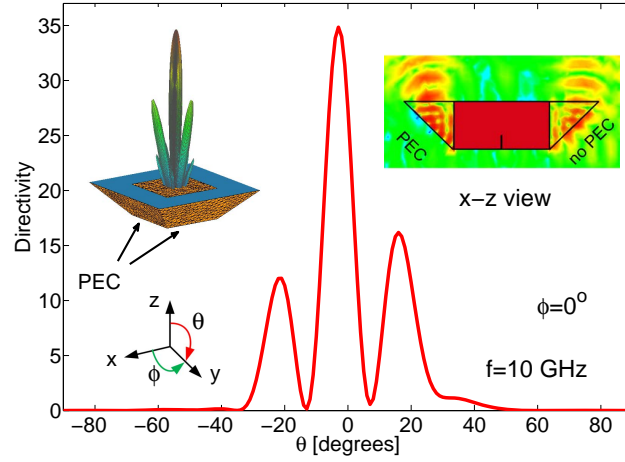


Figure 4.5: Full wave simulated directivity and field distribution of the sum pattern.

is 7.5 mm and the frequency is 10 GHz. The ENZ region in Figs. 4.3, 4.4 and 4.5 is an idealized dielectric with permittivity of zero. The input impedance of the sum pattern is 11.6-43.5j ohms and the input impedance for the difference pattern is 52-33j ohms. All the simulations are done using a wire monopole with no thickness. We may change the imaginary part of the impedance by adjusting the thickness of the monopole. The ENZ region can be realized by a uniaxial wire medium with air as its host medium. The wire's diameter, length, and period are 1, 40, and 10 mm respectively which gives the plasma frequency as 9.2 GHz [26]. Figure 4.6 shows the antenna with the uniaxial wire medium

as its ENZ material. Full wave simulation results of Fig. 4.6 are shown in Figs. 4.7 and 4.8.

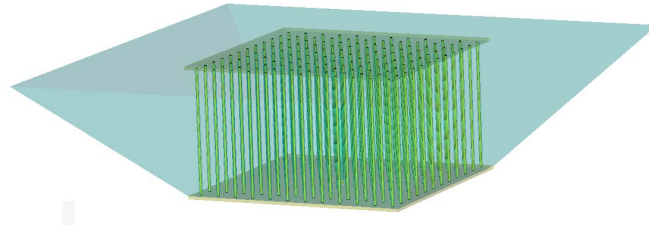


Figure 4.6: The antenna geometry using uniaxial wire medium as its ENZ material.

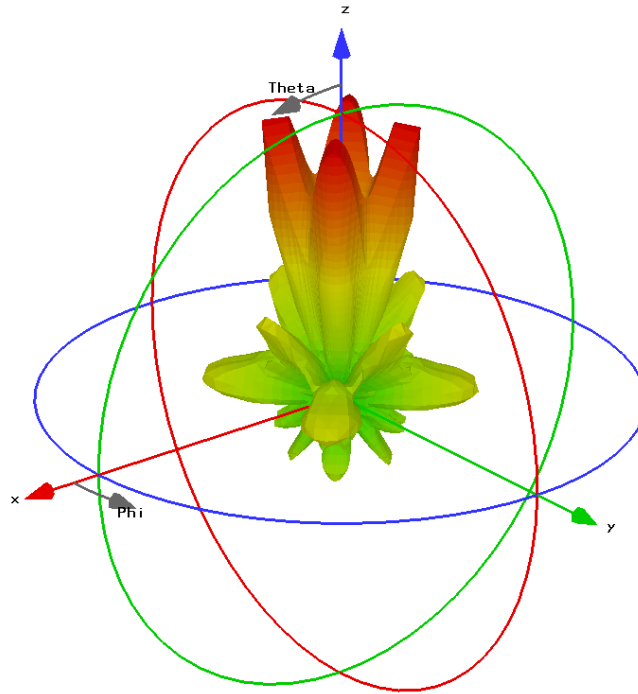


Figure 4.7: The difference pattern (directivity) of the antenna with uniaxial wire medium.

### 4.3 Summary

Sum and difference patterns were generated using a simple and novel structure and its radiation pattern, input impedance and directivity were investigated using full-wave simulations. The structure is useful for radar applications and tracking systems.

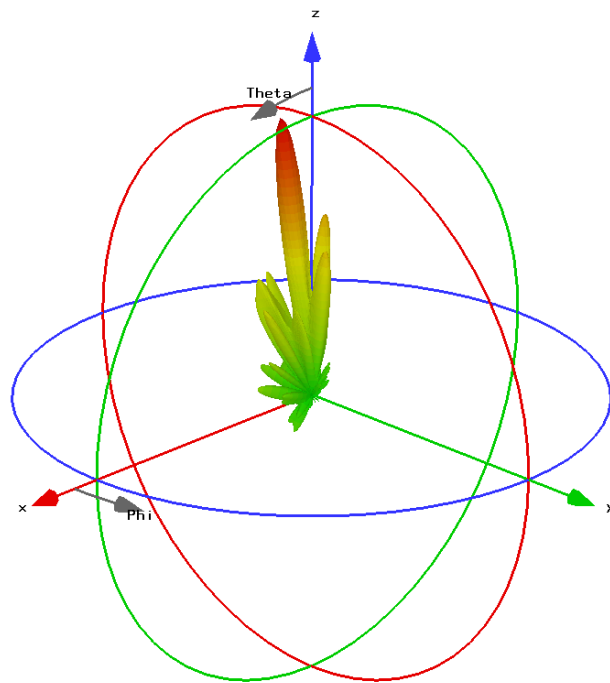


Figure 4.8: The sum pattern (directivity) of the antenna with uniaxial wire medium.



## Chapter 5

### On the possibility of ENZ realization using spatially dispersive material [5]

In this section, the momentum-dependent permittivity for a broad class of natural materials and wire-mesh metamaterials with spatial dispersion is determined in real-space, and a new characteristic length parameter is defined, in addition to the Debye length, which governs polarization screening. It is found that in the presence of spatial dispersion the electric displacement does not vanish at the plasma frequency, in general. However, conditions are investigated under which the permittivity can vanish or be strongly diminished, even in the presence of spatial dispersion, implementing an epsilon-near-zero material.

#### 5.1 introduction

Materials with effective permittivity of approximately zero, also known as epsilon-near-zero (ENZ) materials [44], have become an important topic of research with a variety of applications. For example, enhancing the radiation directivity of antennas [45], supercoupling [46; 17], transforming curved wavefronts into planar ones [47], implementing optical nano circuit concepts [48], cloaking [49; 50], designing lenses with enhanced focusing [51; 52], and tailoring the radiation pattern of antennas [53] are recent applications of ENZ materials. However, to our knowledge, in previous work on ENZ applications spatial dispersion of the material was ignored in establishing the ENZ condition, which, for local materials, occurs exactly at the plasma frequency. This is often a reasonable approximation for natural materials where spatial dispersion is fairly weak (e.g. typical semiconductors, metals, or high-density plasmas). However, this may not be a good

approximation for artificial materials with strong spatial dispersion, such as wire media [27; 26].

The present work has three aims: 1) to provide the “space-domain” form of the permittivity  $\underline{\underline{\varepsilon}}(\mathbf{r} - \mathbf{r}')$  appropriate for forming the space-domain relation between displacement and electric field,  $\mathbf{D}(\mathbf{r}) = \int \underline{\underline{\varepsilon}}(\mathbf{r} - \mathbf{r}') \cdot \mathbf{E}(\mathbf{r}') d^3\mathbf{r}'$ , 2) to introduce a new screening parameter  $k_\alpha$  that relates polarization to the total electric field, in a similar way that  $k_D$ , the Debye wavenumber, relates polarization to the incident electric field, and 3), to address under what conditions we can achieve an ENZ medium for which  $\mathbf{D} \simeq \mathbf{0}$  in the presence of spatial dispersion.

We consider the momentum-dependent permittivity tensor in the spatial-temporal Fourier transform domain as

$$\frac{\underline{\underline{\varepsilon}}(\mathbf{q})}{\varepsilon_0} = \varepsilon_h \underline{\underline{\mathbf{I}}} - \kappa \left( \underline{\underline{\mathbf{I}}} - \frac{1}{q^2 - \alpha^2} \mathbf{q}\mathbf{q} \right), \quad (5.1)$$

which describes a wide range of natural materials (NM) including many semiconductors, plasmas, and metals, as well as the isotropic connected wire medium (ICWM) as is shown in Fig. 5.1 which acts as an artificial plasma [26; 8; 1].

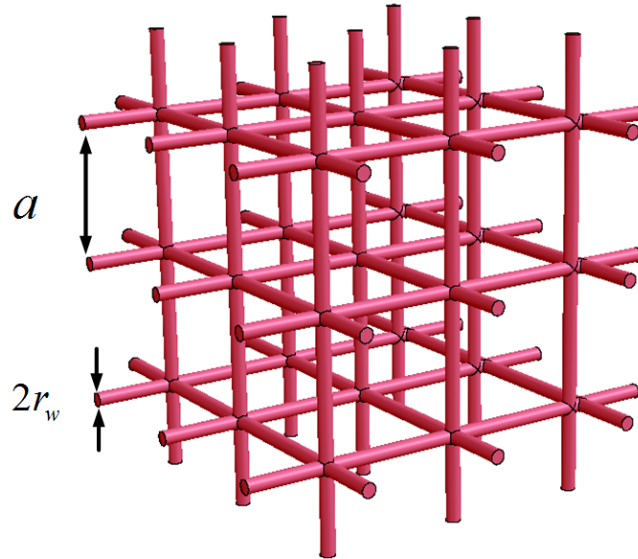


Figure 5.1: Isotropic connected wire medium with wire period ( $a$ ) and radius ( $r_w$ ).

In (5.1),  $\underline{\mathbf{I}}$  is the identity tensor,  $\varepsilon_h$  is the relative permittivity (for a wire medium this is the permittivity of the host medium),  $\varepsilon_0$  is the permittivity of vacuum,  $\mathbf{q}$  is the spatial Fourier transform wavenumber (time dependence is  $e^{j\omega t}$ )

$$\mathcal{F}\{f(\mathbf{r})\} = F(\mathbf{q}) = \int f(\mathbf{r}) e^{-j\mathbf{q}\cdot\mathbf{r}} d^3\mathbf{r}, \quad (5.2)$$

$$f(\mathbf{r}) = \frac{1}{(2\pi)^3} \int F(\mathbf{q}) e^{j\mathbf{q}\cdot\mathbf{r}} d^3\mathbf{q}, \quad (5.3)$$

with  $\mathbf{r}$  being the position vector, and

$$\kappa = \frac{j\sigma}{\omega\varepsilon_0}, \quad (5.4)$$

$$\alpha^2 = -\frac{j\omega}{D} \quad (5.5)$$

where  $\sigma$  is the conductivity [S/m],  $D$  is the diffusion coefficient [ $\text{m}^2/\text{s}$ ], and  $\omega$  is the radial frequency [1]. We assume all material losses are incorporated in the conductivity. For natural materials we assume conductivity in the usual Drude form,

$$\sigma^{\text{NM}} = \frac{\omega_p^2 \varepsilon_0}{(j\omega + \tau^{-1})}, \quad (5.6)$$

where  $\omega_p^2 = n_e q_e^2 / \varepsilon_0 m_e$  ( $\omega_p$  is the plasma frequency) and  $\tau$  is the relaxation time - typical values for semiconductors and metals are  $\tau \sim 10 - 100$  fs. In the low-loss case  $\omega \gg \tau^{-1}$ ,  $\sigma^{\text{NM}}$  is essentially imaginary-valued. For the isotropic wire medium the effective conductivity can be expressed in the same Drude form [1]

$$\sigma^{\text{ICWM}} = \frac{-j\omega\varepsilon_0}{\left(\frac{\omega^2}{\omega_p^2} - \frac{1}{\varepsilon_m - \varepsilon_h} \frac{1}{f_v}\right)} \simeq \frac{\omega_p^2 \varepsilon_0}{(j\omega + (\tau^{\text{WM}})^{-1})}, \quad (5.7)$$

upon defining  $\tau^{\text{WM}} \equiv f_v \sigma_m / \omega_p^2 \varepsilon_0$ , where  $\sigma_m$  is the assumed real-valued conductivity of

the wires (the permittivity of the wires is  $\varepsilon_m = 1 - j\sigma_m/\omega\varepsilon_0$ ),  $\omega_p$  is the plasma frequency  $(\omega_p a)^2 \cong 2\pi c^2 / \ln(a^2/4r_w/(a - r_w)) \cong 2\pi c^2 / (\ln(a/(2\pi r_w)) + 0.5275)$  where  $a$  and  $r_w$  are wire period and radius, respectively, and  $f_v$  is the volume fraction of wires,  $f_v = \pi r_w^2/a^2$ . Typical values of  $\tau^{\text{WM}}$  are on the order of  $\mu\text{s}$ , although  $(\tau^{\text{WM}})^{-1} \rightarrow 0$  for perfect electrical conducting (PEC) wires in a lossless host medium.

The diffusion coefficient in (5.5) is

$$D = \frac{\beta}{j\omega(1 - j(\omega\tau)^{-1})}. \quad (5.8)$$

For natural materials  $\beta^{\text{NM}} = \langle v^2 \rangle / 3$ , with  $\langle v^2 \rangle$  being the electron mean-square velocity[54]. For plasmas and semiconductors  $\langle v_{\text{thermal}}^2 \rangle = 3k_B T/m$ , but for good metals  $\langle v^2 \rangle = 3v_F^2/5$ , where  $v_F$  is the electron Fermi velocity. For isotropic wire media  $D^{\text{ICWM}} = c^2 \sigma^{\text{ICWM}} / l_0 \varepsilon_0 \varepsilon_h \omega_p^2$  [1], such that

$$\beta^{\text{WM}} = \frac{c^2}{l_0 \varepsilon_h} = \frac{v_h^2}{l_0} \quad (5.9)$$

where  $v_h = 1/\sqrt{\mu_0 \varepsilon_0 \varepsilon_h}$  is the electromagnetic phase velocity in the nondispersive host and  $l_0$  is a weak function of wire period with typical values of  $l_0 \sim 2 - 3$  [8]; note the similarity between  $\beta^{\text{WM}} = v_h^2/l_0 \simeq v_h^2/3$  and with  $\beta^{\text{NM}} = \langle v^2 \rangle / 3$ . For lossless natural materials or PEC wire materials with a non absorbing host,

$$\kappa = \frac{\omega_p^2}{\omega^2}, \quad \alpha^2 = \frac{\omega^2}{\beta}. \quad (5.10)$$

It is useful for the purpose of this paper to decompose (5.1) into longitudinal and transverse components with respect to  $\mathbf{q}$ ,

$$\frac{\underline{\varepsilon}(\mathbf{q})}{\varepsilon_0} = (\varepsilon_h - \kappa)(\mathbf{I} - \hat{\mathbf{q}}\hat{\mathbf{q}}) + \left( \varepsilon_h - \kappa + \frac{\kappa q^2}{q^2 - \alpha^2} \right) \hat{\mathbf{q}}\hat{\mathbf{q}}$$

$$= \varepsilon^T (\mathbf{I} - \hat{\mathbf{q}}\hat{\mathbf{q}}) + \varepsilon^L(q) \hat{\mathbf{q}}\hat{\mathbf{q}}. \quad (5.11)$$

Notice that for natural materials  $\varepsilon_h - \kappa = \varepsilon_h - j\sigma/\omega\epsilon_0$  is merely the complex permittivity, and in the lossless case  $\varepsilon_h - \kappa$  is real-valued. For lossless wire media  $\sigma$  is imaginary and nonzero, so that  $\varepsilon_h - \kappa$  is also real-valued.

It is evident from (5.1) that in the local limit ( $q \rightarrow 0$ ) and assuming lossless natural materials or wire media with perfectly conducting wires ( $\varepsilon_m \rightarrow -\infty$ ), the space-domain permittivity will be

$$\frac{\underline{\underline{\varepsilon}}}{\varepsilon_0} = \varepsilon_h \left( 1 - \frac{\omega_p^2}{\varepsilon_h \omega^2} \right) \mathbf{I} \quad (5.12)$$

which is the equation commonly used in the design of ENZ materials. The permittivity (5.12) becomes exactly zero at the frequency  $\omega = \omega_p/\sqrt{\varepsilon_h}$ .

In the following, we find the inverse Fourier transform of (5.1), and the polarization (and therefore the electric displacement field) in terms of the scattered, incident, and total fields inside the material. From the polarization in the space domain we will see that the Debye length is not the best parameter for considering the ENZ condition. A new wavenumber leading to a different characteristic screening length will be introduced to study the electric displacement inside a spatially dispersive material, and conditions will be investigated under which the electric displacement can vanish.

## 5.2 Permittivity tensor and polarization vector in space domain

### 5.2.1 Permittivity tensor

The inverse Fourier transform of (5.1) is easily seen to be

$$\frac{\underline{\varepsilon}(\mathbf{r})}{\epsilon_0} = (\varepsilon_h - \kappa) \delta(\mathbf{r}) \underline{\mathbf{I}} - \kappa \nabla \nabla \frac{e^{-j\alpha r}}{4\pi r} \quad (5.13)$$

where  $\delta(\mathbf{r})$  is the Dirac delta function and we have used the Fourier transform identities

$$\mathcal{F} \left\{ \frac{e^{-j\alpha r}}{4\pi r} \right\} = \frac{1}{q^2 - \alpha^2}, \quad (5.14)$$

$$\mathcal{F} \{ \nabla \nabla g(\mathbf{r}) \} = -\mathbf{q} \mathbf{q} \mathcal{F} \{ g(\mathbf{r}) \}. \quad (5.15)$$

The derivatives are easily carried out to yield

$$\frac{\underline{\varepsilon}(\mathbf{r})}{\epsilon_0} = (\varepsilon_h - \kappa) \delta(\mathbf{r}) \underline{\mathbf{I}} - \kappa \left\{ (3\hat{\mathbf{r}}\hat{\mathbf{r}} - \underline{\mathbf{I}}) \left( \frac{1}{r^2} - \frac{\alpha}{ir} \right) - \alpha^2 \hat{\mathbf{r}}\hat{\mathbf{r}} \right\} \frac{e^{-j\alpha r}}{4\pi r}. \quad (5.16)$$

Equation (5.16) is the permittivity tensor in the “space domain” (it is not actually in real space because of the delta function - it is a quantity to be integrated) which relates the electric displacement vector  $\mathbf{D}(\mathbf{r})$  and the electric field vector  $\mathbf{E}(\mathbf{r})$  as  $\mathbf{D}(\mathbf{r}) = \underline{\varepsilon}(\mathbf{r}) * \mathbf{E}(\mathbf{r})$ , where  $*$  denotes convolution,

$$\mathbf{D}(\mathbf{r}) = \int \underline{\varepsilon}(\mathbf{r} - \mathbf{r}') \bullet \mathbf{E}(\mathbf{r}') d^3\mathbf{r}'. \quad (5.17)$$

We have assumed that the relation between  $\mathbf{D}(\mathbf{q})$  and  $\mathbf{E}(\mathbf{q})$  in the spatial transform domain is  $\mathbf{D}(\mathbf{q}) = \underline{\varepsilon}(\mathbf{q}) \bullet \mathbf{E}(\mathbf{q})$ .

### 5.2.2 Polarization as a function of the total field

In the following it is useful to introduce the screening wavenumber  $k_\alpha \equiv j\alpha = -\sqrt{j\omega/D}$ .

Using (5.1) in the definition of the polarization,

$$\mathbf{P}(\mathbf{q}) = \mathbf{D}(\mathbf{q}) - \varepsilon_0 \mathbf{E}(\mathbf{q}) = (\underline{\varepsilon}(\mathbf{q}) - \varepsilon_0 \underline{\mathbf{I}}) \bullet \mathbf{E}(\mathbf{q}) \quad (5.18)$$

$$= \varepsilon_0 \left( (\varepsilon_h - 1 - \kappa) \mathbf{I} + \kappa \frac{\mathbf{q}\mathbf{q}}{(q^2 + k_\alpha^2)} \right) \cdot \mathbf{E}(\mathbf{q})$$

where  $\mathbf{E}$  is the total electric field inside the material. Decomposing (5.18) into parallel and perpendicular components with respect to  $\mathbf{q}$ ,

$$\frac{\mathbf{P}_\parallel(\mathbf{q})}{\varepsilon_0} = (\varepsilon_h - 1 - \kappa) \mathbf{E}_\parallel(\mathbf{q}) + \kappa \frac{q^2 \mathbf{E}_\parallel(\mathbf{q})}{(q^2 + k_\alpha^2)}, \quad (5.19)$$

$$\frac{\mathbf{P}_\perp(\mathbf{q})}{\varepsilon_0} = (\varepsilon_h - 1 - \kappa) \mathbf{E}_\perp(\mathbf{q}) \quad (5.20)$$

in the transform domain, and

$$\frac{\mathbf{P}_\parallel(\mathbf{r})}{\varepsilon_0} = (\varepsilon_h - 1 - \kappa) \mathbf{E}_\parallel(\mathbf{r}) - \kappa \left( \nabla^2 \mathbf{E}_\parallel(\mathbf{r}) * \frac{e^{-k_\alpha r}}{4\pi r} \right), \quad (5.21)$$

$$\frac{\mathbf{P}_\perp(\mathbf{r})}{\varepsilon_0} = (\varepsilon_h - 1 - \kappa) \mathbf{E}_\perp(\mathbf{r}) \quad (5.22)$$

in the space domain. These show that the longitudinal polarization has a term that is local with the total longitudinal field, as well as a nonlocal contribution that decays according to the screening length  $L_\alpha = 2\pi/k_\alpha$  (or, for large screening length the nonlocal contribution decays algebraically). In the absence of spatial dispersion ( $D = 0$ ),  $L_\alpha \rightarrow 0$  and the relation between longitudinal polarization and total longitudinal field is local, as is the relation between perpendicular polarization and total perpendicular field.

### 5.2.3 Polarization as a function of the scattered field

We assume a translationally-invariant material, although a finite-volume material scatterer can be accommodated in the same manner using the volume equivalence principle. An incident field  $\mathbf{E}^i(\mathbf{r})$  polarizes the medium, creating polarization current,  $j\omega\mathbf{P}(\mathbf{r})$ , such

that the scattered field  $\mathbf{E}^{\text{sca}}(\mathbf{r})$  produced by the induced polarization is

$$\mathbf{E}^{\text{sca}}(\mathbf{r}) = -j\omega\mu_0 (\underline{\mathbf{G}}(\mathbf{r}) * j\omega\mathbf{P}(\mathbf{r})) \quad (5.23)$$

where  $\underline{\mathbf{G}}(\mathbf{r})$  is the electric dyadic Green's function [32]. Taking the Fourier transform of (5.23) and using the transform-domain Green's function ,

$$\mathbf{E}^{\text{sca}}(\mathbf{r}) = \frac{k^2}{\varepsilon_0} \frac{\underline{\mathbf{I}}k^2 - \mathbf{q}\mathbf{q}}{k^2(q^2 - k^2)} \cdot \mathbf{P}(\mathbf{q}) = \frac{k^2\mathbf{P}(\mathbf{q})}{\varepsilon_0(q^2 - k^2)} - \frac{q^2\mathbf{P}_{\parallel}(\mathbf{q})\hat{\mathbf{q}}}{\varepsilon_0(q^2 - k^2)}. \quad (5.24)$$

Therefore,

$$\mathbf{P}_{\parallel}(\mathbf{q}) = -\varepsilon_0 \mathbf{E}_{\parallel}^{\text{sca}}(\mathbf{q}), \quad (5.25)$$

$$\mathbf{P}_{\perp}(\mathbf{q}) = \frac{\varepsilon_0}{k^2} (q^2 - k^2) \mathbf{E}_{\perp}^{\text{sca}}(\mathbf{q}). \quad (5.26)$$

In the space domain, (5.25) and (5.26) become

$$\mathbf{P}_{\parallel}(\mathbf{r}) = -\varepsilon_0 \mathbf{E}_{\parallel}^{\text{sca}}(\mathbf{r}) \quad (5.27)$$

$$\mathbf{P}_{\perp}(\mathbf{r}) = -\varepsilon_0 \left(1 + \frac{\nabla^2}{k^2}\right) \mathbf{E}_{\perp}^{\text{sca}}(\mathbf{r}). \quad (5.28)$$

Therefor, the longitudinal polarization is local to the longitudinal scattered field, although the transverse polarization is nonlocal to the transverse scattered field.

## 5.2.4 Polarization as a function of the incident field

By decomposing the total electric field into the scattered and incident fields as  $\mathbf{E}(\mathbf{r}) = \mathbf{E}^i(\mathbf{r}) + \mathbf{E}^{\text{sca}}(\mathbf{r})$  and using (5.19)-(5.20) and (5.25)-(5.26),



$$\mathbf{P}_{\parallel}(\mathbf{q}) = \frac{\varepsilon_0}{\varepsilon_h} \left( \varepsilon_h - 1 + \frac{\kappa}{\kappa - \varepsilon_h} \frac{k_D^2}{q^2 + k_D^2} \right) \mathbf{E}_{\parallel}^i(\mathbf{q}), \quad (5.29)$$

$$\mathbf{P}_{\perp}(\mathbf{q}) = \varepsilon_0 (\varepsilon_h - 1 - \kappa) \left( 1 + \frac{(\varepsilon_h - \kappa - 1) k^2}{q^2 - (\varepsilon_h - \kappa) k^2} \right) \mathbf{E}_{\perp}^i(\mathbf{q}) \quad (5.30)$$

in the transform domain, where

$$k_D = \alpha \sqrt{\frac{\kappa}{\varepsilon_h} - 1} = \sqrt{\frac{j\omega\varepsilon_0\varepsilon_h + \sigma}{D\varepsilon_0\varepsilon_h}} \quad (5.31)$$

is the Debye wavenumber (usually defined for  $\omega = 0$ ). In the space domain,

$$\mathbf{P}_{\parallel}(\mathbf{r}) = \frac{\varepsilon_0}{\varepsilon_h} \left( (\varepsilon_h - 1) \mathbf{E}_{\parallel}^i(\mathbf{r}) + \frac{k_D^2 \kappa}{\kappa - \varepsilon_h} \mathbf{E}_{\parallel}^i(\mathbf{r}) * \frac{e^{-k_D r}}{4\pi r} \right), \quad (5.32)$$

$$\mathbf{P}_{\perp}(\mathbf{r}) = \varepsilon_0 (\varepsilon_h - 1 - \kappa) \mathbf{E}_{\perp}^i(\mathbf{r}) \quad (5.33)$$

$$+ \varepsilon_0 (\varepsilon_h - \kappa - 1)^2 k^2 \left( \mathbf{E}_{\perp}^i(\mathbf{r}) * \frac{e^{-jk\sqrt{\varepsilon_h - \kappa}r}}{4\pi r} \right).$$

These show that the longitudinal polarization has a term that is local with the incident field, as well as a nonlocal contribution that decays according to the Debye length  $L_D = 2\pi/k_D$ . In the absence of spatial dispersion ( $D = 0$ ),  $L_D \rightarrow 0$  and the relation between longitudinal polarization and the longitudinal incident field is local.

The Debye wavenumber and the new screening wavenumber are related as

$$k_D = k_{\alpha} \sqrt{1 - \frac{\kappa}{\varepsilon_h}}.$$

Assuming for simplicity that  $\varepsilon_h = 1$  and that the materials are lossless, from  $\kappa = \omega_p^2/\omega^2$  we have that for  $\omega > \omega_p$ ,  $\kappa < 1$  and so  $k_D < k_{\alpha}$ , with  $k_D \rightarrow k_{\alpha}$  as  $\omega \rightarrow \infty$ . However, in this case both wavenumbers are imaginary-valued and no screening takes place. The

material response is generally nonlocal, with a relatively large effective radius (nonlocal effects diminish algebraically with distance  $\mathbf{r} - \mathbf{r}'$ ). For  $\omega < \omega_p$ ,  $\kappa > 1$  and although  $k_\alpha$  is imaginary  $k_D$  is real-valued, resulting in screening of the incident field. Thus, in the lossless case we have the usual condition that below the plasma frequency the effect of the incident field is (exponentially) screened by the Debye length, whereas above the plasma frequency no such screening takes place. Regardless of frequency the polarization is not screened in terms of the total field (which is important in considering the displacement field), but the response is generally nonlocal, with the relationship between polarization and total field decaying algebraically with distance  $\mathbf{r} - \mathbf{r}'$ . In the case of lossy media,  $k_D$  and  $k_\alpha$  are both complex-valued, and screening of polarization in terms of both the incident field (via  $k_D$ ) and in terms of the total field (via  $k_\alpha$ ) take place.

### 5.3 Discussion of the results and the establishment of the ENZ condition

In the presence of spatial dispersion the ENZ condition is  $\mathbf{D}(\mathbf{r}) \simeq 0$ . From (3.10) and (3.11),

$$\mathbf{D}_\parallel(\mathbf{r}) = \varepsilon_0 (\varepsilon_h - \kappa) \mathbf{E}_\parallel(\mathbf{r}) - \varepsilon_0 \kappa \nabla^2 \mathbf{E}_\parallel(\mathbf{r}) * \frac{e^{-k_\alpha r}}{4\pi r}, \quad (5.34)$$

$$\mathbf{D}_\perp(\mathbf{r}) = \varepsilon_0 (\varepsilon_h - \kappa) \mathbf{E}_\perp(\mathbf{r}). \quad (5.35)$$

Now, we can consider three different scenarios:

1. the electric field is transverse (i.e., perpendicular to  $\mathbf{q}$ ): in this case we only need consider (5.35), and the ENZ condition can be satisfied simply by setting  $\varepsilon_h = \kappa$ , which is equivalent to  $\varepsilon^T = 0$ , which is the usual ENZ condition for a local material. As an example, if the electric field is associated with a TE traveling wave, the

permittivity becomes exactly zero (or equivalently,  $\mathbf{D} = \mathbf{0}$ ) at the plasma frequency.

2. the electric field is longitudinal (i.e., parallel to  $\mathbf{q}$ ): in this case we only need consider (5.34), and the ENZ condition is still possible by setting (5.34) to be zero, leading to

$$\varepsilon^L(\mathbf{r}) * \mathbf{E}(\mathbf{r}) = 0 \quad (5.36)$$

where

$$\varepsilon^L(\mathbf{r}) = (\varepsilon_h - \kappa) \delta(\mathbf{r}) - \kappa \nabla^2 \left( \frac{e^{-k_\alpha r}}{4\pi r} \right). \quad (5.37)$$

Unlike  $\varepsilon^T$ , the longitudinal permittivity  $\varepsilon^L$  must be convolved with the electric field, and (5.36) does not simply lead to  $\varepsilon^L = 0$ ; the condition depends on  $\mathbf{E}(\mathbf{r})$  in general. As an example, for a purely longitudinal field having the form  $\mathbf{E}(\mathbf{r}) = e^{-j\mathbf{k} \cdot \mathbf{r}} \hat{\mathbf{k}}$ , then

$$\mathbf{D}(\mathbf{r}) = \varepsilon_0 \mathbf{E}(\mathbf{r}) \left( \varepsilon_h + \frac{\kappa \alpha^2}{k^2 - \alpha^2} \right), \quad (5.38)$$

for which the ENZ condition is  $\varepsilon_h = \kappa (1 - k^2/\alpha^2)^{-1}$ . In the absence of spatial dispersion ( $D = 0$ ),  $\alpha^2 \rightarrow \infty$  and, as expected, the ENZ condition for longitudinal fields becomes the same as for transverse fields,

$$\varepsilon_h = \kappa. \quad (5.39)$$

For lossless wire media (5.39) becomes

$$\omega = \frac{\omega_p}{\sqrt{\varepsilon_h \left( 1 - \frac{1}{l_0} \right)}} \quad (5.40)$$

so that the effective plasma frequency is larger in the event of spatial dispersion than if spatial dispersion were absent (spatial dispersion can be set to zero by setting  $l_0 = 0$  which leads to  $D = 0$  and  $\omega = \omega_p/\sqrt{\varepsilon_h}$ ). It should be noted that a purely longitudinal field generally does not exist (an exception is a local material exactly

at the plasma frequency), but here we consider this case since the next scenario is a combination of the first two cases.

3. the electric field is neither purely transverse nor purely longitudinal (i.e., neither parallel nor perpendicular to  $\mathbf{q}$ ): in this case, the ENZ condition can be obtained only if

$$\varepsilon^T = 0, \quad (5.41)$$

and (5.36) simultaneously, which leads to, from (5.34)-(5.35),

$$\nabla^2 \mathbf{E}_{\parallel}(\mathbf{r}) * \frac{e^{-k_{\alpha} r}}{4\pi r} = 0. \quad (5.42)$$

Equation (5.42) cannot be satisfied in general, and it depends on the electric field. However, if  $k_{\alpha}$  has a large real part, (5.42) can be approximately satisfied independent of the electric field due to strong screening.

In summary, if we have a purely transverse field (such as a TE wave), the ENZ condition is satisfied as occurs for local materials. For purely longitudinal fields the ENZ condition can also be obtained, (5.39), although at a different frequency from the local case. And, for the general case the ENZ condition cannot be exactly obtained, although if sufficient field screening occurs via  $k_{\alpha}$  the ENZ condition can be approximately satisfied.

Given the last statement, it is useful to consider the screening parameter  $k_{\alpha}$ , or, more precisely, the screening length  $L_{\alpha} = 2\pi / \text{Re}(k_{\alpha})$ . This screening length is different from the Debye length in the sense that it refers to screening of the total field rather than the incident field (see the appendix). Since the relation between displacement field and electric field involves the total fields, this screening length is relevant for the displacement field and consideration of the ENZ condition. Table 5.1 shows the two screening lengths for some natural and artificial materials: gold at two frequencies, a semiconductor at two frequencies and for two doping levels, and an isotropic wire medium, where the Debye screening length is defined in the appendix. For the wire medium examples,  $L_{\alpha}$  is quite

Table 5.1: Normalized characteristic screening and Debye length of some sample materials

Material	$\omega/\omega_p$	$L_D/\lambda_0$	$L_\alpha/\lambda_0$
gold	0.8	$2.78 \times 10^{-3}$	1.79
gold	1.2	2.69	1.48
SC ( $N = 10^{20}m^{-3}$ )	0.8	$8.35 \times 10^{-5}$	$8.36 \times 10^{-5}$
SC ( $N = 10^{20}m^{-3}$ )	1.2	$1.02 \times 10^{-4}$	$1.02 \times 10^{-4}$
SC ( $N = 10^{24}m^{-3}$ )	0.8	$1.52 \times 10^{-3}$	$1.61 \times 10^{-3}$
SC ( $N = 10^{24}m^{-3}$ )	1.2	$2.31 \times 10^{-3}$	$2.38 \times 10^{-3}$
ICWM	0.8	0.981	$2.65 \times 10^6$
ICWM	1.2	$2.20 \times 10^6$	$3.98 \times 10^6$
PEC ICWM	any	$\infty$	$\infty$

large and spatial dispersion effects are important (i.e., the relation between displacement field and electric field is strongly nonlocal, and the nonlocal contribution decays algebraically rather than exponentially). However, for metals and semiconductors the screening length  $L_\alpha$  is quite small and spatial dispersion effects are relatively unimportant (the ENZ condition can be approximately satisfied regardless of field polarization)

For the semiconductor (SC) we assumed  $T = 300$  K,  $m = 0.26m_e$ ,  $\varepsilon_h = 12$ . For gold,  $N = 5.9 \times 10^{28} [m^{-3}]$ , and  $v_F = 1.4 \times 10^6 [m/s]$ . For the ICWM we used  $\varepsilon_h = 1$ ,  $a = \lambda_0/10$ , and  $r_w = a/100$ . For the imperfectly conducting wires,  $\varepsilon_m = 1 - \omega_m^2 / (\omega(\omega - j\Gamma))$  where  $\omega_m = 1.37 \times 10^{16} [s^{-1}]$  and  $\Gamma = 5 \times 10^{13} [s^{-1}]$ .

It can be seen that the wire medium (having a large screening length  $L_\alpha$ ) cannot realize the ENZ condition excepting either the first or second scenarios described above (e.g. TEM or TE waves). In fact, by looking carefully at previous successful attempts for realizing the ENZ condition using a wire medium, one can see that the third scenario was not implicated. For example, in [41] only a perpendicular electric field exists (which is the first scenario). However, if one tries to realize an ENZ section inside a waveguide carrying a TM wave (third scenario), the wire medium will not be able to completely provide the ENZ condition. To validate this, we consider an x-band rectangular waveguide as shown in Fig. 5.2, with height  $b=1.016$  cm and width  $a=2.286$  cm. The waveguide has total length 15 cm, with a 5 cm section at each end filled with a simple dielectric having

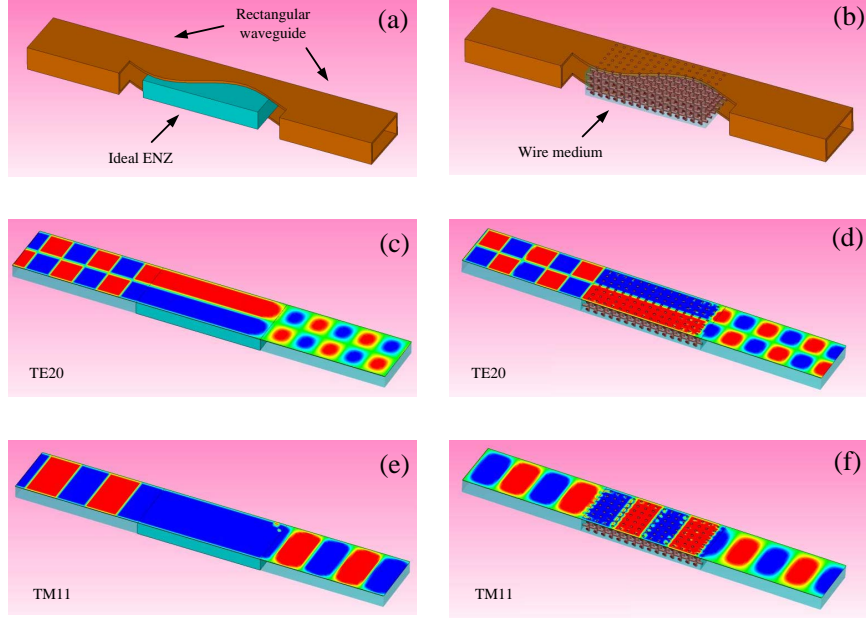


Figure 5.2: Waveguide with a section of ENZ material: a. depicts an idealized ENZ material in the center region of the waveguide, otherwise filled with a simple constant-permittivity medium, and b. shows the section filled with an isotropic wire medium. c.  $TE_{20}$  mode in the idealized ENZ, d.  $TE_{20}$  mode in the actual wire medium, e.  $TM_{11}$  mode in the idealized ENZ, and f.  $TM_{11}$  mode in the actual wire medium.

$\varepsilon = 1.5$ , and a 5 cm long center region containing an ENZ medium. The frequency of operation is 16.5 GHz, well above cutoff to allow both TE and TM modes to propagate. All simulations were performed using CST Microwave Studio [55].

Fig. 5.2(a) depicts the waveguide with a section of idealized ENZ material (with the permittivity set to  $\varepsilon_h = 0.1$ ), and Fig. 5.2(b) shows the section filled with an isotropic wire medium. The host material of the wire medium has  $\varepsilon_h = 8$ , and the wire period and radius are 3.2 mm and 0.5 mm, respectively. At the operating frequency, for a local wire-medium plasma model this would result in an ENZ condition (the plasma frequency is 16.7 GHz).

Fig. 5.2(c) shows the result for the  $TE_{20}$  mode for the idealized ENZ material. It can be seen that the material is acting like an ENZ material, since the wavelength in the center section is much longer than in the two ends (where  $\varepsilon_h = 1.5$ ). Fig. 5.2(d) shows the corresponding result when the wire medium fills the center region. As expected for

a purely-transverse TE mode (scenario 1 above), the wire medium also acts as an ENZ material for the TE mode. Fig. 5.2(e) shows the result for the idealized ENZ material for the  $TM_{11}$  mode, where, as expected, wavelength in the center section is much longer than in the two ends, similar to the TE case. Finally, Fig. 5.2(f) shows the corresponding result for the TM mode for the actual isotropic wire medium. It is evident that the material does not function as an ENZ medium for the TM mode. Given that the TM mode has both transverse and longitudinal components, it corresponds to scenario 3 above (a combination of scenarios 1 and 2). Because the wire medium does not produce a small screening length  $L_\alpha$  (see Table 5.1), and because the longitudinal field is not negligible compared to the transverse field, for the TM mode the wire medium does not produce the ENZ condition. However, for a waveguide filled with a semiconductor we would expect to see the ENZ condition for both TE and TM modes (however, the simulation is not possible in CST).

Based on Table 5.1, ICWM cannot be used to realize the ENZ condition for an arbitrary excitation. Of course, the screening length of the ICWM in Table 5.1 is obtained for specific wire parameters (such as wire period and radius). It can be shown that even with changing the parameters of the ICWM, the screening length is extremely large. To clarify this, Fig. 5.3 shows the normalized screening length of an ICWM as a function of the wire period (a) and radius ( $r_w$ ). The wire material is the same as the imperfectly-conducting ICWM in Table 5.1, and the frequency is  $\omega = 1.2\omega_p$ . As Fig. 5.3 shows, the normalized screening length is very large, which differentiates the ICWM from the natural materials described in the table.

In summary, in this chapter the “space-domain” nonlocal permittivity  $\underline{\varepsilon}(\mathbf{r} - \mathbf{r}')$  has been obtained and a new characteristic screening length introduced for spatially dispersive materials, including artificial wire media. Unlike the Debye length, the new characteristic length relates polarization to the total electric field inside the material, and so it can be used to study the electric displacement distribution in relation to the ENZ condition.

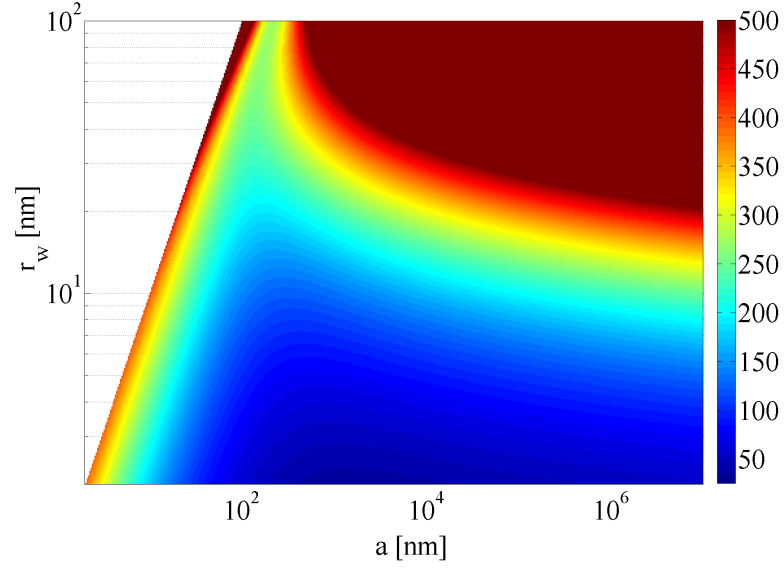


Figure 5.3: Normalized screening length of the ICWM ( $L_\alpha/\lambda_0$ ) as a function of the wire period ( $a$ ) and radius ( $r_w$ ) at  $\omega = 1.2\omega_p$ .

Using some typical values semiconductor and wire medium metamaterials, it was shown that the new characteristic length is very small for semiconductors and therefore an ENZ condition can be easily obtained. However, for wire media the ENZ condition cannot be identically obtained except in some special cases, and often only the perpendicular displacement field can vanish.



## Chapter 6

### Homogenization example: hyperlensing by a graphene monolayer [6]

In this chapter, the canalization of terahertz surface plasmon polaritons using a modulated graphene monolayer is investigated for subwavelength imaging. An anisotropic surface conductivity formed by a set of parallel nanoribbons with alternating positive and negative imaginary conductivities is used to realize the canalization regime required for hyperlensing. The ribbons are narrow compared to the wavelength, and are created electronically by gating a graphene layer over a corrugated ground plane. Good quality canalization of surface plasmon polaritons is shown in the terahertz even in the presence of realistic loss in graphene, with relevant implications for subwavelength imaging applications.

#### 6.1 introduction

Graphene, the first 2D material to be practically realized [56], has attracted great interest in the last decade. The fact that electrons in graphene behave as massless Dirac-Fermions leads to a variety of anomalous properties [57; 58], such as charge carriers with ultra high-mobility and long mean-free paths, gate-tunable carrier densities, and anomalous quantum Hall effects [59]. Graphene's electrical properties have been studied in many previous works [60; 61; 62; 63; 64; 65; 66; 67; 68; 69] and are often represented by a local complex surface conductivity given by the Kubo formula [70; 71]. Since its surface conductivity leads to attractive surface plasmon properties, graphene has become a good candidate for plasmonic applications, especially in the terahertz (THz) regime [72; 73; 74; 75; 76; 77; 78; 53].

Surface plasmons (SPs) are the collective charge oscillations at the surface of plasmonic materials. SPs coupled with photons form the composite quasi-particles known as surface plasmon polaritons (SPPs). Theoretically, the dispersion relationship for SPPs on a surface can be obtained as a solution of Maxwell's equations [79]. In this approach it is easy to show that, in order to support the SPP, 3D materials with negative bulk permittivities (*e.g.*, noble metals) or 2D materials with non-zero imaginary surface conductivities (*e.g.*, graphene) are essential. Although SPPs on metals and on graphene have considerable qualitative similarities, graphene SPPs generally exhibit stronger confinement to the surface, efficient wave localization up to mid-infrared frequencies [80; 74], and they are highly tunable (which is one of their most unique and important properties)[58]. Applications of graphene SPPs include electronics [81; 82; 83], optics [84; 85; 86], THz technology [87; 88; 89; 90], light harvesting [91], metamaterials [92], and medical sciences [93; 94].

In this chapter we study the canalization of SPPs on graphene, which can have direct applications for sub-wavelength imaging using THz sources.

Sub-wavelength imaging using metamaterials was first reported by Pendry in 2000 [95]. His technique [96] was based on backward waves, negative refraction and amplification of evanescent waves. More recently, another more robust venue for subwavelength imaging was proposed, based on metamaterials operating in the so called “canalization regime” [97; 98; 99]. In this case, the structure (acting as a transmission medium) transfers sub-wavelength images from a source plane to an image plane over distances of several wavelengths, without diffraction [100]. This form of super-resolving imaging, or hyperlensing, can also be realized by a uniaxial wire medium [101]. In these schemes, all spatial harmonics (evanescent and propagating) propagate with the same phase velocity from the near- to the far-field. In this paper we discuss the canalization of SPPs on a modulated graphene monolayer. In Ref. [102], it was shown that the near field of a vertical point source placed in close proximity to a graphene monolayer couples primarily to the

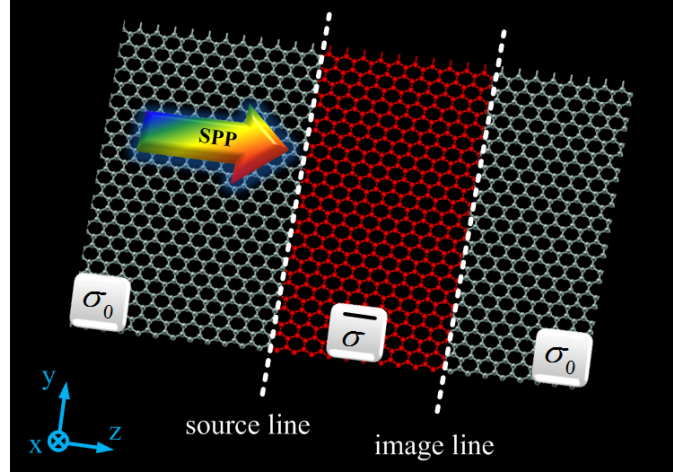


Figure 6.1: An infinite graphene layer in the  $yz$ -plane. The conductivity of graphene is isotropic ( $\sigma_0$ ) everywhere except in the red region, where it is anisotropic ( $\bar{\sigma}$ ). The anisotropic region will be created by a suitable gate bias.

field of an SPP strongly confined to the monolayer. By creating an anisotropic graphene surface as alternating graphene nanoribbons with positive and negative imaginary surface conductivities, we achieve SPP canalization and hyperlensing of the near-field of an arbitrary source.

To achieve canalization, it is necessary to realize a flat isofrequency contour[103]. Here, taking the same definition for canalization as for a 3D material, we first study the conditions for canalization of SPPs on a 2D material such as graphene. Then, a practical geometry is proposed and verified for the hyperlens implementation.

## 6.2 Theory and formulation

Figure 6.1 shows an infinite graphene layer in the  $yz$ -plane suspended in vacuum. Its surface conductivity is assumed isotropic ( $\sigma_0$ ) everywhere except in the region between the source and image lines (red colored region), which is anisotropic and is given as

$$\bar{\sigma} = \sigma_y \hat{\mathbf{y}}\hat{\mathbf{y}} + \sigma_z \hat{\mathbf{z}}\hat{\mathbf{z}} = -j \left( \sigma_y^i \hat{\mathbf{y}}\hat{\mathbf{y}} + \sigma_z^i \hat{\mathbf{z}}\hat{\mathbf{z}} \right), \quad (6.1)$$

where for now  $\sigma_{y,z}$  are assumed to be imaginary-valued, (to be generalized later)  $\sigma_{y,z} = 0 - j\sigma_{y,z}^i$ . For an SPP traveling over such an anisotropic graphene layer, it is possible [see the appendix] to show that the governing dispersion relation is

$$k_z^2 \left( \frac{\sigma_z^i}{\sigma_z^i + \sigma_y^i} \right) + k_y^2 \left( \frac{\sigma_y^i}{\sigma_z^i + \sigma_y^i} \right) - k_0^2 = \frac{k_0 k_x}{\sigma_z^i + \sigma_y^i} \left( \frac{2}{\eta_0} - \frac{\eta_0 \sigma_y^i \sigma_z^i}{2} \right), \quad (6.2)$$

where  $k_0$  is the wavenumber in free space,  $\eta_0 = \sqrt{\mu_0/\varepsilon_0}$  is the intrinsic impedance of vacuum,  $k_x = \sqrt{k_y^2 + k_z^2 - k_0^2}$ , and the 2D spatial Fourier transform variables are  $(y, z) = (k_y, k_z)$ .

From (6.2), an ideal canalization regime can be realized when

$$\sigma_y^i \rightarrow 0; \quad \sigma_z^i \rightarrow \infty, \quad (6.3)$$

simultaneously, such that (6.2) becomes

$$k_z = k_0, \quad (6.4)$$

independent of  $k_y$ . Equation (6.4) implies that all of the transverse spatial harmonics ( $k_y$  of the SPPs) will propagate with the same wavenumber (phase velocity) in the  $z$ -direction. In this situation, which is analogous to the canalization regime in 3D metamaterials, any SPP distribution at the source line in Fig. 6.1 will be transferred to the image line without diffraction or any phase distortion. Condition (6.3) is somewhat analogous to the condition required for canalization of 3D waves in Ref. [104], but with the difference that here the extreme parameters (6.3) yield a finite wave number, equal to the background medium surrounding the modulated graphene layer, and not zero as for the 3D case. This is to be expected, since the canalized SPPs still need to be above the light cone to avoid radiation and leakage in the background medium. Quite peculiarly, it follows from (6.4) that

the confinement in the transverse ( $x$ ) direction of each SPP is proportional to its spatial frequency along  $y$ , i.e.,  $k_x = k_y$ .

It might seem difficult to find a natural 2D material providing (6.3) for canalization. However, it can be shown [see the appendix] that a modulated isotropic conductivity  $\sigma(z)$  can act as an effective anisotropic conductivity,

$$\sigma_y^{\text{eff}} = \frac{1}{T} \int_{\langle T \rangle} \sigma(z) dz, \quad (6.5)$$

$$\frac{1}{\sigma_z^{\text{eff}}} = \frac{1}{T} \int_{\langle T \rangle} \frac{1}{\sigma(z)} dz, \quad (6.6)$$

where  $\sigma(z)$  is assumed to be periodic with period  $T$ , and the integrations are over one period. Note that  $T$  should be small compared to the wavelength in order to provide valid effective parameters. Therefore, if the isotropic conductivity of graphene is properly modulated (*e.g.*, by electrical gating or chemical doping), its effective anisotropic conductivity can indeed satisfy (6.3).

In the following, two conductivity modulations will be analyzed whose effective anisotropic conductivities satisfy (6.3) and are thus in principle capable of canalizing SPPs. Since we will use full-wave simulations to confirm the canalization geometries, a section in the appendix is dedicated to modeling of graphene in commercial simulation codes using finite-thickness dielectrics.

### 6.3 Realization of the hyperlens

In previous canalization metamaterials, or hyperlenses, using alternating positive and negative dielectrics, an idealized, abrupt transition has been assumed between layers. For graphene, this would be analogous to strips having abrupt transitions between positive and negative imaginary-part conductivities. We refer to this as the hard-boundary case,

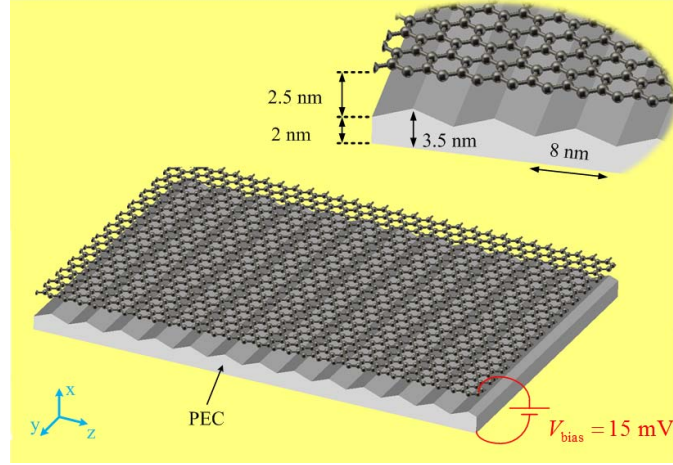


Figure 6.2: Triangular ridged ground plane for achieving conductivity modulation (leading to a soft-boundary profile).

and analyze it in detail in the appendix. However, given the finite quantum capacitance of graphene, such an abrupt transition is impossible to achieve. A more realistic modulation scenario for a conductivity profile satisfying (6.3) can be obtained in the geometry of Fig. 6.2. It consists of an infinite sheet of graphene gated by a ridged ground plane, as shown in the insert of Fig. 6.2. Performing a static analysis, it is possible to obtain the charge density on the graphene layer, which may in turn provide the chemical potential and the conductivity of graphene following a method analogous to Ref. [53]. Figure 6.3 shows the calculated conductivity of the graphene layer as a function of  $z$  (using the complex conductivity predicted by the Kubo formula; see Ref. [67] for the explicit expression for  $f = 10$  THz,  $T = 3$  K,  $\Gamma = 0.215$  meV).

Two important conclusions can be drawn from Fig. 6.3: i) the imaginary part of conductivity dominates the real part, as desired, and ii) its distribution is almost perfectly sinusoidal, which, after insertion into (6.5) and (6.6), satisfies (6.3). Therefore, the geometry of Fig. 6.2 may be expected to support canalization. The resulting graphene nanoribbons have a realistic smooth variation in conductivity; we refer to this geometry as the soft-boundary scenario, considered in the following.

As an example, two point sources are placed in front of the source line in Fig. 6.1, exciting SPPs on the graphene layer. The point sources are separated by  $20 \text{ nm} = 0.15\lambda_{\text{SPP}}$ ,

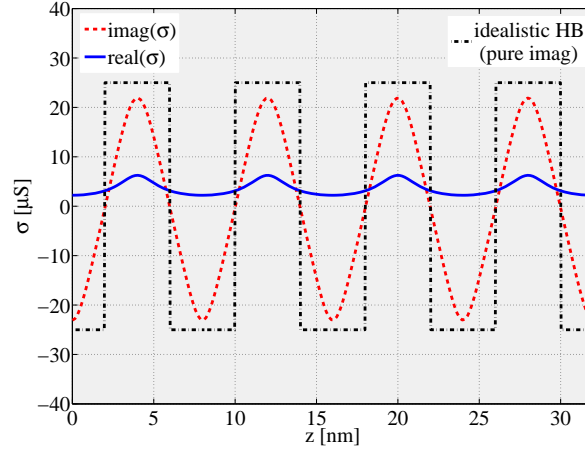


Figure 6.3: The conductivity distributions resulting from the bias modulation scheme depicted in Fig. 6.2. Also shown is the idealized hard-boundary case discussed in the appendix.

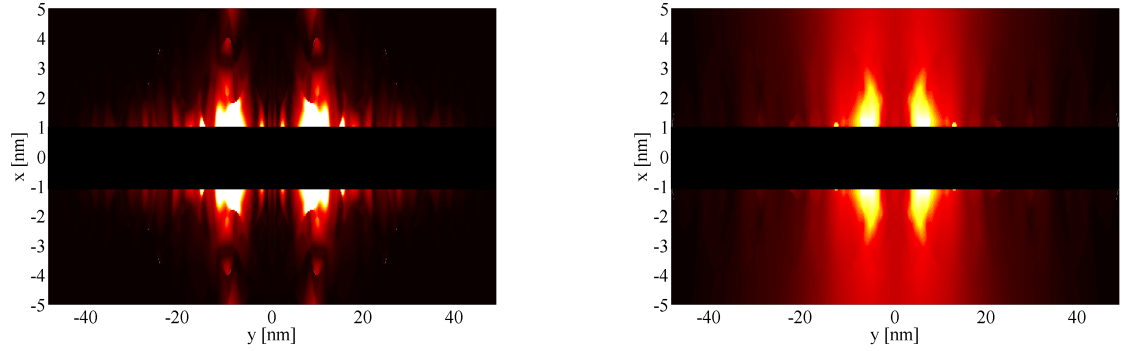


Figure 6.4: The normalized  $x$ -component of the electric field at the source (left) and image (right) planes of the modulated graphene surface. Source and image lines are at separated by  $2\lambda_{\text{SPP}}$  (the region  $-1 < x < 1$  is the dielectric slab model of graphene).

where  $\lambda_{\text{SPP}} = 133$  nm using (S.2) in appendix section, and the canalization area (the region between the source and the image lines) has length  $2\lambda_{\text{SPP}} = 250$  nm and width of 100 nm (which is large compared to the separation between sources).

Figure 6.4 shows the  $x$ -component of the electric field at the source line and image line (at the end of the modulated region). The plot of the normalized  $x$ -component of the field at  $x = 1$  nm is shown in Fig. 6.5, while Figure 6.6 shows the  $x$ -component of the electric field above the modulated graphene surface, and a homogenous graphene surface with

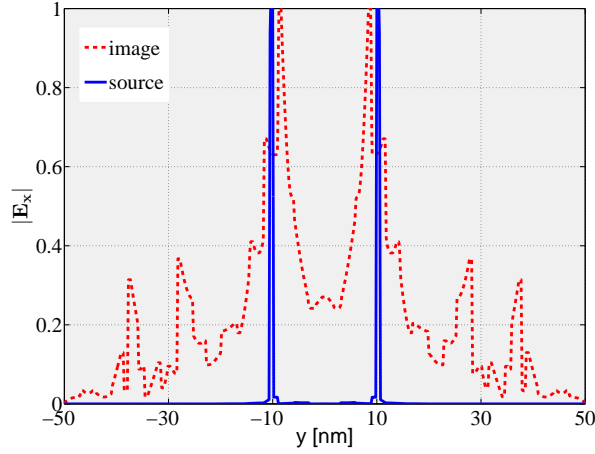


Figure 6.5: The normalized  $x$ -components of the electric field at the source and image lines on the surface of the modulated graphene ( $x = 1$  nm).

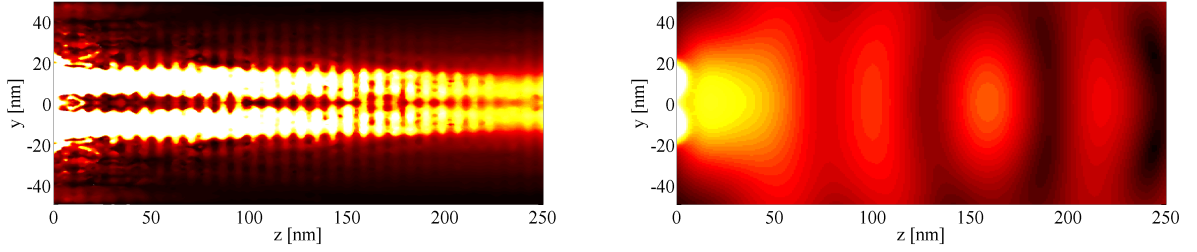


Figure 6.6: Normalized  $x$ -component of the electric field above the modulated graphene surface (left) and a homogenous graphene surface (right).

conductivity  $\sigma = -j23.5 \mu\text{S}$ . This shows quite strikingly how the canalization occurring on the modulated graphene can avoid the usual diffraction expected on a homogeneous layer. Figs. S.3-S.5 in the appendix section show consistent results for the hard-boundary case.

It is easy to show that (6.5) and (6.6) cannot be exactly satisfied if the conductivity includes loss (i.e., the real part of  $\sigma$ ). Therefore as loss increases, the phase velocities will differ among various spatial components and, as a result, one would expect to see a blurred image, and eventually no image, as loss further increases. To investigate this deterioration effect, we decrease the canalization length to  $200 \text{ nm} = 1.5\lambda_{\text{SPP}}$  and increase the



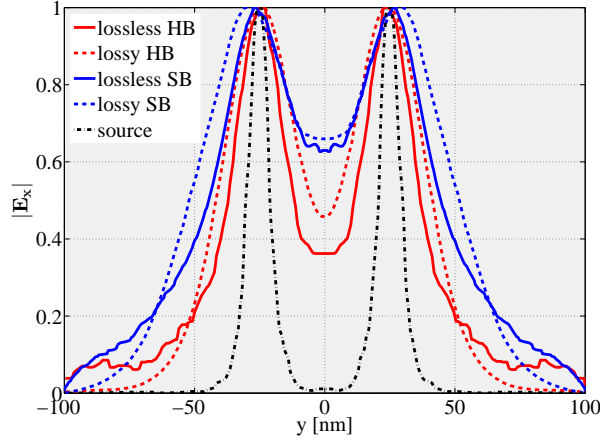


Figure 6.7: The effect of loss on the image canalization for hard- and soft-boundary bias modulations.

separation between sources to  $50 \text{ nm} = 0.4\lambda_{\text{SPP}}$  (which we found necessary to maintain accuracy in the simulation). The geometry is then simulated for soft- and hard-boundary cases (with and without loss for each case) and the  $x$ - components of the electric field at  $x = 10 \text{ nm}$  are shown in Fig. 6.7. The curves are calculated in the image line at a distance  $1 \text{ nm}$  above the graphene surface.

Comparison between the four curves in Fig. 6.7 shows that the lossless hard- and soft-boundary examples yield similar results, as expected since their effective surface conductivity satisfies (6.3) exactly. In fact, as long as the period is small compared to the wavelength, any modulation which has half-wave symmetry will satisfy (6.3), leading to perfect canalization.

However, adding loss causes the effective surface conductivities to have non-vanishing real parts, and therefore (6.3) cannot be exactly satisfied. In the lossy case, the modulation scheme is important, since it affects how closely (6.3) can be satisfied. For example, Fig. 6.7 shows that the idealistic hard-boundary model exhibits better resolution than the realistic soft-boundary model.

Image degradation due to loss can be lessened by working at higher frequencies. In fact, the maximum of the ratio  $\text{Im}(\sigma)/\text{Re}(\sigma)$  may be increased by adjusting the chemical potential at higher frequencies. In the appendix section the ratio  $\text{Im}(\sigma)/\text{Re}(\sigma)$  is plotted

as a function of chemical potential and frequency, and its optimal value for three different frequencies is used to simulate to the same geometry. The simulation results confirm the improvement of canalization as frequency increases.

Our results show that a triangular ridged ground plane to bias the graphene monolayer indeed allows canalization and hyperlensing, since its effective conductivities given by (6.5) and (6.6) satisfy (6.3). However, there are many possible  $\sigma(z)$  functions that, after inserting them into (6.5) and (6.6), will satisfy (6.3). As an example, the sinusoidal conductivity of Fig. 6.3 can also be implemented using a rectangular ridged ground plane (details are shown in the appendix section).

## 6.4 Summary

We have analyzed the possibility to produce in-plane canalization of SPPs on a 2D surface, with particular emphasis on its realization in a realistically modulated graphene monolayer, resulting in a planarized 2D hyperlens on graphene. We envision the use of this effect on a ridged ground plane for sub-wavelength imaging of THz sources and to arbitrarily tailor the front wave of an SPP by suitably designing the boundary of the canalization region.

## 6.5 Appendix

### 6.5.1 On the modeling of graphene layer by a thin dielectric

Modeling graphene as a 2D surface having an appropriate value of surface conductivity  $\sigma$  is an accurate approach for a semiclassical analysis (e.g., the Drude model for intraband contributions has been verified experimentally [105; 106; 107], and the interband model and the visible-spectrum response have also been verified [107]). However, often it is convenient to model graphene as a thin dielectric layer, which is easily implemented in

typical electromagnetic simulation codes. It is common to consider an equivalent dielectric slab with the thickness of  $d$  and a 3D conductivity of  $\sigma_{3D} = \sigma/d$ . The corresponding bulk (3D) relative permittivity is [72]

$$\varepsilon_{3D} = 1 + \frac{\sigma}{j\omega\varepsilon_0 d}, \quad (6.7)$$

where  $\omega$  is the angular frequency. However, for calculations in which the geometry is discretized (e.g., in the finite-element method), fine features in the geometry such as an electrically-thin slab demand finer discretization, which in turn requires more computational costs. Thus, whereas sub 1 nm thickness values may seem more physically-appropriate, numerical considerations often lead to the use of a thicker material. As an example, in Ref. [72] the thickness of the dielectric slab is assumed to be 1 nm.

However, the accuracy of the dielectric model degrades as the thickness of the slab increases. Since this model is widely adopted, yet a detailed consideration of this effect has not been previously presented, we briefly consider this topic below.

Consider a transverse magnetic SPP on an infinite graphene layer. The SPP wavelength using the 2D conductivity is [67]

$$\lambda_{\text{SPP}} = \lambda_0 \left( 1 - \left( \frac{2}{\eta_0 \sigma} \right)^2 \right)^{-0.5}, \quad (6.8)$$

where  $\lambda_0$  is the wavelength in free space. On the other hand, in Ref. [108] it is shown that a dielectric slab with negative permittivity ambient in a medium with positive permittivity can support two sets of dielectric modes (even and odd). The odd modes have the wavelength (assuming vacuum as the ambient medium)

$$\lambda_{\text{odd}} = 2\pi \left( -\frac{2}{d} \coth^{-1} \varepsilon_{3D} \right)^{-1}, \quad (6.9)$$

where  $\varepsilon_{3D}$  and  $d$  are the dielectric slab permittivity and thickness, respectively. It is shown in Ref. [108] that the odd modes can exist only if

$$\varepsilon_{3D} < -1. \quad (6.10)$$

It can also be noticed that the modal field distribution outside of the slab is similar to that of a SPP on graphene. It is easy to show that in the limit of  $d \rightarrow 0$  and using (6.7), the dielectric-slab odd mode becomes the graphene SPP mode  $\lambda_{\text{odd}} \rightarrow \lambda_{\text{SPP}}$ . It can be shown that (6.9) is a good approximation for  $\lambda_{\text{SPP}}$  only if three conditions are satisfied as [see the next sub-section]

$$\frac{d}{\lambda_{\text{SPP}}} \ll 1, \quad (6.11)$$

$$|\sigma| \ll \frac{2}{\eta_0}, \quad (6.12)$$

$$\left| \frac{\sigma}{d} \right| > 2\omega\varepsilon_0. \quad (6.13)$$

Equation (6.13) is in fact the direct insertion of (6.7) into (6.10). Based on (6.13), as the  $\sigma/d$  ratio increases, the dielectric slab becomes a better approximation (as long as (6.12) is not violated). To consider this, Fig. 6.8 shows the frequency independent error (%) of using the dielectric slab model for graphene as a function of the normalized  $d$  and  $\sigma$  (assuming  $\sigma$  is imaginary-valued),

$$\text{error}(\%) = \frac{\lambda_{\text{odd}} - \lambda_{\text{SPP}}}{\lambda_{\text{SPP}}} \times 100. \quad (6.14)$$

As a numerical example (using equations (3) and (4) in Ref. [67]), for  $d = 2 \text{ nm}$ , the scattering rate  $\Gamma = 0.215 \text{ meV}$ , and chemical potential  $\mu_c = 0.03 \text{ eV}$  at  $f = 10 \text{ THz}$  and very low temperature ( $T = 3 \text{ K}$ ), the normalized thickness and conductivity will be  $d/\lambda_0 = 66.7 \times 10^{-6}$  and  $\sigma = 1.1 - j23 \mu\text{S}$  which leads to an error of 4.9%. This is set as the maximum error that is allowed in the rest of this work.

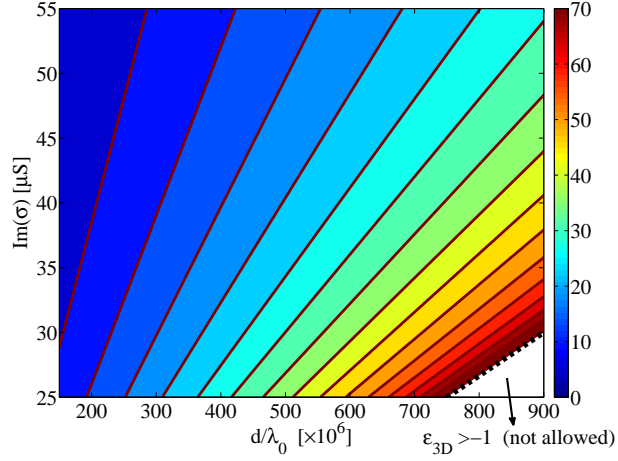


Figure 6.8: The error (6.14) as a function of the normalized dielectric thickness and conductivity of graphene. The graph is frequency independent.

### 6.5.2 Proof of (6.13)

From (6.9),

$$\coth\left(\frac{d|\beta_{\text{odd}}|}{2}\right) = \frac{\sigma^i}{\omega\epsilon_0 d} - 1 \quad (6.15)$$

where  $\beta_{\text{odd}} = 2\pi/\lambda_{\text{odd}}$  and  $\sigma = -j\sigma^i$ .

Assuming  $d/\lambda_{\text{odd}} \ll 1$ , (6.15) leads to

$$\frac{2}{d|\beta_{\text{odd}}|} + \frac{d|\beta_{\text{odd}}|}{6} - \dots = \frac{\sigma^i}{\omega\epsilon_0 d} - 1. \quad (6.16)$$

After keeping only the first term of the series in (6.16) and using the assumption  $d/\lambda_{\text{odd}} \ll 1$ ,

$$\frac{|\lambda_{\text{odd}}|}{\lambda_0} = \frac{\sigma^i \eta_0}{2}. \quad (6.17)$$

Comparing (6.17) and (6.8),  $\lambda_{\text{odd}}$  is a good approximation of  $\lambda_{\text{SPP}}$  only if

$$|\sigma^i| \ll \frac{2}{\eta_0}. \quad (6.18)$$

### 6.5.3 Proof of (6.2)

For the anisotropic region of Fig. 6.1, consider a general magnetic field in the Fourier transform domain as

$$\mathbf{H} = e^{-jk_y y - jk_z z} \times \quad (6.19)$$

$$\begin{cases} (H_x^+ \hat{\mathbf{x}} + H_y^+ \hat{\mathbf{y}} + H_z^+ \hat{\mathbf{z}}) e^{-\sqrt{k_y^2 + k_z^2 - k_0^2} x} & x > 0 \\ (H_x^- \hat{\mathbf{x}} + H_y^- \hat{\mathbf{y}} + H_z^- \hat{\mathbf{z}}) e^{\sqrt{k_y^2 + k_z^2 - k_0^2} x} & x < 0 \end{cases}$$

where  $H_{x,y,z}^{+,-}$  are constants. Equation (6.19) is chosen so that it satisfies the Helmholtz equation and has the form of a plasmonic wave.

Using Ampere's law to find the electric field in each region and satisfying the boundary conditions

$$H_y^+ - H_y^- = \sigma_z E_z, \quad (6.20)$$

$$H_z^+ - H_z^- = -\sigma_y E_y, \quad (6.21)$$

$$H_x^+ = H_x^-, \quad (6.22)$$

it is straightforward to show that

$$H_y^- = -H_y^+, \quad (6.23)$$

$$H_z^- = -H_z^+, \quad (6.24)$$

$$\begin{bmatrix} \sigma_z j k_y & Y & 0 \\ j k_z \sigma_y & 0 & Z \\ j k_x & j \omega \varepsilon_0 k_y & j \omega \varepsilon_0 k_z \end{bmatrix} \begin{bmatrix} H_x^+ \\ H_y^+ \\ H_z^+ \end{bmatrix} = 0, \quad (6.25)$$

where  $Y = -2j\omega\varepsilon_0 - \sigma_z k_x$ , and  $Z = -2j\omega\varepsilon_0 - k_x \sigma_y$ . Setting the determinant of the above matrix to zero leads to (6.2).

It is easy to show that in the isotropic limit ( $\sigma_y = \sigma_z = \sigma_0$ ), (6.2) simplifies to the well-known dispersion equations [62; 67]  $k_x = -\frac{2jk_0}{\eta_0\sigma_0}$ , and  $k_x = -\frac{jk_0\eta_0\sigma_0}{2}$ , for transverse magnetic (TM) and transverse electric (TE) surface waves, respectively. The solution of (6.2) will lead to a solution for the SPP with the magnetic field

$$\mathbf{H} = e^{-k_x x - j k_y y - j k_z z} \times \left( \hat{\mathbf{x}} + \frac{j \sigma_z k_y}{2j\omega\varepsilon_0 + k_x \sigma_z} \hat{\mathbf{y}} + \frac{j \sigma_y k_z}{2j\omega\varepsilon_0 + k_x \sigma_y} \hat{\mathbf{z}} \right). \quad (6.26)$$

In the canalization regime, the SPP given by (6.26) is a TM mode with respect to the canalization direction ( $z$ -direction in our notation) and its magnetic field has a peculiar circular polarization,

$$\mathbf{H} = (\hat{\mathbf{x}} + j \hat{\mathbf{y}}) e^{-k_y(x+jy) - j k_0 z}. \quad (6.27)$$

It is also interesting that the confinement in the  $x$ -direction of each SPP harmonic is proportional to  $k_y$ .

#### 6.5.4 Proof of (6.5) and (6.6)

Assume a sheet of graphene with a periodic isotropic conductivity in the  $z$ -direction ( $\sigma(z) = \sigma(z + T)$ ) as shown in Fig. 6.9. Enforcing a constant, uniform, and  $z$ -directed surface current ( $J_z$ ) on the graphene induces an electric field on the graphene as

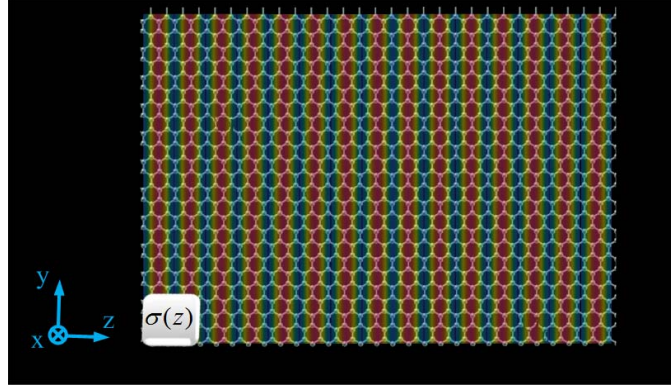


Figure 6.9: An infinite graphene layer with isotropic periodic conductivity of  $\sigma(z)$ .

$$E(z) = \frac{J_z}{\sigma(z)}. \quad (6.28)$$

Defining average parameters leads to

$$E_{\text{av}} = \frac{J_z}{\sigma_{\text{av},z}} = \frac{1}{L} \int_{\langle L \rangle} \frac{J_z}{\sigma(z)} dz, \quad (6.29)$$

$$\frac{1}{\sigma_{\text{av},z}} = \frac{1}{L} \int_{\langle L \rangle} \frac{1}{\sigma(z)} dz. \quad (6.30)$$

Enforcing a constant, uniform and  $y$ -directed electric field ( $E_y$ ) induces a surface current on the graphene as

$$J_y(z) = \sigma(z) E_y \quad (6.31)$$

which is (6.5).

Defining average parameters leads to

$$J_{y,\text{av}}(z) = \sigma_{\text{av},y} E_y = \frac{1}{L} \int_{\langle L \rangle} \sigma(z) E_y dz, \quad (6.32)$$

$$\sigma_{\text{av},y} = \frac{1}{L} \int_{\langle L \rangle} \sigma(z) dz, \quad (6.33)$$



which is (6.6).

### 6.5.5 Idealized graphene nanoribbons with hard-boundaries

An idealization of the modulation scheme discussed in the text would consist of alternating positive and negative imaginary conductivities, with each strip terminating in a sharp transition between positive and negative values (see Fig. 6.13). We assume that all of the strips have the same width  $W = 4 \text{ nm}$  and conductivity modulus  $|\sigma| = 23.5 \mu\text{S}$ , which is the conductivity of a graphene layer for  $f = 10 \text{ THz}$ ,  $T = 3 \text{ K}$ ,  $\Gamma = 0.215 \text{ meV}$  and  $\mu_c = 0.022 \text{ eV}$  or  $\mu_c = 0.03 \text{ eV}$  (for positive and negative  $\text{Im}(\sigma)$ , respectively). The chemical potential is chosen to minimize the loss at the given frequency. In fact, the ratio  $\text{Im}(\sigma)/\text{Re}(\sigma)$  is maximized at this frequency (the ratio is 7 for  $\mu_c = 0.022 \text{ eV}$ ). Since the effect of loss was discussed in the text, here we assume an imaginary-valued conductivity  $\sigma = \pm j23.5 \mu\text{S}$ .

We refer to this idealized conductivity profile as the hard-boundary case, because of the step discontinuity (sharp transition) of the conductivity between neighboring strips. This resembles the geometry in Ref. [104] for canalization of 3D waves in which there are also hard-boundaries between dielectric slabs with positive and negative permittivities.

As a simulation example of the hard-boundary case, two point sources are placed in front of the source line in Fig. 6.1 exciting two SPPs on the graphene layer. The point sources are separated by  $20 \text{ nm} = 0.15\lambda_{\text{SPP}}$  where  $\lambda_{\text{SPP}} = 133 \text{ nm}$  using (6.8), and the canalization area (the region between the source and the image lines) has length  $2\lambda_{\text{SPP}} = 250 \text{ nm}$  and width of  $100 \text{ nm}$  (which is large compared to the separation between sources). Figure 6.10 shows the normalized  $x$ -component of the electric field  $|E_x|$  at the source line and image line (at the end of the modulated region). Fig. 6.11 shows the normalized  $x$ -component of the electric field above the surface of the graphene ( $x = 5 \text{ nm}$ ). Note that the region  $-1 < x < 1 \text{ nm}$  represents the graphene (since we have used a dielectric slab model for graphene with the thickness of  $2 \text{ nm}$ ).

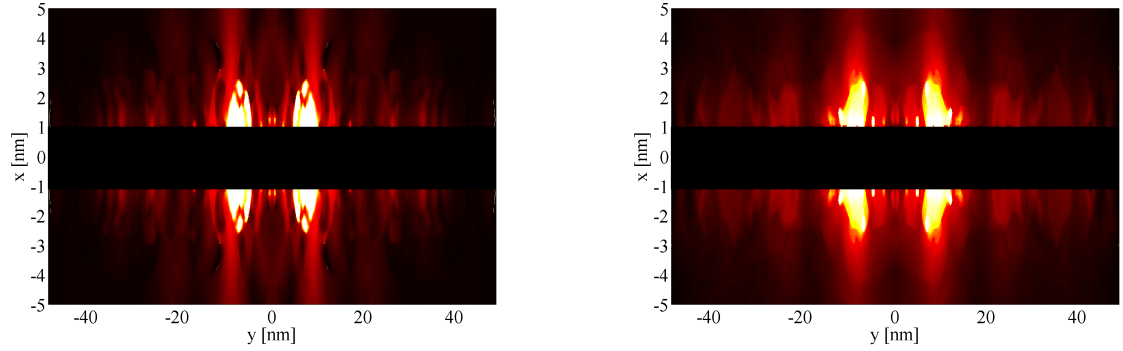


Figure 6.10: The normalized  $x$ -component of the electric field at the source (left) and image (right) planes of the hard-boundary example. Source and image lines are separated by  $2\lambda_{\text{SPP}}$  (the region  $-1 < x < 1$  is the dielectric slab model of graphene).

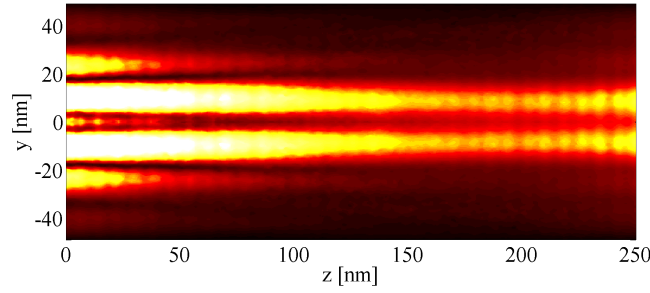


Figure 6.11: Normalized  $x$ -component of the electric field above the graphene surface.

Canalization is evident from Figs. 6.10 and 6.11. Figure 6.12 shows the normalized field intensities at the source and image lines just above the graphene surface ( $x = 1$  nm).

### 6.5.6 Simulation setup for the hard- and the soft-boundary examples

Full-wave simulations have been done using CST Microwave Studio

CST. In this section we consider the dielectric model of graphene. Figure 6.13 shows the simulation setup of the hard-boundary example. The simulation results are given in Figs. 6.10-6.12. The graphene strips can be modeled with dielectric slabs having

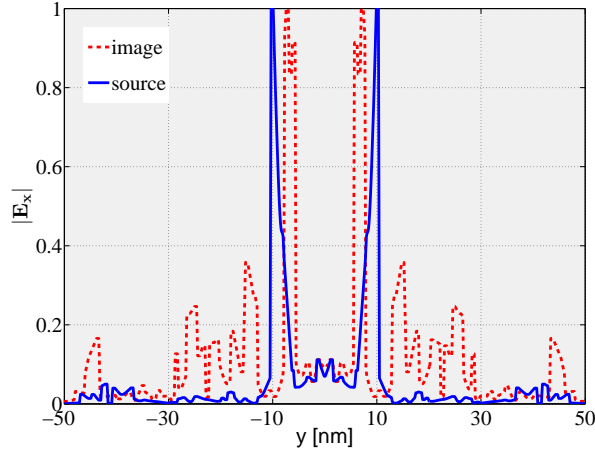


Figure 6.12: The normalized  $x$ -components of the electric field at the source and image lines on the surface of the graphene (taken at the height  $x = 1$  nm) for the hard-boundary example.

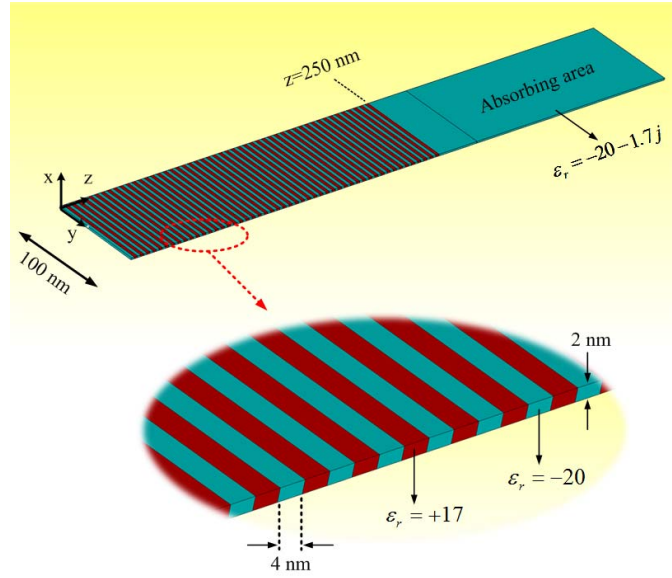


Figure 6.13: The dielectric model of the hard-boundary graphene strip example.

thickness  $d = 2$  nm and, using (6.7), permittivities of  $\varepsilon^- = -20$  and  $\varepsilon^+ = 22$ . However, as shown in the insert of Fig. 6.13, the permittivity  $\varepsilon^+ = 17$  is used rather than  $\varepsilon^+ = 22$  because numerical experiments show that that value leads to better canalization. The difference with our analytically-predicted value for best canalization is seemingly because in our analytical model we have disregarded radiation, reflections from discontinuities, and similar effects.

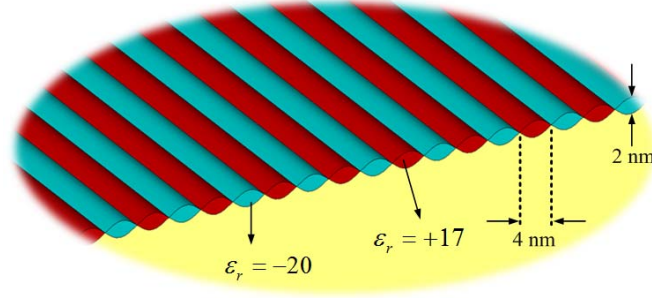


Figure 6.14: The dielectric model for the soft-boundary example - constant permittivities and smoothly-varying thickness model graphene's sinusoidal chemical potential.

For the soft-boundary example, the conductivity of the strips varies smoothly with position. So, applying the dielectric slab model, we could use a dielectric slab with a fixed thickness (e.g.,  $d = 2$  nm) and a position dependent permittivity given by (6.7) as

$$\varepsilon_{3D}(z) = 1 + \frac{\sigma(z)}{j\omega\varepsilon_0 d}. \quad (6.34)$$

However, an alternative method which is easier to implement for simulation is to consider a dielectric slab with fixed permittivity (or permittivities) and a position dependent thickness as

$$d(z) = \frac{\sigma(z)}{(\varepsilon_{3D} - 1)j\omega\varepsilon_0}. \quad (6.35)$$

Obviously, two different  $\varepsilon_{3D}$  values should be chosen for different signs of  $\sigma(z)$  so that  $d(z)$  remains positive. This has been done for the conductivity of Fig. 3, and the resulting dielectric slab model is shown in Fig. 6.14. Comparison between Fig. 6.13 and Fig. 6.14 clearly shows the difference between the hard- and the soft-boundary examples.

### 6.5.7 The improvement of canalization by increasing the frequency

Figure 6.15 shows the ratio  $\text{Im}(\sigma)/\text{Re}(\sigma)$  versus chemical potential at three different frequencies, showing that, as frequency increases, loss becomes less important. Note also that the value of chemical potential that maximizes the conductivity ratio is considerably

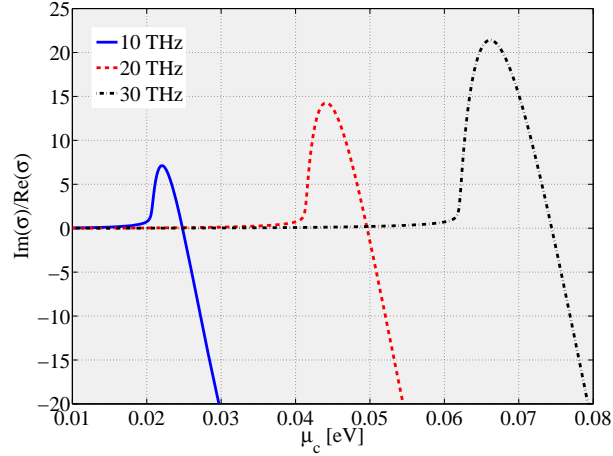


Figure 6.15: The ratio  $\text{Im}(\sigma)/\text{Re}(\sigma)$  as a function of chemical potential for three different frequencies.

frequency dependent. In Fig. 6.16 the effect of decreasing loss as a result of the frequency increase is investigated. To do so, the peak ratio  $\text{Im}(\sigma)/\text{Re}(\sigma)$  of the three curves in Fig. 6.15 are chosen associated with frequencies 10, 20, and 30 THz. These ratios are assigned to a same geometry (and holding frequency constant) and the  $x$ -component of the electric fields are shown in Fig. 6.16 (the scalings are the same). In this way, all of the electrical lengths (such as the electrical length of the nanoribbons, canalization region, etc.) remain the same and only the effect of loss is incorporated. From Fig. 6.16, it is obvious that the increase of frequency improves the canalization. However, since the dimensions become smaller, fabrication becomes more difficult.

### 6.5.8 Modulated graphene conductivity using a rectangular ridged ground plane

The sinusoidal conductivity of Fig. 3 can be implemented using a rectangular ridged ground plane, as shown in Fig. 6.17. The conductivity distribution of the geometry in Fig. 6.17 is shown in Fig. 6.18 and is almost identical to Fig. 3, although their ground plane geometries are different. Obviously, the ideal canalization behavior of the two geometries is very similar. Interestingly, the rectangular ridged ground plane has to

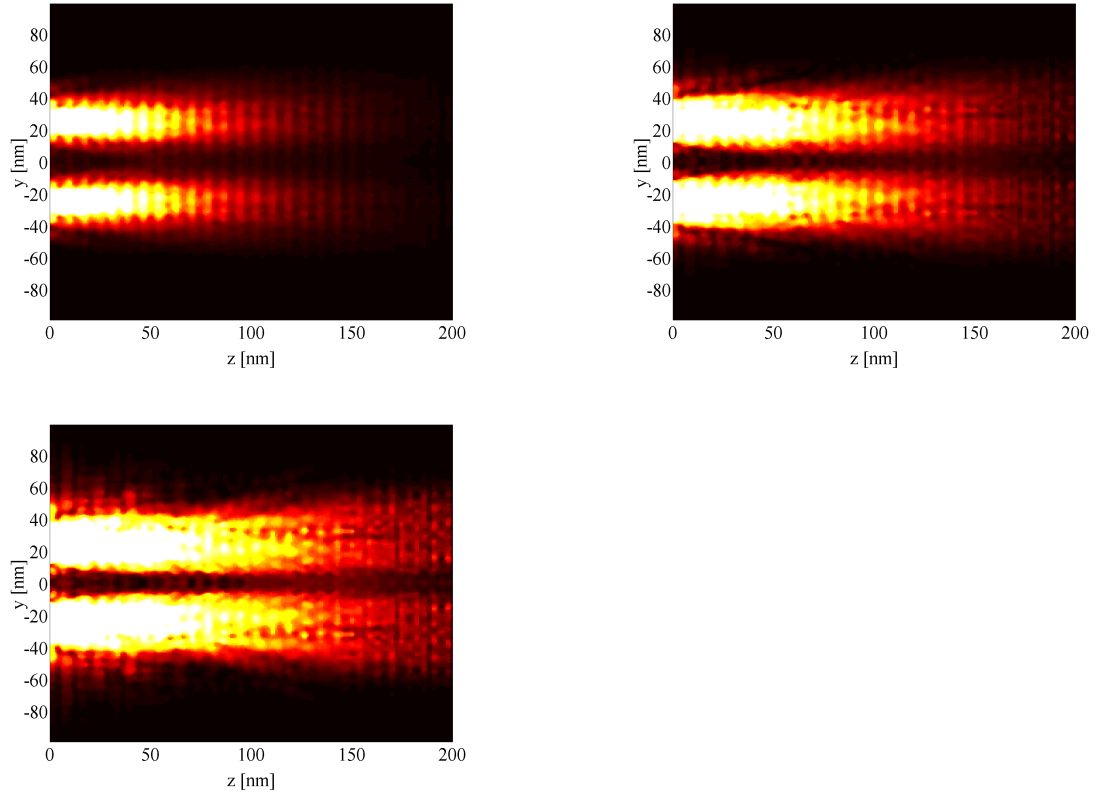


Figure 6.16: The normalized  $x$ -component of the electric field above the graphene surface ( $x = 2$  nm) for the peak value of  $\text{Im}(\sigma)/\text{Re}(\sigma)$  at 10 THz (top-left), 20 THz (top-right), and 30 THz (bottom).

be non-symmetric (the ratio of groove to ridge is 3) to produce the same conductivity function as the symmetrical triangular ridged ground plane.

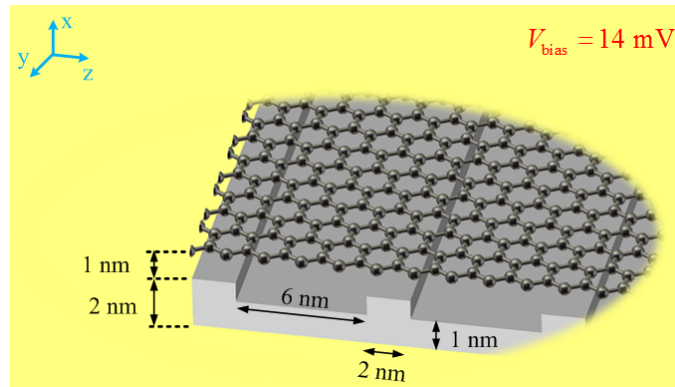


Figure 6.17: An alternative geometry with rectangular ridged ground plane to realize the soft-boundary example.

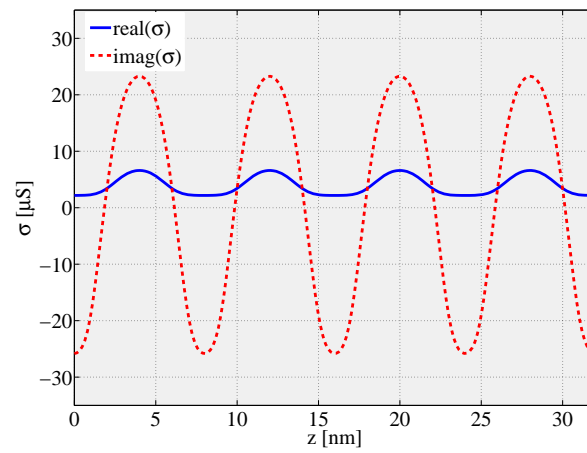


Figure 6.18: The conductivity distribution in the geometry of Fig. 6.17.

## Chapter 7

### Summary, future work and outlook

A new integro-differential equation was proposed for solving scattering problems involving wire media, allowing for the first treatment of three-dimensional wire medium objects. The integro-differential equation was shown to be efficient and accurate via comparisons with other results, known analytical results, and measurement for 1d, 2d, and 3d cases (both isotropic and anisotropic for 3d). In the 1d isotropic case the integro-differential equation led to an analytical solution. For 3d objects, the effect of wire period and diameter was investigated experimentally in a range of parameters that demonstrated the expected breakdown of homogenization for large wire period. In order to have a valid homogenized model for the uniaxial wire medium geometries studied, wire size should be larger than the Debye length, the wire diameter to period ratio should be less than 0.25, and the period should be such the plasma frequency is higher than the operating frequency.

Then, using wire medium as an ENZ material, sum and difference patterns were generated using a simple and novel structure and its radiation pattern, input impedance and directivity were investigated using full-wave simulations. The structure is useful for radar applications and tracking systems.

Focusing on ENZ materials, the “space-domain” nonlocal permittivity  $\underline{\epsilon}(\mathbf{r} - \mathbf{r}')$  has been obtained and a new characteristic screening length introduced for spatially dispersive materials, including artificial wire media. Unlike the Debye length, the new characteristic length relates polarization to the total electric field inside the material, and so it can be used to study the electric displacement distribution in relation to the ENZ condition. Using some typical values semiconductor and wire medium metamaterials, it was shown



that the new characteristic length is very small for semiconductors and therefore an ENZ condition can be easily obtained. However, for wire media the ENZ condition cannot be identically obtained except in some special cases, and often only the perpendicular displacement field can vanish.

In the last section, as a different example of homogenization, we have analyzed the possibility to produce in-plane canalization of SPPs on a 2D surface, with particular emphasis on its realization in a realistically modulated graphene monolayer, resulting in a planarized 2D hyperlens on graphene. We envision the use of this effect on a ridged ground plane for sub-wavelength imaging of THz sources and to arbitrarily tailor the front wave of an SPP by suitably designing the boundary of the canalization region.

## **Publications from this thesis in refereed journals**

- Ebrahim Forati, George W. Hanson, Alexander B. Yakovlev, and, Andrea Alu “A planar hyperlens based on a modulated graphene monolayer,” arXiv:1311.4791.
- Ebrahim Forati and George Hanson, “A transport model for homogenized uniaxial wire media: three dimensional scattering problems and homogenized model limits,” Physical Review B, Vol. 88, No. 12, Sep. 2013.
- Ebrahim Forati and George Hanson, “On the epsilon near zero condition for spatially dispersive materials,” New J. Phys. 15, 123027 (2013).
- Ebrahim Forati and George Hanson, “Scattering from isotropic connected wire medium metamaterials: three-, two- and one-dimensional cases,” IEEE Trans. On Antennas and Propagation, Vol. 61, No. 7, July 2013.
- George W. Hanson, Ebrahim Forati, and Mrio G. Silveirinha, “Modeling of spatially-dispersive wire media: transport representation, comparison with natural materials, and additional boundary conditions,” IEEE Trans. On Antennas and Propagation. Vol. 60, No. 9, pp.4219-4239, Sep. 2012.

## BIBLIOGRAPHY

- [1] G. Hanson, E. Forati, and M. Silveirinha, “Modeling of spatially-dispersive wire media: transport representation, comparison with natural materials, and additional boundary conditions,” *IEEE Trans. Antennas and Prop.*, vol. 60, pp. 4219–4239, 2012.
- [2] E. Forati and G. Hanson, “Scattering from isotropic connected wire medium metamaterials: three-, two- and one-dimensional cases,” *IEEE Trans. Antennas and Prop.*, vol. 61, pp. 3564–3574, 2013.
- [3] E. Forati and G. Hanson, “A transport model for homogenized uni-axial wire media: three dimensional scattering problems and homogenized model limits,” *Phys. Rev. B*, vol. 88, p. 125125, 2013.
- [4] E. Forati and G. Hanson, “A novel epsilon-near-zero total internal reflection antenna to form radar sum and difference patterns,” in *IEEE AP-S International Symposium on Antennas and Prop.*, 2013.
- [5] E. Forati and G. Hanson, “On the epsilon near zero condition for spatially dispersive materials,” *New J. Phys.*, vol. 15, p. 123027, 2013.
- [6] E. Forati, G. Hanson, A. Yakovlev, and A. Alu, “A planar hyperlens based on a modulated graphene monolayer,” *arXiv:1311.4791*, 2013.
- [7] T. Shen and T. Wong, “Response of elementary semiconducting structures to a terahertz electric field,” in *IEEE APS-URSI*, pp. 1613–1616, 2011.
- [8] M. Silveirinha, “Artificial plasma formed by connected metallic wires at infrared frequencies,” *Phys. Rev. B*, vol. 79, pp. 035118 (1–15), 2009.

- [9] A. Sihvola, *Electromagnetic mixing formulas and applications*. IEE press, 1999.
- [10] R. Ruppin, “Evaluation of extended maxwell-garnet theories,” *Optics communication*, pp. 273–279, 2000.
- [11] C. Bohren, “Applicability of effective-medium theories to problems of scattering and absorption by nonhomogeneous atmospheric particles,” *Journal of the Atmospheric Sciences*, vol. 43, pp. 468–475, 1986.
- [12] T. Jones, *Electromechanics of Particles*. Cambridge University Press, 2005.
- [13] T. A. N. Morgado, *Tailoring the near- and far-fields with wire media*. PhD thesis, University of Coimbra, 2011.
- [14] W. Lu and S. Sridhar, “Superlens imaging theory for anisotropic nanostructured metamaterials with broadband all-angle negative refraction,” *Phys. Rev. B*, vol. 77, p. 33101, 2008.
- [15] P. A. Belov and Y. Hao, “Subwavelength imaging at optical frequencies using a transmission device formed by a periodic layered metal-dielectric structure operating in the canalization regime,” *Phys. Rev. B*, vol. 73, p. 113110, 2006.
- [16] M. Silveirinha and N. Engheta, “Theory of supercoupling, squeezing wave energy, and field confinement in narrow channels and tight bends using epsilon-near-zero metamaterials,” *Phys. Rev. B*, vol. 76, p. 245109, 2007.
- [17] M. Silveirinha, P. Belov, and C. Simovski, “Subwavelength imaging at infrared frequencies using an array of metallic nanorods,” *Phys. Rev. B*, vol. 75, pp. 035108 (1–12), 2007.
- [18] C. S. R. Kaipa, A. B. Yakovlev, S. I. Maslovski, and M. G. Silveirinha, “Near-field imaging with a loaded wire medium,” *Phys. Rev. B*, vol. 86, pp. 155103 (1–10), 2012.

- [19] A. V. I.S. Nefedov, D. Chicherin, “Infrared cloaking based on wire media,” in *Proc. of SPIE*, vol. 6987, p. 698728, 2008.
- [20] S. C. G. Lovat, P. Burghignoli, “Shielding properties of a wire-medium screen,” *IEEE Trans. Electromag. Comp.*, vol. 50, pp. 80–88, 2008.
- [21] S. Hrabar, *Metamaterials and Plasmonics: Fundamentals, Modelling, Applications*, ch. Application of Wire Media in Antenna Technology, pp. 139–151. NATO Science for Peace and Security Series B: Physics and Biophysics, 2009.
- [22] P. Burghignoli, G. Lovat, F. Capolino, D. Jackson, and D. Wilton, “Directive leaky-wave radiation from a dipole source in a wire-medium slab,” *IEEE Trans. Antennas and Prop.*, vol. 56, pp. 1329–1338, 2008.
- [23] W. Rotman, “Plasma simulation by artificial dielectrics and parallel-plate media,” *IRE Transactions on Antennas and Propagation*, vol. 10, pp. 82–95, 1962.
- [24] J. Brown, *Progress in Dielectrics*, ch. Artificial dielectrics, p. 193225. Wiley, 1960.
- [25] J. M. Pitarke, F. Garcia-Vidal, and J. Pendry, “Effective medium response of a system of metallic cylinders,” *Phys. Rev. B*, vol. 57, pp. 15261–15288, 1998.
- [26] P. Belov, R. Marques, S. Maslovski, I. Nefedov, M. Silveirinha, C. Simovski, and S. Tretyakov, “Strong spatial dispersion in wire media in the very large wavelength limit,” *Phys. Rev. B*, vol. 67, p. 113103, 2003.
- [27] M. Silveirinha and C. Fernandes, “Homogenization of 3-d-connected and non-connected wire metamaterials,” *IEEE Trans. Microw. Theory Tech.*, vol. 53, p. 14181430, 2005.
- [28] M. G. Silveirinha, “Nonlocal homogenization model for a periodic array of -negative rods,” *Phys. Rev. E*, vol. 73, p. 046612, 2006.

- [29] C. Bohren and D. Huffman, *Absorption and Scattering of Light by Small Particles*. John Wiley and Sons, 1983.
- [30] G. Hanson, M. Silveirinha, P. Burghignoli, and A. Yakovlev, “Nonlocal susceptibility of the wire medium in the spatial domain considering material boundaries,” *New Journal of Physics*, 2013.
- [31] A. D. Yaghjian, “Electric dyadic green’s functions in the source region,” *Proc. IEEE*, vol. 68, pp. 248–263, 1980.
- [32] W. Chew, *Waves and Fields in Inhomogeneous Media*. IEEE Press, 1995.
- [33] G. Hanson, “Drift-diffusion: A model for teaching spatial dispersion concepts and the importance of screening in nanoscale structures,” *IEEE Antennas and Propagation Magazine*, vol. 52, pp. 198–207, 2012.
- [34] J. Volakis and K. Sertel, *Integral equation methods for electromagnetics*. Scitech, 2012.
- [35] C. David and F. J. G. de Abajo, “Spatial nonlocality in the optical response of metal nanoparticles,” *Physical Chemistry C*, pp. 19470–75, 2011.
- [36] R. Newton, “Optical theorem and beyond,” *Am. J. Physics*, vol. 44, pp. 639–642, 1976.
- [37] FDTD, *Lumerical Solutions*. Inc.
- [38] QWED, URL: [www.qwed.com.pl](http://www.qwed.com.pl). Warsaw, Poland.
- [39] SPI, *Flash-Dry Silver Paint*. Structure Probe Inc.
- [40] B. Wang and K.-M. Huang, “Shaping the radiation pattern with mu and epsilon-near-zero metamaterials,” *Progress In Electromagnetics Research*, vol. 106, pp. 107–119, 2010.

- [41] R. Zhou, H. Zhang, and H. Xin, "Metallic wire array as low-effective index of refraction medium for directive antenna application," *IEEE Trans. Antennas and Prop.*, vol. 58, no. 1, pp. 79–87, 2010.
- [42] M. I. Skolnik, *Introduction to Radar Systems*. Radar Handbook, 1962.
- [43] FEKO, "Software & Systems SA,(Pty) Ltd, 32 Techno Lane." Technopark. Stellenbosch 7600, EM.
- [44] A. Alu, N. Engheta, A. Erentok, and R. Ziolkowski, "Single-negative, double-negative and low-index metamaterials and their electromagnetic applications," *IEEE Antennas and Prop. Magazine*, vol. 49, pp. 23–36, 2007.
- [45] J. Brown, "Artificial dielectrics having refractive indices less than unity," *Proc. Inst. Elect. Eng.*, vol. 100IV, p. 51, Jan. 1953.
- [46] M. Silveirinha and N. Engheta, "Tunneling of electromagnetic energy through subwavelength channels and bends using  $\epsilon$ -near-zero materials," *Phys. Rev. Lett.*, vol. 97, p. 157403, 2006.
- [47] A. Alu, M. Silveirinha, A. Salandrino, and N. Engheta, "Epsilon-near-zero metamaterials and electromagnetic sources: Tailoring the radiation phase pattern," *Phys. Rev. B*, vol. 75, p. 155410, 2007.
- [48] N. Engheta, "Circuits with light at nanoscales: Optical nanocircuits inspired by metamaterials," *Science*, vol. 317, no. 5845, pp. 1698–1702, 2007.
- [49] F. Bilotti, S. Tricarico, and L. Vegni, "Electromagnetic cloaking devices for te and tm polarizations," *New J. of Phys.*, vol. 10, p. 115035, 2008.
- [50] F. Bilotti, S. Tricarico, and L. Vegni, "Plasmonic metamaterial cloaking at optical frequencies," *IEEE Trans. on Nanotechnology*, vol. 9, no. 1, pp. 55–61, 2010.

- [51] M. Navarro-Cia, M. Beruete, M. Sorolla, and N. Engheta, “Lens concept using epsilon near-zero (enz) metamaterials,” in *IEEE AP-S International Symposium on Antennas and Prop*, 2011.
- [52] M. Navarro-Ca, M. Beruete, I. Campillo, and M. Sorolla, “Enhanced lens by epsilon and mu near-zero metamaterial boosted by extraordinary optical transmission,” *Phys. Rev. B*, vol. 83, p. 115112, 2011.
- [53] E. Forati and G. W. Hanson, “Soft-boundary graphene nanoribbon formed by a graphene sheet above a perturbed ground plane: Conductivity profile and spp modal current distribution,” *J. Opt.*, vol. 15, pp. 114006–114006, 2013.
- [54] A. M. Portis, *Electromagnetic fields: sources and media*. New York: Wiley, 1978.
- [55] CST, *Microwave Studio*. <http://www.cst.com>.
- [56] K. S. Novoselov, A. K. Geim, S. V. Morozov, D. Jiang, Y. Zhang, S. V. Dubonos, I. V. Grigorieva, and A. A. Firsov, “Electric field effect in atomically thin carbon films,” *Science*, vol. 306, pp. 666–669, 2004.
- [57] A. H. Castro Neto, F. Guinea, N. M. R. Peres, K. S. Novoselov, and A. K. Geim, “The electronic properties of graphene,” *Rev. Mod. Phys.*, vol. 81, pp. 109–162, 2009.
- [58] X. Luo, T. Qiu, W. Lu, and Z. Ni, “Plasmons in graphene: Recent progress and applications,” *Materials Science and Engineering: R*, vol. 74, pp. 351–376, 2013.
- [59] Y. Zhang, Y. W. Tan, H. L. Stormer, and P. Kim, “Experimental observation of the quantum hall effect and berry’s phase in graphene,” *Nature*, vol. 438, pp. 201–204, 2005.
- [60] L. A. Falkovsky and A. A. Varlamov, “Space-time dispersion of graphene conductivity,” *Eur. Phys. J. B*, vol. 56, pp. 281–284, 2007.



- [61] L. A. Falkovsky and S. S. Pershoguba, “Optical far-infrared properties of a graphene monolayer and multilayer,” *Phys. Rev. B*, vol. 76, pp. 153410–153410, 2007.
- [62] S. A. Mikhailov and K. Ziegler, “New electromagnetic mode in graphene,” *Phys. Rev. Lett.*, vol. 99, pp. 016803–016803, 2007.
- [63] V. P. Gusynin, S. G. Sharapov, and J. P. Carbotte, “Unusual microwave response of dirac quasiparticles in graphene,” *Phys. Rev. Lett.*, vol. 96, pp. 256802–256802, 2006.
- [64] V. P. Gusynin and S. G. Sharapov, “Transport of dirac quasiparticles in graphene: Hall and optical conductivities,” *Phys. Rev. B*, vol. 73, pp. 245411–245411, 2006.
- [65] N. M. R. Peres, A. C. Neto, and F. Guinea, “Conductance quantization in mesoscopic graphene,” *Phys. Rev. B*, vol. 73, pp. 195411–195411, 2006.
- [66] G. W. Hanson, “Dyadic green’s functions for an anisotropic, non-local model of biased graphene,” *IEEE Trans. Antennas Propagat.*, vol. 56, pp. 747–757, 2008.
- [67] G. W. Hanson, “Dyadic greens functions and guided surface waves for a surface conductivity model of graphene,” *J. Appl. Phys.*, vol. 103, pp. 064302–064302, 2008.
- [68] N. M. R. Peres, F. Guinea, and A. C. Neto, “Electronic properties of disordered two-dimensional carbon,” *Phys. Rev. B*, vol. 73, pp. 125411–125411, 2006.
- [69] K. Ziegler, “Minimal conductivity of graphene: Nonuniversal values from the kubo formula,” *Phys. Rev. B*, vol. 75, pp. 233407–233407, 2007.
- [70] N. Ashcroft and N. Mermin, *Solid State Physics*. Saunders College, 1976.
- [71] V. P. Gusynin, S. G. Sharapov, and J. P. Carbotte, “Magneto-optical conductivity in graphene,” *J. Phys.: Condens. Matter*, vol. 19.2, pp. 026222–026222, 2007.

- [72] A. Vakil and N. Engheta, “Transformation optics using graphene,” *Science*, vol. 332.6035, pp. 1291–1294, 2011.
- [73] J. Christensen, A. Manjavacas, S. Thongrattanasiri, F. H. L. Koppens, and F. J. G. de Abajo, “Graphene plasmon waveguiding and hybridization in individual and paired nanoribbons,” *ACS Nano*, vol. 6, pp. 431–440, 2011.
- [74] G. W. Hanson, E. Forati, W. Linz, and A. B. Yakovlev, “Excitation of thz surface plasmons on graphene surfaces by an elementary dipole and quantum emitter: Strong electrodynamic effect of dielectric support,” *Phys. Rev. B*, vol. 86, pp. 235440 (1–9)–9, 2012.
- [75] A. Y. Nikitin, F. Guinea, F. J. Garcia-Vidal, and L. Martin-Moreno, “Edge and waveguide thz surface plasmon modes in graphene micro-ribbons,” *arXiv*, vol. 1107.5787, pp. –, 2011.
- [76] D. L. Sounas and C. Caloz, “Edge surface modes in magnetically biased chemically doped graphene strips,” *Appl. Phys. Lett.*, vol. 98, pp. 021911–021911, 2011.
- [77] W. Wang, P. Apell, and J. Kinaret, “Edge plasmons in graphene nanostructures,” *Phys. Rev. B*, vol. 84, pp. 085423–085423, 2011.
- [78] E. Forati and G. W. Hanson, “Surface plasmon polaritons on soft-boundary graphene nanoribbons and their application in switching/demultiplexing,” *Appl. Phys. Lett.*, vol. 103, pp. 133104–133104, 2013.
- [79] H. Raether, *Surface Plasmons*. Berlin: Springer, 1988.
- [80] A. Y. Nikitin, F. Guinea, F. J. Garcia-Vidal, and L. Martin-Moreno, “Fields radiated by a nanoemitter in a graphene sheet,” *Phy. Rev. B*, vol. 84, pp. 195446–195446, 2011.

- [81] C. Berger, Z. Song, X. Li, X. Wu, N. Brown, C. Naud, D. Mayou, T. Li, J. Hass, and A. N. Marchenkov, “Electronic confinement and coherence in patterned epitaxial graphene,” *Science*, vol. 312, pp. 1191–1196, 2006.
- [82] T. Mueller, F. Xia, M. Freitag, J. Tsang, and P. Avouris, “Role of contacts in graphene transistors: A scanning photocurrent study,” *Phys. Rev. B*, vol. 79, pp. 245430–245430, 2009.
- [83] R. R. Nair, P. Blake, A. N. Grigorenko, K. S. Novoselov, T. J. Booth, T. Stauber, N. M. R. Peres, and A. K. Geim, “Fine structure constant defines visual transparency of graphene,” *Science*, vol. 320, pp. 1308–1308, 2008.
- [84] F. Bonaccorso, Z. Sun, T. Hasan, and A. C. Ferrari, “Graphene photonics and optoelectronics,” *Nat. Photon.*, vol. 4, pp. 611–622, 2010.
- [85] F. N. Xia, T. Mueller, Y. M. Lin, A. Valdes-Garcia, and P. Avouris, “Ultrafast graphene photodetector,” *Nat. Nanotechnol.*, vol. 4, pp. 839–843, 2009.
- [86] K. F. Mak, M. Y. Sfeir, Y. Wu, C. H. Lui, J. A. Misewich, and T. F. Heinz, “Measurement of the optical conductivity of graphene,” *Phys. Rev. Lett.*, vol. 101, pp. 196405–196405, 2008.
- [87] T. Otsuji, S. B. Tombet, A. Satou, H. Fukidome, M. Suemitsu, E. Sano, V. Popov, M. Ryzhii, and V. Ryzhii, “Graphene-based devices in terahertz science and technology,” *J. Phys. D: Appl. Phys.*, vol. 45, pp. 303001–303001, 2012.
- [88] C. Docherty and M. Johnston, “Terahertz properties of graphene,” *J. Infrared Millim. Terahertz Waves*, vol. 33, pp. 797–815, 2012.
- [89] J. S. Gomez-Diaz, M. Esquius-Morote, and J. Perruisseau-Carrier, “Plane wave excitation-detection of non-resonant plasmons along finite-width graphene strips,” *Optics Express*, vol. 21, pp. 24856–24872, 2013.

- [90] J. S. Gomez-Diaz and J. Perruisseau-Carrier, “Graphene-based plasmonic switches at near infrared frequencies,” *Optics Express*, vol. 21, pp. 15490–15504, 2013.
- [91] Y. Jiang, W. Lu, H. Xu, Z. Dong, and T. Cui, “A planar electromagnetic “black hole” based on graphene,” *Phys. Lett. A*, vol. 376, pp. 1468–1471, 2012.
- [92] P. Y. Chen and A. Al, “Atomically thin surface cloak using graphene monolayers,” *ACS Nano*, vol. 5, pp. 5855–5863, 2011.
- [93] Y. Liu, X. Dong, and P. Chen, “Biological and chemical sensors based on graphene materials,” *Chem. Soc. Rev.*, vol. 41, pp. 2283–2307, 2012.
- [94] S. Szunerits, N. Maalouli, E. Wijaya, J. Vilcot, and R. Boukherroub, “Recent advances in the development of graphene-based surface plasmon resonance (spr) interfaces,” *Anal. Bioanal. Chem.*, vol. 405, pp. 1435–1443, 2013.
- [95] J. B. Pendry, “Negative refraction makes a perfect lens,” *Phys. Rev. Lett.*, vol. 85, pp. 3966–3966, 2000.
- [96] V. Veselago, “The electrodynamics of substances with simultaneously negative values of *and*,” *Sov. Phys. Usp.*, vol. 10, pp. 509–514, 1968.
- [97] P. Ikonen, P. A. Belov, C. R. Simovski, and S. I. Maslovski, “Experimental demonstration of subwavelength field channeling at microwave frequencies using a capacitively loaded wire medium,” *Phys. Rev. B*, vol. 73, pp. 073102–073102, 2006.
- [98] E. E. Narimanov and V. M. Shalaev, “Optics: Beyond diffraction,” *Nature*, vol. 447.7142, pp. 266–267, 2007.
- [99] A. Salandrino and N. Engheta, “Far-field subdiffraction optical microscopy using metamaterial crystals: Theory and simulations,” *Phys. Rev. B*, vol. 74, pp. 075103–075103, 2006.

- [100] P. A. Belov, C. R. Simovski, and P. Ikonen, “Canalization of subwavelength images by electromagnetic crystals,” *Phys. Rev. B*, vol. 71, p. 193105, 2005.
- [101] P. Belov and M. Silveirinha, “Resolution of subwavelength transmission devices formed by a wire medium,” *Phys. Rev. E*, vol. 73, p. 056607, 2006.
- [102] G. W. Hanson, A. B. Yakovlev, and A. Mafi, “Excitation of discrete and continuous spectrum for a surface conductivity model of graphene,” *J. Appl. Phys.*, vol. 110, pp. 114305–114305, 2011.
- [103] P. A. Belov, Y. Zhao, S. Tse, P. Ikonen, M. G. Silveirinha, C. R. Simovski, and S. Tretyakov, “Transmission of images with subwavelength resolution to distances of several wavelengths in the microwave range,” *Phy. Rev. B*, vol. 77, p. 193108, 2008.
- [104] S. A. Ramakrishna, J. B. Pendry, M. C. K. Wiltshire, and W. J. Stewart, “Imaging the near field,” *J. Mod. Opt.*, vol. 50, pp. 1419–1430, 2003.
- [105] Z. Q. Li, E. A. Henriksen, Z. Jiang, Z. Hao, M. C. Martin, P. Kim, H. L. Stormer, and D. N. Basov, “Dirac charge dynamics in graphene by infrared spectroscopy,” *Nat. Phys.*, vol. 4, pp. 532–535, 2008.
- [106] C. Lee, J. Y. Kim, S. Bae, K. S. Kim, B. H. Hong, and E. J. Choi, “Optical response of large scale single layer graphene,” *Appl. Phys. Lett.*, vol. 98, pp. 071905–071905, 2011.
- [107] J. Y. Kim, C. Lee, S. Bae, K. S. Kim, B. H. Hong, and E. J. Choi, “Far-infrared study of substrate-effect on large scale graphene,” *Appl. Phys. Lett.*, vol. 98, pp. 201907–201907, 2011.
- [108] A. Alu and N. Engheta, “Optical nanotransmission lines: Synthesis of planar left-handed metamaterials in the infrared and visible regimes,” *JOSA B*, vol. 23, pp. 571–583, 2006.

## CURRICULUM VITAE

### Ebrahim Forati

University of Wisconsin-Milwaukee  
Department of Electrical Engineering  
3200 North Cramer Street  
Milwaukee, WI 53211 USA

Phone: (414) 306-3767  
email: forati@ieee.org

#### Education:

- **Doctor of Philosophy in Engineering,**  
University of Wisconsin-Milwaukee, May 2014.

Thesis title: *A novel transport based model for wire media and its application to scattering problems.*

Advisor: George W. Hanson.

- **Master of Science in Electrical Engineering,**  
Iran University of Science and Technology, July 2009.
- **Bachelor of Science in Electrical Engineering,**  
Iran University of Science and Technology, September 2006.

#### Research Interests:

- Electromagnetics, Metamaterials, Graphene, Antenna.

#### Publications in refereed journals:

- Ebrahim Forati, George Hanson, Alexander Yakovlev, and Andrea Alu, **“A planar hyperlens based on a modulated graphene monolayer”** *submitted, arXiv:1311.4791*
- Ebrahim Forati and George Hanson, **“Surface plasmon polaritons on soft-boundary graphene nanoribbons and their applications as voltage controlled plasmonic switches and frequency demultiplexers”** *Applied Physics Letters*, Vol. 103, pp. 133104, 2013. DOI: 10.1063/1.4822044
- Ebrahim Forati and George Hanson, **“Soft-boundary graphene nanoribbon formed by a graphene sheet above a perturbed ground plane: conductivity profile and SPP modal current distribution”** *Journal of optics*, Vol. 15, pp. 114006, 2013. DOI: 10.1088/2040-8978/15/11/114006

- Ebrahim Forati and George Hanson, “**On the epsilon near zero condition in spatially dispersive materials**” *New Journal of Physics* , Vol. 15, pp. 123027, 2013
- Ebrahim Forati and George Hanson, “**A transport model for homogenized uniaxial wire media: three dimensional scattering problems and homogenized model limits**” *Physical Review B*, Vol. 88, No. 12, Sep. 2013, DOI: 10.1103/PhysRevB.88.125125
- Ebrahim Forati and George Hanson, “**Scattering from isotropic connected wire medium metamaterials: three-, two- and one-dimensional cases,**” *IEEE Trans. On Antennas and Propagation*, DOI:10.1109/TAP.2013.2254455
- George W. Hanson, Ebrahim Forati, Whitney Linz, and Alexander B. Yakovlev, “**Excitation of THz surface plasmons on graphene surfaces by an elementary dipole and quantum emitter: Strong electrodynamic effect of dielectric support,**” *Physical Review B*, Vol. 86, No. 23, Dec. 2012, DOI: 10.1103/PhysRevB.86.235440
- D. Li, Y. S. Jung, H. K. Kim, J. Chen, D. A. Geller, M. V. Shuba, S. A. Maksimenko, L. Li, S. Patch, E. Forati, and G. W. Hanson, “**The effect of sample holder geometry on electromagnetic heating on nanoparticle and NaCl solutions at 13.56 MHz,**” *IEEE Trans. On Biomedical Engineering*, Vol. 59, No. 12, Dec. 2012, DOI:10.1109/TBME.2012.2219049
- George W. Hanson, Ebrahim Forati, and Mrio G. Silveirinha, “**Modeling of spatially-dispersive wire media: transport representation, comparison with natural materials, and additional boundary conditions,**” *IEEE Trans. On Antennas and Propagation*. Vol. 60, No. 9, pp.4219-4239, Sep. 2012, DOI:10.1109/TAP.2012.2207078
- E. Forati, A. D. Mueller, P. Gandomkar, G. Hanson, “**A New Formulation of Pocklington's Equation for Thin Wires Using the Exact Kernel,**” *IEEE Trans. On Antennas and Propagation*. Vol. 59, No. 11, pp.4355-4360, Nov. 2011, DOI:10.1109/TAP.2011.2164211
- H. Oraizi and E. Forati, “**Novel Circuit Topologies for Active Distributed Frequency Multiplexers and De-multiplexers,**” *International Journal of RF and Microwave Computer-Aided Engineering*, vol. 21, Issue 1, pp. 67-76, Jan 2011, DOI: 10.1002/mmce.20488
- H. Oraizi and E. Forati, “**Novel Wideband Active Microstrip Antennas Using Active Distributed Frequency Multiplexers or De-multiplexers,**” *International*

*Journal of RF and Microwave Computer-Aided Engineering*, vol. 20, Issue 4, pp. 408-415, July 2010, DOI: 10.1002/mmce.20445

### Conferences and meetings presentations:

- (Submitted) Ebrahim Forati, George W. Hanson, and Stephen Hughes, **“Graphene as a tunable reservoir for shaping the incoherent spectrum of a quantum dot via plasmonic effects,”** *Conference on Lasers and Electro-Optics (CLEO), San Jose, CA, June 2014*
- (Oral, E. Forati) E. Forati, G. W. Hanson, Alexander Yakovlev, Andrea Alu, **“Canalization of surface plasmon polaritons on a graphene sheet with a perturbed ground plane,”** *USNC/URSI National Radio Science Meeting, Boulder, CO, January 2014*
- (Oral, E. Forati) Ebrahim Forati and George Hanson, **“A novel epsilon-near-zero total internal reflection antenna to form radar sum and difference patterns,”** *IEEE AP-S International Symposium and USNC/URSI National Radio Science Meeting, Orlando, FL, July 2013*
- (Oral, E. Forati) Ebrahim Forati and George Hanson, **“Three dimensional scattering problems involving uniaxial and isotropic wire medium objects:spherical and cubical examples,”** *IEEE AP-S International Symposium and USNC/URSI National Radio Science Meeting, Orlando, FL, July 2013*
- (Poster) G. W. Hanson, E. Forati A. B. Yakovlev, **“Excitation amplitude of THz surface plasmons on graphene surfaces by an elementary dipole and quantum emitter,”** *Graphene Nanophotonics 2013, Benasque (Spain), March 4-8, 2013*
- (Keynote talk., A. B. Yakovlev) A. B. Yakovlev, S. I Maslovski, M. G. Silveirinha, C. S. R. Kaipa, G. W. Hanson, P. A. Belov, O. Luukkonen, I. S. Nefedov, C. R. Simovski, S. A. Tretyakov, Y. R. Padooru and E. Forati, **“Homogenization of Wire Media for the Efficient Analysis of Practical Metamaterial Structures at Microwave and Terahertz Frequencies,”** *META13, the 4th International Conference on Metamaterials, Photonic Crystals and Plasmonics, Sharjah-UAE, March 2013*
- (Oral, E. Forati) E. Forati, G. W. Hanson, **“The interaction of electromagnetic waves and three-dimensional non-isotropic (uniaxial) wire medium metamaterials based on a transport model,”** *USNC/URSI National Radio Science Meeting, Boulder, CO, January 2013*



- (Poster) E. Forati, G. W. Hanson, **“Scattering Problems Involving Three Dimensional Non-Local Wire Metamaterials Based on a Transport Model,”** *IEEE AP-S International Symposium and USNC/URSI National Radio Science Meeting, Chicago, IL, July 2012*
- (Oral, E. Forati) E. Forati, G. W. Hanson, T. Shen and T. Wong, **“Drift-diffusion and transport models for the analysis of non-local plasmas and metamaterials,”** *USNC/URSI National Radio Science Meeting, Boulder, CO, January 2012*
- (Oral, H. Oraizi) H. Oraizi, and E. Forati, **“Adjustment of resonant frequency of rectangular patch antenna by placing metallic walls or vias adjacent to its edge,”** *10th Mediterranean Microwave Symposium (MMS’2010), Cyprus, August, 2010, pp. 431-435*
- (Oral, E. Forati) H. Oraizi, and E. Forati, **“A Novel design of Multiplexers and Demultiplexers,”** *17th Iranian Conference on Electrical Engineering (ICEE), Tehran, Iran, May.2009*
- (Oral, H. Oraizi) H. Oraizi, E. Forati and M. S. Esfahlan, **“A Novel Topology For The Implementation of Active Distributed Multiplexers,”** *19th European Conference of Circuit Theory and Design (ECCTD), Antalya, Turkey, 2009, pp. 383-386*
- (Oral, M. S. Esfahlan) H. Oraizi, M. S. Esfahlan, and E. Forati, **“Design of Stepped-Impedance Low Pass Filters with Impedance Matching by Particle Swarm Optimization and Conjugate Gradient Method,”** *19th European Conference of Circuit Theory and Design (ECCTD), Antalya, Turkey, 2009, pp. 639-642*

#### Awards:

- USNC-URSI travel fellowship award (two times in years 2012 and 2013) to support the participation to the National Radio Science meeting in Boulder, CO, USA
- UWM Chancellor’s award (Five times between 2010 and 2014)

#### Membership:

- Student member of IEEE (2009-present)
- IEEE Antennas and propagation society (2012-present)

- Student member of American Physical Society (2013-present)

**Technical software skills:**

- Skilled in:  
MATLAB/HFSS/ COMSOL /ADS/FEKO/MathCAD/Lumerical/CST
- Familiar with:  
SONNET/Ansoft Designer/Protel /Microwave office/Orcad/Pascal

**Teaching experience at UWM:**

- Fall 2013: Instructor of EE150, Electronic Technology in the World Around us, Teaching Assistan of EE305, Electrical Circuits II
- Summer 2013: Instructor of EE305, Electrical Circuits II
- Spring 2013: Teaching Assistant of EE101, Fundamentals of Electrical Engineering
- Fall 2012: Instructor of EE150
- Summer 2012: Instructor of EE335, Electronics II
- Spring 2012: Instructor of EE150
- Fall 2011: Teaching Assistant of EE299 (Later changed to EE101) Fundamentals of Electrical Engineering

**Technical Reviewer:**

- American Math Society
- IEEE Transactions on Antennas and propagation
- American Physical Society
- Journal of Optics
- iCBEB conference